Karlsruher Institut für Technologie

# The Influence of Strong Stellar Particle Events and Galactic Cosmic Rays on Exoplanetary Atmospheres

Zur Erlangung des akademischen Grades eines

Doktors der Naturwissenschaften (Dr. rer. nat.)

von der KIT-Fakultät für Physik des
Karlsruher Instituts für Technologie (KIT)

genehmigte

Dissertation

von

Andreas Bartenschlager, M. Sc.

aus Mindelheim

Tag der mündlichen Prüfung: 07. November 2025
Referent: Prof. Dr. Peter Braesicke
Korreferent: Prof. Dr. Thomas Leisner
Betreuerin: Dr. Miriam Sinnhuber

# Abstract

Humanity has always been fascinated by the universe and has continuously expanded its knowledge about it. Since the first discovery of a planet outside the solar system, improved technology now also allows us to investigate potential atmospheres around these planets, which are influenced by their home star.

It is known from Earth that highly energetic particles can change the composition of Earth's atmosphere, in particular influencing so-called biosignatures such as ozone ($O_3$) or nitrous oxide ($N_2O$). These are trace gases that could indicate biogenic activity and are relevant for observations of exoplanets. Red dwarf stars are the most common type of star in the universe and often have higher stellar activity than Sun-like stars. Studying the effects of these energetic particles on the atmospheres of planets orbiting red dwarfs is crucial for improving the interpretation of current and future measurements.

In this context, the thesis addresses the influence of strong stellar energetic particle events (SEP) on exoplanetary atmospheres. Various simulations were carried out using the ion chemistry model ExoTIC (**Exo**planetary **T**errestrial **I**on **C**hemistry model). After validating newly implemented reactions using today's Earth atmosphere during the Halloween energetic particle event in October 2003, the model simulations were extended to two exoplanets with diverse atmospheres. These two planets orbit an active on the one hand, and an inactive red dwarf star on the other hand. To model the particle environment for red dwarf stars, the Carrington event of 1859 was scaled to the position of the exoplanets around their host star. For Earth, it was one of the strongest ever recorded solar energetic particle event.

The comparison between simulations and observations on Earth during the Halloween storm of 2003 showed good agreement, suggesting that the model configuration can be used for further simulations. The results for the different exoplanetary atmospheres varied significantly. For $N_2$–dominated atmospheres, changes in the $N_2O$, $H_2O$, and $O_3$ concentrations were observed during the particle event, while in $H_2$–dominated atmospheres, water vapor was primarily affected. The changes in atmospheric composition are therefore also reflected in the simulated transmission spectra and can make it more difficult to

interpret the measured data. Particularly in $N_2$-dominated atmospheres without biogenic fluxes, the abiotic production of $N_2O$ shows more pronounced signals in the simulated transmission spectrum and suggests that $N_2O$ is a marker for stellar activity rather than a robust biosignature.

The results of this work contribute to a better interpretation of current and future measurements and show that the influence of stellar energetic particles have to be taken into account. In particular, since exoplanetary atmospheres can vary greatly, the effects on composition are very different.

# Zusammenfassung

Seit jeher sind Menschen fasziniert vom Universum und haben den Drang das Wissen darüber kontinuierlich zu erweitern. Seit der ersten Entdeckung eines Planeten außerhalb des Sonnensystems, erlaubt es die verbesserte Technologie auch potentielle Atmosphären um diese Planeten zu untersuchen. Diese Atmosphären werden durch den Heimatstern des Planeten beeinflusst.

Von der Erde ist bekannt, dass energiereiche Teilchen die Zusammensetzung der Erdatmosphäre verändern können, insbesondere auch Einfluss auf sogenannte Biosignaturen wie Ozon ($O_3$) oder Lachgas ($N_2O$) nehmen. Dies sind Spurengase, die auf eine biogene Aktivität hinweisen könnten und für Beobachtungen von Exoplaneten von größerer Relevanz sind. Rote Zwergsterne sind im Universum der am häufigsten vorkommende Sterntyp und besitzen oft eine größere stellare Aktivität im Vergleich zur Sonne. Die Untersuchung der Auswirkungen dieser energiereichen Teilchen auf die Atmosphäre von Planeten um rote Zwerge ist entscheidend, um die Interpretation von gegenwärtigen und zukünftigen Messungen zu verbessern.

Die vorliegende Arbeit befasst sich in diesem Kontext mit dem Einfluss von starken stellaren Teilchenereignissen (SEP) auf Exoplanetare Atmosphären. Hierzu wurden verschiedene Simulationen mit dem Ionenchemiemodell ExoTIC (**Exo**planetary **T**errestrial **I**on **C**hemistry model) durchgeführt. Nach einer Validierung von neu hinzugefügten Reaktionen am Beispiel der heutigen Erdatmosphäre während des Halloween Ereignisses im Oktober 2003, wurden die Modellsimulationen auf zwei Exoplaneten mit unterschiedlichen Atmosphären ausgedehnt. Diese beiden Planeten umkreisen dabei einerseits einen aktiven und andererseits einen inaktiven roten Zwergstern. Für die Modellierung des dortigen Teilchenflusses, wurde das auf der Erde beobachtete Carringtonereignis von 1859 auf die Position der Exoplaneten um deren Stern skaliert.

Der Vergleich zwischen den Simulationen und Beobachtungen auf der Erde während des Halloween Ereignisses von 2003 ergab eine gute Übereinstimmung. Demnach konnte das Modell Setup für die weiteren Simulationen verwendet werden. Die Ergebnisse für die verschiedenen exoplanetaren Atmosphären variierten deutlich. Für $N_2$-dominierte

Atmosphären zeigten sich während des Teilchenereignisses Veränderungen in den $N_2O$, $H_2O$ sowie $O_3$ Konzentrationen, wohingegen bei $H_2$-dominierten Atmosphären vor allem Wasserdampf beeinflusst wird. Die Veränderungen in der atmosphärischen Zusammensetzung zeigen sich folglich auch in den simulierten Transmissionsspektren und können die Interpretation der Messdaten erschweren. Insbesondere in $N_2$-dominierten Atmosphären ohne biogene Flüsse ist die abiotische Produktion von $N_2O$ mit deutlicheren Signalen im Transmissionsspektrum zu sehen und deutet darauf hin, dass $N_2O$ eher ein Marker für stellare Aktivität ist, als eine robuste Biosignatur.

Die Ergebnisse dieser Arbeit tragen dazu bei, aktuelle und zukünftige Messungen besser interpretieren zu können und zeigt auf, dass dabei der Einfluss von energiereichen Teilchen berücksichtigt werden muss. Insbesonders, da exoplanetare Atmosphären sehr unterschiedlich sein können, sind die Auswirkungen auf die Zusammensetzung sehr verschieden.

# Foreword

*"To me, it underscores our responsibility to deal more kindly with one another, and to preserve and cherish the pale blue dot, the only home we've ever known."*

— Carl Sagan, *Pale Blue Dot*, 1997

Part of the results presented in chapter 5 form a core contribution to a peer-reviewed article in the Astrophysical Journal:
*Herbst, K., Bartenschlager, A., Grenfell, J. L., Iro, N., Sinnhuber, M., Taysum, B., Wunderlich, F., Engelbrecht, N. E., Light, J., Moloto, K. D., Harre, J.-V., Rauer, H., & Schreier, F. (2024). Impact of Cosmic Rays on Atmospheric Ion Chemistry and Spectral Transmission Features of TRAPPIST-1e.* The Astrophysical Journal, 961*(2), 164. https://doi.org/10.3847/1538-4357/ad0895*

As a non-native English speaker, I used the language-support tool DeepL to improve grammar and style. All scientific content, analyses, and conclusions are my own work.

# Contents

# 1 Introduction

## 1.1 Motivation

Since the first detection of an extrasolar planet (exoplanet) around a solar-type star by Mayor and Queloz (1995), more than 6,000[1] planets have been detected so far, and the number is increasing quite fast. This suggests that extrasolar systems are very common in the universe and the shape of their planets can be very different.

For observations, it is easier to detect larger planets around sun-like stars, but evolving technology over past decades has also made it possible to discover Earth-sized planets. In 2011, Fressin et al. (2012) announces the detection of two Earth-sized planets around the star Kepler-20. The system was observed by NASA's Kepler space observatory and the planets were subsequently named Kepler-20e and f. This type of planet in particular is of great interest, as the rocky structure could be ideal for the search for life. As we know so far, it is crucial for surface life that a planet has an atmosphere, shielding the harmful stellar radiation. For this reason, observations in recent years have increasingly focused on discovering and studying the atmospheres of extrasolar planets, finding a great diversity of atmospheric compositions (Madhusudhan et al., 2016). However, in contrast to the discovery of planets, it requires a much higher measurement accuracy of the instruments, since the contribution of an atmosphere is much smaller compared to the star-to-planet ratio.

Ongoing missions like the Hubble Space Telescope (HST) and the James Webb Space Telescope (JWST) are able to characterize exoplanetary atmospheres in different wavelength ranges from visible to infrared using the transit method. Within this range, several trace gases absorb very well, for example $H_2O$ (2.7 $\mu$m), $CO_2$ (4.3 $\mu$m) or $O_3$ (9.6 $\mu$m) have absorption bands in the infrared (Goody & Yung, 1995). Although the technical limits are being pushed further and further and are reaching their current peak with JWST, it is still not possible to characterize atmospheres of Earth-like planets around Sun-like stars

[1] https://exoplanetarchive.ipac.caltech.edu/, last visited December 9, 2025

with JWST, as the atmospheric signal-to-noise ratio is still too low. Therefore, current observations focus on M dwarf stars, which are smaller and have a higher star-planet ratio (Seager et al., 2025). Fortunately, M-dwarf stars are the most abundant type of star in the universe, which significantly increases the number of observational targets (Henry & Jao, 2024).

As M-dwarf stars tend to be more active compared to the sun, the stellar environment is influenced by potential more frequent and more stellar energetic particle events (SEPs), caused by coronal mass ejections (CMEs) or stellar flares, and galactic cosmic rays (GCRs) as remnants of supernovae (Herbst et al., 2019a). Figure 1.1 illustrates the interaction between stellar activity and planetary atmospheres, using Earth as an example. Once the SEPs hit the atmosphere, they enable a cascade of different reactions that change the Earth's atmospheric composition (right part of Fig. 1.1).

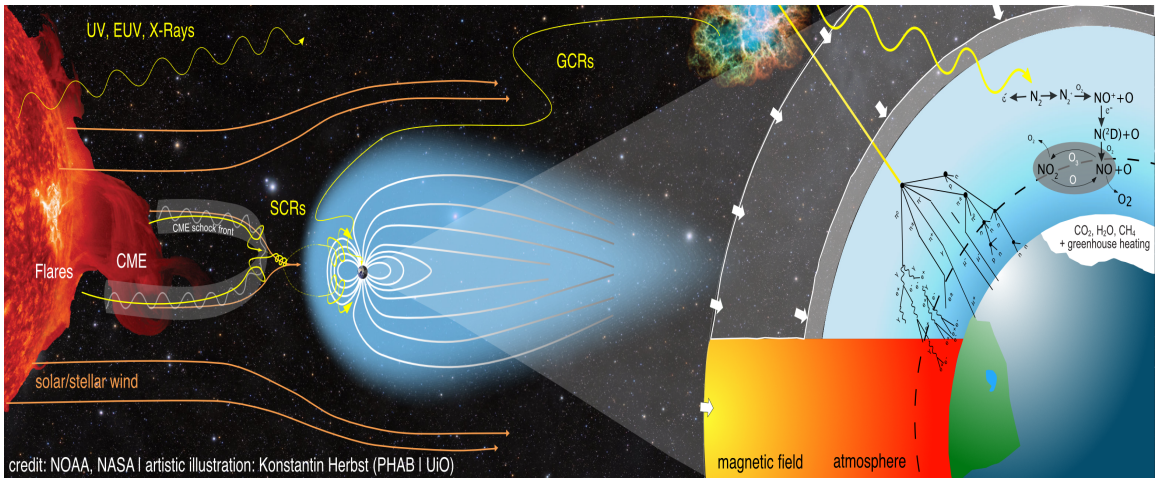


**Figure 1.1: Artists' illustration of the interaction between stellar activity and planetary atmospheres.** The figure illustrates the interactions between different fields of research. Understanding the effects of stellar energetic particles require a combination of stellar physics and the mechanisms behind stellar activity (left part), as well as the interaction of such energetic particles with planetary atmospheres. For example in Earth's atmosphere, the mechanism of Ozone depletion by $NO_x$ chemistry is shown in the right part of the figure (Credit: NOAA/NASA, public domain, artistic illustration created by Konstantin Herbst (PHAB | UiO), used with permission).

On Earth, these SEPs are known to influence the chemical constituents of the upper atmosphere mainly due to $HO_x$ (H, OH, $HO_2$) and $NO_x$ (N, NO, $NO_2$) species (Sinnhuber et al., 2012). This will be further explained in chapter 2. Not only the Earth, but also the atmosphere of Mars is exposed to the impact of high-energy particles. A recent numerical study from Nakamura et al. (2023) also suggests Ozone ($O_3$) depletion by $HO_x$

and $NO_x$ similar to Earth. However, this is based on a slightly different mechanism, as the atmosphere is $CO_2$ dominated.

Regarding the variety of atmospheres and the more active M-dwarf stars, it is interesting to apply this knowledge to extrasolar planets with the aim of better interpreting future observations.

## 1.2 Research Questions

A key concept in exoplanetary research is the so-called atmospheric biosignatures. They are trace gases, which can be attributed to life or be produced by organic processes. These include molecular oxygen ($O_2$), methane ($CH_4$), nitrous oxide ($N_2O$) and ozone ($O_3$) as a photochemical by-product of $O_2$ (Grenfell, 2018). As mentioned in the previous section, SEPs change the composition of the atmosphere and also cover the species noted above. Hence, there could be potential to form biosignatures by abiotic mechanisms and create false positive or false negative signals in the observations, which could be misleading in the interpretation whether there is life beyond Earth or not. Together with the current knowledge about energetic particles and the properties of M-dwarf stars, the objective of this thesis is to address the following scientific questions.

***Q1.*** ***How do stellar energetic particles and galactic cosmic rays influence the composition of different atmospheres of planets around M-dwarf stars?***

***Q2.*** ***What impact do these changes in atmospheric composition have on the observed transmission spectra and their interpretation?***

***Q3.*** ***Does this affect the observability and interpretation of the so-called biosignatures in current and future observations?***

To investigate these questions, model experiments are performed with the help of the 1D ion chemistry model ExoTIC (Sinnhuber et al., 2012; Winkler, 2008). After describing the details of the model in chapter 3, the thesis starts in chapter 2 with an introduction to the theoretical background on the different types of stars and the principles of energetic particles impacting planetary atmospheres. As part of this thesis, several new reactions are added to the source code of ExoTIC. The results for validation against the atmosphere of modern Earth are shown in chapter 4. Based on that, numerical simulations for two

exoplanetary systems with different properties are performed to study the influence of energetic particles. The two systems studied, around the stars TRAPPIST-1 and LHS1140, are located in the neighborhood of the solar system and host at least one rocky planet in the so-called habitable zone. Both stars are red dwarf stars with different stellar activity and are therefore very interesting in terms of energetic particle precipitation. The thesis concludes with a summary and looks to future developments and observations in the final chapter 6.

# 2 Theoretical Background

The universe is quite complex and very diverse, and stars or planetary atmospheres are no exception. With the newest instruments in space, these can be examined in more detail. This chapter provides a theoretical overview of different types of stars and planetary atmospheres (section 2.1). The sections 2.2 and 2.3 describe the topics which are the focus of this thesis. They give an introduction to the phenomenon of particle precipitation, which includes stellar or solar particle events (SPE) and galactic cosmic rays (GCRs) and describe the influence of such particles on the atmospheric chemistry. Finally, section 2.4 introduces the different methods to observe (exo)planetary atmospheres.

## 2.1 From Stars to (Exo)planetary Atmospheres

The sun provides light and energy and has always fascinated mankind. Without the sun, life on Earth would not be possible. With the progress of science, it was recognized that it is just one star among many, which also raised the question of its origin. Star formation begins in interstellar clouds filled with gas – mostly $H_2$ – and dust. If the gravitational potential energy is higher than the kinetic energy of the particles, the cloud gets gravitationally unstable and will contract (Hanslmeier, 2023). This contraction towards the center of the cloud leads to collisions between the molecules, which results in a temperature increase. As the temperature rises, the $H_2$ molecules are first dissociated and then ionized (Hanslmeier, 2023), creating a plasma of free charged particles.

The released energy of the continuing gravitational collapse will increase the motion of the charged particles, which leads to an internal pressure gradient, slowing down the collapse. A temperature of ~30,000 K is necessary to form a protostar (Beech, 2019). The formed core accretes material, which leads to a surrounding disk, due to the conservation of angular momentum. By accreting more and more material onto the stellar surface, the protostar becomes bigger and heats up. When the temperature in its core is high enough, nuclear fusion ignites and the star reaches the main sequence in the Hertzsprung-Russell diagram

(HRD), also called a Zero Age Main Sequence Star, ZAMS (Beech, 2019; Hanslmeier, 2023). The mass of the molecular gas cloud, or the amount of accreted material, determines the type of star on the main sequence (McKee & Ostriker, 2007).

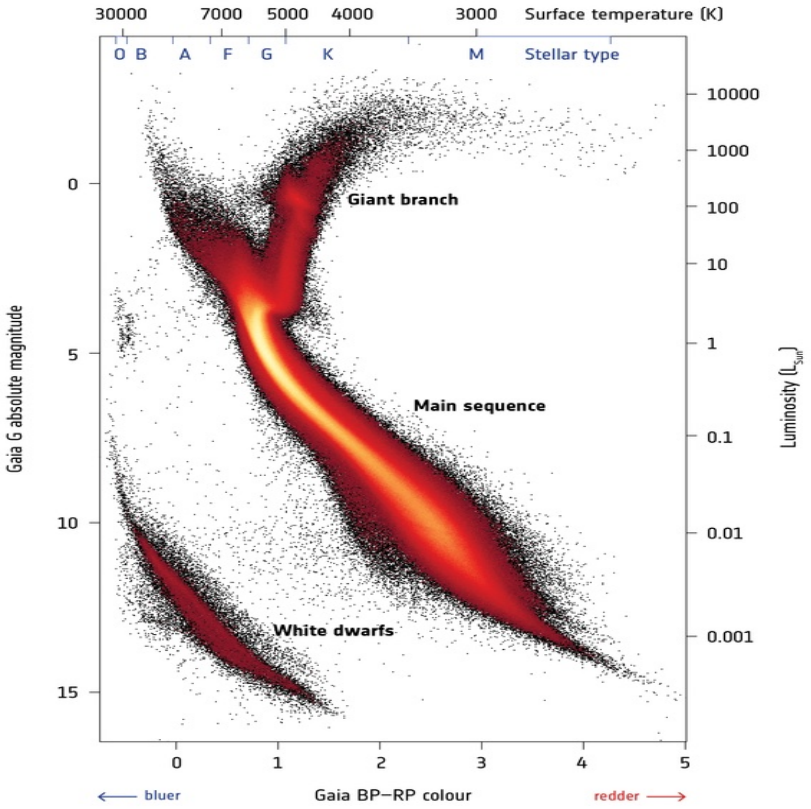


**Figure 2.1: Hertzsprung-Russell diagram from Gaia measurements.** The figure shows measurements from Gaia (ESA), characterizing the properties (Luminosity, spectral class) of around two billion stars (Copyright © ESA/Gaia/DPAC, licensed under CC BY-SA 3.0 IGO[1], no changes were made).

Figure 2.1 shows the distribution of different type of stars in the HRD measured by Gaia. Stars with less mass are cooler and appear in the lower right of the main sequence. They are called M-dwarf stars according to their spectral class, while the hotter G-type stars like the sun are located in the middle of the main sequence. The most common stars in the universe are M-type stars (Beech, 2019). Due to their cooler temperature, convection extends far into the core making them completely convective stars (Hanslmeier, 2023). Therefore, this type of star can use its entire hydrogen reservoir for nuclear fusion and together with their low luminosity, they have the longest lifetimes among main sequence stars (Hansen et al., 2004; Adams et al., 2005).

[1] Source: https://sci.esa.int/web/gaia, last visited on December 9, 2025

### Stellar spectrum

In a good approximation the radiation of a star can be described by a black body, which means a Planck curve at a certain surface temperature (Hanslmeier, 2023). The higher the temperature, the further the maximum of the radiation shifts to lower wavelengths.

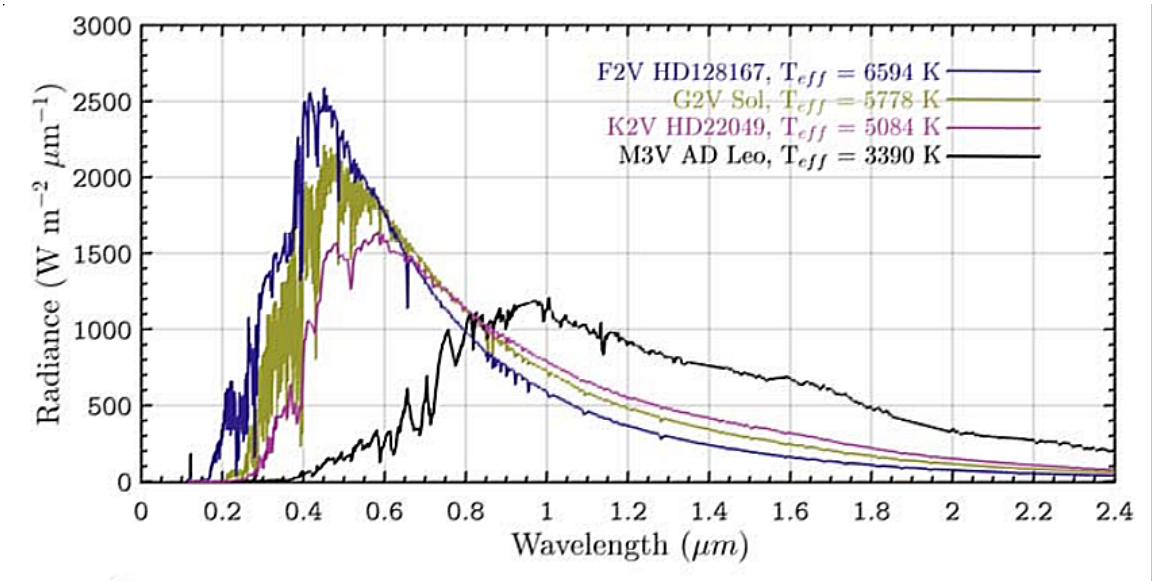


**Figure 2.2: Spectral energy distribution for different stellar types.** The figure shows the spectral energy distribution of different types of stars. G-stars (olive curve) have their maximum at around 500 nm, F-stars (blue) at around 450 nm and K-stars (magenta) at around 700 nm. The maximum of M-stars is shifted to red or infrared part of the electromagnetic spectrum (black curve). The figure is from Rushby et al. (2019), licensed under CC BY 3.0.

This can be seen in figure 2.2, where the spectral energy distribution of different types of stars is shown. Most of the total flux for G stars comes from the visible part of the spectrum (olive green curve for the Sun), while for the cooler M stars most of it comes from the infrared region (black curve). For example, the Earth at a distance of 1 AU receives a total irradiance of 1.37 kW m$^{-2}$ (Hanslmeier, 2023). Together with the stellar activity (see sec. 2.2), the different stellar spectra significantly influence the chemistry of a planet's potential atmosphere.

### Planet Formation

The surrounding disk of a young star consists of 99% gas and 1% dust and is called protoplanetary disk. The current state of research suggest, that the growth of planets

starts with small dust particles of $\mu$m size. They collide and stick together through adhesion, forming mm and cm sized particles. Further growth to meter size or planetesimals face some barriers. Bigger particles tend to bounce off during the collision process, so that it is unlikely that they stick together (bouncing barrier). In addition, the collisions can lead to fragmentation (Armitage & Kley, 2019, and references therein).

To overcome these barriers, Armitage and Kley (2019) discuss different mechanisms like the sweep-up of smaller particles (Windmark, F. et al., 2012). The presence of a few larger particles initiates this process and produces 100-m-sized bodies. In this case the bouncing boundary is useful to prevent the growth of too many large particles, which would be fragmented by collisions. Another discussed mechanism is the streaming instability (Youdin & Goodman, 2005), where density pertubations can evolve. If the density reaches a critical amount, gravitation set in and will form larger objects. Once a planetesimal is formed, the gravitational attraction leads to a fast growth of the largest objects (runaway growth) by accreting material from their surrounding. The resulting moon-sized objects form the planets due to mutual collisions over several ten million years (Armitage & Kley, 2019).

Regarding the formation mechanism and the composition of the protoplanetary disk, extrasolar planets can be very diverse with respect to their orbits or bulk densities. Up today we know of different classes of planets from rocky planets and super-Earths to ice giants or hot Jupiters (Madhusudhan et al., 2016).

#### Planetary Atmospheres

The diversity of the different planets that have formed has an influence on the formation of their atmosphere. In this thesis, the main focus is on terrestrial planets within the habitable zone of M-dwarf stars. According to Johnson et al. (2008), a planet's ability to retain atoms or molecules depends on the Jeans parameter $\lambda$, which is defined by the following equation 2.1

$$\lambda \equiv \frac{GM_p m}{k_B T r}. \tag{2.1}$$

Here, $M_p$ and $m$ are the planetary and mean molecular mass, $r$ is the distance to the exobase of the planet, where the mean free path is comparable to the atmospheric scale height (Volkov, 2017). $T$ is the temperature of the gas, $G$, the gravitational constant and $k_B$, the Boltzmann constant. For $\lambda \gg 1$, the planet can retain its atmosphere.

The first, primordial atmosphere is formed by accreting hydrogen within the stellar nebula (Lammer, 2012). Sanchez-Lavega (2010) suggested that these atmospheres are subject to constant evolution due to external influences like stellar winds or orbital changes, as well as internal influences such as interaction with the surface. Bigger planets are more resistant and it is more likely that they retain their primordial atmosphere, whereas smaller planets like Earth, Venus and Mars loose their initial atmosphere due to the higher thermal velocities of $H_2$ and He. These planets can form further atmospheres by outgassing of volatile compounds like $H_2O$, $CO_2$, $N_2$ or $SO_2$.

Table 2.1 gives an overview of the atmospheric composition of the rocky solar system planets Earth, Venus and Mars. The latter two have $CO_2$-dominated atmospheres, whereas the Earth has an $N_2$-$O_2$-dominated one, which comes mainly from the evolution of life (Sanchez-Lavega, 2010). Although there is still no direct evidence for an atmosphere around a rocky planet outside the solar system, the formation mechanisms and observations of solar terrestrial planets make it very likely that there are atmospheres around rocky planets beyond our solar system.

**Table 2.1: Atmospheric composition of rocky solar system planets.** The table provides different values of the atmospheric composition for the solar system planets Earth, Venus and Mars. The values are based on the work of Sanchez-Lavega (2010), and recent measurements for $CO_2$ and $CH_4$.

| Specie | Earth | Venus | Mars |
|---|---|---|---|
| $N_2$ | 0.7808 | 0.035 | 0.027 |
| $O_2$ | 0.2095 | 0–20 ppm[1] | 0.13 ppm |
| $CO_2$ | 425 ppm[2] | 0.965 | 0.953 |
| $CH_4$ | 1.9 ppm[2] | – | 33 ppb[3] |
| $H_2O$ | <0.03 | 50 ppm | 0–300 ppm |
| CO | 0.2 ppm | 50 ppm | 700 ppm |
| $O_3$ | 10 ppm | – | 0.01 ppm |
| NO | <0.01 ppm | – | 3 ppm |
| $N_2O$ | 0.35 ppm | – | – |
| $NO_2$ | 15 ppb | – | – |
| $SO_2$ | <2 ppb | 60 ppm | – |
| $H_2$ | 0.5 ppm | – | 10 ppm |

[1] ppm: parts per million ($10^{-6}$ mol/mol)

[2] https://gml.noaa.gov/ccgg/trends/, last visited on September 26, 2025

[3] ppb: parts per billion ($10^{-9}$ mol/mol)

### Habitable Zone

The most interesting rocky planets for current research are found in the habitable zone (HZ) of a star. This is the area around a star in which liquid water can exist on the surface and thus support the existence of life as we know it. It is highly influenced by the existence of an atmosphere and the stellar spectrum of the host star. For an atmospheric pressure of 1 bar, the surface temperature $T_s$ has to satisfy equation 2.2 (Madhusudhan et al., 2016).

$$0\,^{\circ}\mathrm{C} \leq T_s \leq 100\,^{\circ}\mathrm{C} \tag{2.2}$$

Of course, the upper limit should be below boiling point of water (100 °C). If not, the planet will face a *runaway greenhouse effect*. With increased stellar irradiation at the inner edge of the HZ, a planet crosses the Simpson-Nakajima limit (Nakajima et al., 1992), which restricts the thermal outgoing radiation on a moist planet. As a consequence, the lower atmosphere heats up without increasing thermal emission and evaporating all the liquid surface water giving an additional positive feedback for heating (Goldblatt et al., 2013). Within the hotter atmosphere, water vapor reaches higher altitudes and thus is photolyzed by the incoming UV-radiation. So, the lighter hydrogen will escape and the planet becomes dry within 10–100 million years (Bauer & Lammer, 2010; Innes et al., 2023), which explains that Venus has no significant amount of water any more.

The Outer edge of the habitable zone is is reached when $T_s$ drops permanently below the freezing point of water, so that it only occurs in solid form. The greater the distance from the star, the lower the stellar flux and thus the temperature. The carbon cycle becomes less efficient and $CO_2$ accumulates in the atmosphere and increases the temperature on the ground. However, if a planet is too far away from the host star, the $CO_2$ can condense despite a higher $CO_2$ partial pressure. This increases the reflectivity and reduces the amount of gaseous $CO_2$, which ultimately reduces the greenhouse effect and makes the planet too cold for liquid water (Kasting et al., 1993; Ramirez, 2018).

The incoming flux defines the orbital distance of the habitable zones. For G-type stars like the sun, the luminosity is higher, which leads to a greater orbital distance compared to the less luminous M-type stars (Bauer & Lammer, 2010). In order to receive a similar amount of irradiation, the HZ of M stars can be more than an order of magnitude closer to the star than the distance between Earth and Sun (Bauer & Lammer, 2010; Kopparapu et al., 2013). At such distances, it is likely, that the planets are tidally locked due to tidal forces slowing down the planetary rotation (Dole & Asimov, 1964).

### Vertical Temperature Profile

The vertical temperature distribution of a planet's atmosphere is determined by the incoming stellar flux and the atmospheric composition. The parameter to describe this vertical structure in the tropospheric layer is the lapse rate $\Gamma(z) = dT/dz$. Figure 2.3 shows the vertical temperature profile of the terrestrial (rocky) planets in the solar system.

The lowest layer is called the troposphere and extends on Earth up to a height of about 10–20 km. Above this, the stratosphere begins with $\Gamma > 0$, caused by the UV and IR absorption of $O_3$. The mesosphere begins at around 50 km and extends to ~90 km with a decrease in temperature. Above this are the thermosphere and the ionosphere. Mars and Venus have no ozone layer and therefore the mesosphere begins directly after the troposphere (~45 km for Mars, ~70 km for Venus) and above it the thermosphere (Sanchez-Lavega, 2010).

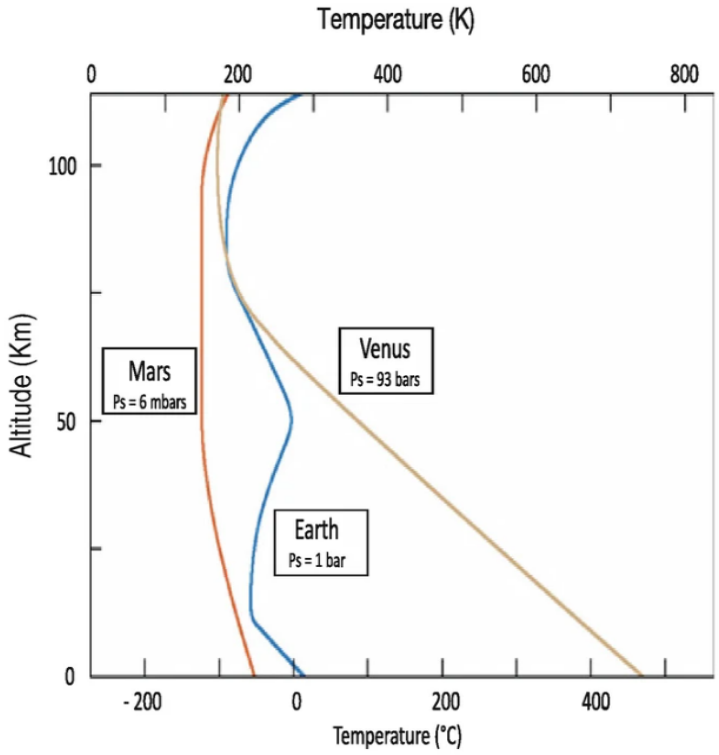


**Figure 2.3: Temperature profiles for the terrestrial solar system planets.** The figure shows the vertical temperature profile of the rocky solar system planets Venus (almond), Earth (blue) and Mars (orange). Earth's profile is characterized by the heated stratosphere at ~12 km due to the ozone layer. Mars and Venus, on the other hand, have no stratosphere, which is why the mesosphere follows directly after the troposphere (the figure is from Encrenaz and Coustenis (2018)[2]).

[2] Reproduced with permission from Springer Nature. CCC License No. 6065860348041

After introducing the theory of the formation of stars, planets and their atmospheres in the previous section, the upcoming section focuses on stellar activity and particle precipitation.

## 2.2 Stellar Activity and Particle Precipitation

The evolution of planetary atmospheres is strongly related to the stellar radiation and particle environment. Stellar extreme UV (EUV) radiation triggers (photo)ionization and affects the temperature of the upper atmosphere (Bauer & Lammer, 2010). In figure 2.4 it is shown that EUV radiation affects Earth's atmosphere mainly above 110 km. By observing the sun and applying it to other main sequence stars, it is suggested that they also reduce their mass due to a stellar wind. This continuous wind consists of a plasma with high kinetic energy, can spread out from the star and influences planetary atmospheres in the near neighborhood (Johnstone, C. P. et al., 2015). By contrast, it reduces the angular momentum and influences the rotation of the star over time (Vidotto, 2021).

According to Müller et al. (2006), the stellar wind drives the astrosphere of a star, which separates the inner stellar system from the outside interstellar medium (ISM) and shields it from high fluxes of galactic cosmic rays (GCRs). GCRs are another source of high energetic particles and are the relics of supernovae from outer space (Herbst et al., 2019a). Recent work using a 1D transport code suggests that the flux of galactic cosmic rays (GCRs) within the astrosphere of less active or inactive host stars is higher and therefore has to be considered as a relevant component of the particle flux, which is especially the case for LHS 1140 and its planet LHS 1140 b (Herbst et al., 2020).

At the shock front of local coronal mass ejections (CMEs), charged particles are accelerated and impact their neighborhood with potentially higher energy (Reames, 1999). These energetic particles accompanied by CMEs are known as stellar energetic particles (SEPs). Since lower-mass stars such as M-dwarfs tend to be fully convective in their interiors compared to G-type stars, stellar activity is increased, exposing the nearby habitable zone to higher particle fluxes due to more extreme SEP events (Herbst et al., 2020).

SEPs and GCRs are the main contributors to the particle flux that influence the atmosphere of a planet in a stellar system (Herbst et al., 2019a). Mironova et al. (2015) gives an overview on processes during the precipitation of energetic particles in Earth's atmosphere. According to their energy, these particles penetrate the atmosphere to different heights. GCRs, consisting of protons, can reach energies from MeV to TeV or even higher and are

responsible for ionization in the lower atmosphere. SEPs are less energetic (typically 10 – 100 MeV) and primarily composed of protons (> 90%). They ionize the middle atmosphere above ~25 km , which is shown by the blue area in figure 2.4.

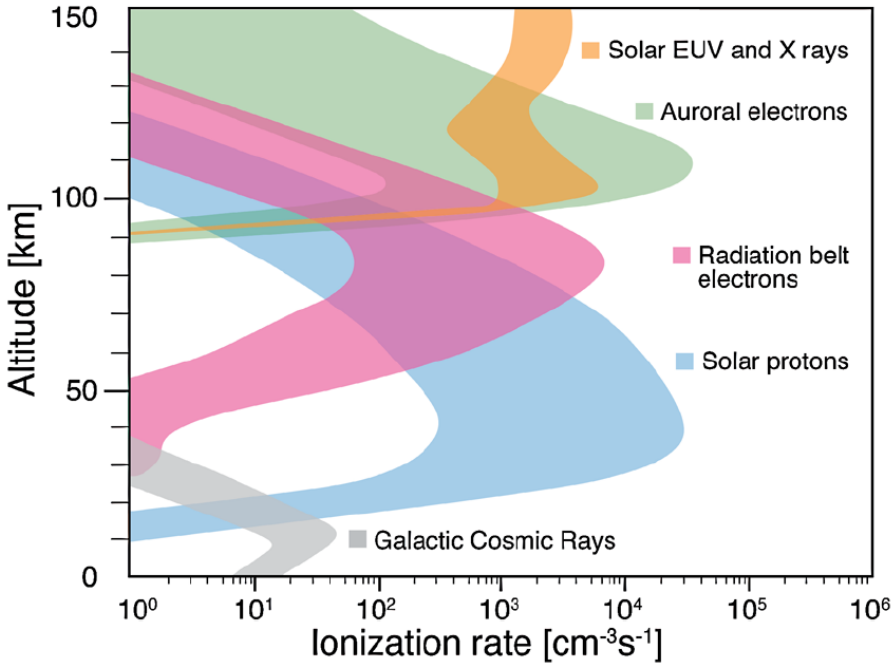


**Figure 2.4: Overview of the particles penetrating into Earth's atmosphere.** Here, the main sources for ionization in the Earth's atmosphere are shown. Depending on their energy they can penetrate to higher or even lower altitudes. EUV-, X-ray radiation (orange) and auroral electrons (green) affect the upper atmosphere, while faster electrons (red), which are accelerated in the radiation belts, protons (blue) and GCRs (gray) reach altitudes below 100 km. The figure was adapted by Mironova et al. (2015)[3] and is from Baker et al. (2012).

Not only Earth experiences the impact of stellar particles. Nordheim et al. (2015) simulates the effects of SEPs and GCRs on the atmosphere of Venus using a 3D Monte Carlo method that also takes heavier ions into account. It provides a better estimate of the ionization rates of GCRs and SEPs, especially for the most relevant altitudes below 100 km. Thus, it is suggested that they will also have an impact on atmospheric chemistry.

Furthermore, this can also be extended to extrasolar systems, where recent estimates propose that the particle flux of SEP events of M-stars could be orders of magnitudes higher than for G-type stars (Herbst et al., 2019b). So it is crucial to investigate the ionizing character of GCRs and SEPs that impact the atmospheric composition of potential

[3] Reproduced with permission from Springer Nature. CCC License No. 6064910157600

atmospheres around M-stars (Herbst et al., 2019a). Thus, the next section provides an overview of the main (ion)chemical processes.

## 2.3 Atmospheric Chemistry and the Influence of Stellar Energetic Particles and Galactic Cosmic Rays

The composition of the atmosphere is driven mainly by photochemistry due to the incoming stellar electromagnetic radiation. In addition to these photochemical reactions, the high-energy particle environment plays an important role in the formation of charged species, which are a significant part of atmospheric chemistry, particularly at higher altitudes. This section discusses the principles of atmospheric ion chemistry and introduces major influences on trace gases of the neutral atmosphere.

### 2.3.1 Principles of Atmospheric Ion Chemistry

Beginning with Earth-like atmospheres consisting mainly of molecular nitrogen ($N_2$) and oxygen ($O_2$), the impact of stellar energetic particles has been studied since the 60s and early 70s of the last century. SEPs collide with the abundant species $N_2$, $O_2$ and O in the mesosphere and He or H in the thermosphere, depositing their energy and leading to ionization (R. Jones & Rees, 1973). Below the mesosphere, mainly $N_2$ and $O_2$ are ionized (Porter et al., 1976; Rusch et al., 1981). R1 to R7 show the reactions in which an incoming energetic particle $\boldsymbol{x}^*$ (proton, (auroral) $e^-$) interacts with the most abundant species $N_2$, $O_2$ and O. These reactions can be both dissociative and ionizing and can also create an excited electronic state N($^2$D,$^3$P) or ground state N($^4$S), especially in the case of atomic nitrogen N (R. Jones & Rees, 1973; Porter et al., 1976).

$$O_2 + \boldsymbol{x}^* \longrightarrow O + O + \boldsymbol{x}^* \tag{R1}$$

$$O_2 + \boldsymbol{x}^* \longrightarrow {O_2}^+ + \boldsymbol{x}^* + e^- \tag{R2}$$

$$O_2 + \boldsymbol{x}^* \longrightarrow O^+ + O + \boldsymbol{x}^* + e^- \tag{R3}$$

$$O + \boldsymbol{x}^* \longrightarrow O^+ + \boldsymbol{x}^* + e^- \tag{R4}$$

$$N_2 + \boldsymbol{x}^* \longrightarrow N + N + \boldsymbol{x}^* \tag{R5}$$

$$N_2 + \boldsymbol{x}^* \longrightarrow {N_2}^+ + \boldsymbol{x}^* + e^- \tag{R6}$$

$$N_2 + \boldsymbol{x}^* \longrightarrow N^+ + N + \boldsymbol{x}^* + e^- \tag{R7}$$

As can be seen from the reaction equations, free electrons are released during the ionization processes, which can initiate new ionizations if they still have sufficient energy. The average kinetic energy of the background then determines when the processes come to an end (Sinnhuber et al., 2012).

According to Sinnhuber et al. (2012), the formation rate P of a primary ion $c^+$ concerning the total ion pair production rate (IPR) is given by

$$P(c^+) = \frac{\sigma_c^+ \cdot [C] \cdot IPR}{Q_{tot}} \tag{2.3}$$

where [C] represents the abundance of a target specie, $\sigma_c^+$ is the cross-section of forming an ion $c^+$ and $Q_{tot}$ is the total produced charge, which can be calculated by 2.4.

$$Q_{tot} = \sum_i \sigma_{tot,i} \cdot [C_i] \tag{2.4}$$

The IPR contains the energy release of the energetic particles propagating through the atmosphere, which can be calculated by the Bethe-Bloch formula. In ExoTIC, $Q_{tot}$ is calculated by 2.5 (see also Table 3.2).

$$\begin{aligned} Q_{tot} = {} & 0.8978 \cdot [N_2] + 1.0 \cdot [O_2] + 0.56 \cdot [O] \\ & + 0.89 \cdot 1.2 \cdot [CO_2] + 0.68 \cdot [H_2O] + 0.21 \cdot [H_2] \end{aligned} \tag{2.5}$$

#### Effects on $NO_x$ Species

The effect of ion chemistry depends on the interacting species. Due to the large amount of nitrogen in Earth-like atmospheres, the impact of particle precipitation is dominated by the formation of short-lived N-containing species (e.g., $NO_x$=N, NO, $NO_2$ or $HNO_3$). Based on the initial reactions R1 to R7, the positive ions of $N_2$, $O_2$, N and O or the excited state of N are the source for forming $NO_x$ (see R8) mainly in the middle atmosphere and thermosphere (Sinnhuber et al., 2012).

$$N(^2D, ^3P) + O_2 \longrightarrow NO + O \tag{R8}$$

According to R. Jones and Rees (1973) and Nicolet (1975) these ions take part in several neutral-ion (R9-R13) or recombination reactions (R14 and R15), forming also the excited states N($^2$D,$^3$P) or the ground state N($^4$S) of N.

$$O^+ + N_2 \longrightarrow NO^+ + N(^4S) \tag{R9}$$

$$O_2{}^+ + N_2 \longrightarrow NO^+ + O \tag{R10}$$

$$O_2{}^+ + N(^4S) \longrightarrow NO^+ + O \tag{R11}$$

$$N_2{}^+ + O \longrightarrow NO^+ + N(^4S) \tag{R12}$$

$$N^+ + O_2 \longrightarrow NO^+ + O \tag{R13}$$

$$NO^+ + e^- \longrightarrow O + N(^4S, {}^2D) \tag{R14}$$

$$N_2{}^+ + e^- \longrightarrow N + N(^4S, {}^2D, {}^3P) \tag{R15}$$

Another important type of reaction is the charge transfer involving $N^+$ (Nicolet, 1975) and $O_2^+$ (R. Jones & Rees, 1973), given by the chemical equations R16 and R17.

$$N^+ + O \longrightarrow O^+ + N \tag{R16}$$

$$O_2{}^+ + NO \longrightarrow NO^+ + O_2 \tag{R17}$$

Regarding the above equations it can be seen that recombination is the most important sink for $NO^+$ ions (Sinnhuber et al., 2012). Rusch et al. (1981) suggests that neutral NO can be formed by reactions R18 and R20 in which atomic nitrogen is present either in the ground state N($^4$S) or in the excited state N($^2$D). The latter dominates production in the strato- and mesosphere, as these reactions are strongly dependent on temperature.

$$N(^4S) + O_2 \longrightarrow NO + O \tag{R18}$$

$$N(^4S) + NO \longrightarrow N_2 + O \tag{R19}$$

$$N(^2D) + O_2 \longrightarrow NO + O \tag{R20}$$

Furthermore, the different electronic states of atomic nitrogen are removed from the atmosphere by reacting with NO forming again $N_2$ and atomic oxygen. The NO molecules

formed by these reactions are the main driver for ozone loss (see section 2.3.2) in Earth's stratosphere due to energetic particle precipitation (Crutzen et al., 1975).

#### Nitrous Oxide

On Earth, Nitrous oxide ($N_2O$) is a greenhouse gas and the decomposition products can destroy the ozone layer (Kelly et al., 2018), but it can be also treated as a biosignature in exoplanetary atmospheres (Grenfell, 2018). Thus, the abiotic sources of $N_2O$ are of potential interest for interpreting future observations. Zipf and Prasad (1980) discuss the production of $N_2O$ by charged particles in the upper atmosphere. Hence, molecular nitrogen changes to an excited electronic state $N_2(A^3\Sigma_u^+)$ and can react with $O_2$, forming $N_2O$ (see R21).

$$N_2(A^3\Sigma_u^+) + O_2 \longrightarrow N_2O + O \tag{R21}$$

Semeniuk et al. (2008) suggests another possible pathway of producing $N_2O$ during energetic particle events in the upper atmosphere via reaction R22, following after the dissociation of $N_2$. There, this reaction is used to explain the enhanced $N_2O$ concentrations measured at ~70 km by the ACE-FTS instrument.

$$N + NO_2 \longrightarrow N_2O + O. \tag{R22}$$

Sheese et al. (2016) extended the ACE-FTS data up to ~95 km and showed that $N_2O$ is also produced by R21 in the lower thermosphere. For the first time, Kelly et al. (2018) implemented all reactions R21–R24 in the chemistry-climate model WACCM (**W**hole **A**tmosphere **C**ommunity **C**limate **M**odel) in order to match the observed higher $N_2O$ concentrations with the model results. For that, the authors used a branching ratio of 0.5% for the $N_2O$ reaction path (R21). The other 99.5% are attributed to reaction R24.

$$N_2(A^3\Sigma_u^+) + O \longrightarrow N_2(X^1\Sigma_g^+) + O \tag{R23}$$

$$N_2(A^3\Sigma_u^+) + O_2 \longrightarrow N_2(X^1\Sigma_g^+) + 2\,O \tag{R24}$$

To conclude on that, the significant amount of $N_2$ at higher altitudes of Earth-like atmospheres can initiate the abiotic production of nitrous oxide ($N_2O$) by energetic particles. As it is considered a trace gas for biotic activity on planets, the abiotic sources could be relevant to exclude possible false positive signals in observations of extrasolar planets.

### Effects on $HO_x$ Species

According to Solomon et al. (1981), $HO_x$(H, OH, $HO_2$) species are also formed by energetic particles, but unlike $NO_x$, which is also a product of $N_2$ dissociation, they are formed only via complex ion chemical reactions involving large cluster ions. The initial energetic particles provide $O_2^+$ ions and they can form $O_4^+$ ions involving a third body M (see R25). The resulting ions consume surrounding water vapor to build up so-called cluster ions.

$$O_2{}^+ + O_2 + M \longrightarrow O_4{}^+ + M \tag{R25}$$

$$O_4{}^+ + H_2O \longrightarrow O_2{}^+(H_2O) + O_2 \tag{R26}$$

$$O_2{}^+(H_2O) + H_2O \longrightarrow H^+(H_2O) + OH + O_2 \tag{R27}$$

By reacting with more water vapor, also cluster ions containing a proton $H^+$ can be formed (R27). During this reaction path an OH molecule will be created. Additional water forms bigger cluster ions containing $n \cdot H_2O$ molecules and then releases one H atom via the recombination reaction R28.

$$H^+(H_2O)_n + e^- \longrightarrow H + n \cdot H_2O \tag{R28}$$

At higher altitudes above 70 km the larger electron density is responsible for recombination of the water cluster ions, whereas at lower altitudes negative ions become more abundant. This could be for example $NO_3^-$ and can remove $HO_x$ from the atmosphere by the reaction chain R29 and R30 (Solomon et al., 1981).

$$H^+(H_2O)_n + NO_3{}^- \longrightarrow HNO_3 + n \cdot H_2O \tag{R29}$$

$$HNO_3 + OH \longrightarrow H_2O + NO_3 \tag{R30}$$

Kazil et al. (2003) proposed a different way to form the protonised water cluster ions $H^+(H_2O)$ by attaching water vapor to $NO^+$ ions (see R31).

$$NO^+(H_2O)_3 + H_2O \longrightarrow H^+(H_2O)_3 + HNO_2 \tag{R31}$$

$HO_x$ can only be created in altitudes where water vapor is a significantly abundant trace species and therefore becomes less important above 85 km (Sinnhuber et al., 2012).

Nevertheless, like $NO_x$, it has an impact on the ozone budget in the mesosphere (Bates & Nicolet, 1950).

### 2.3.2 Atmospheric Ozone

Atmospheric Ozone ($O_3$) plays a major role when it comes to habitability. If its abundance is significant, the planet's surface will be protected from harmful UV radiation. Chapman (1932) was the first to explain the theory of the ozone inventory. The so-called Chapman mechanism is initiated by the photolysis of $O_2$ by UV radiation ($\lambda < 240\,\text{nm}$). The atomic oxygen then will form $O_3$ in a three body collision via reaction R33.

$$O_2 + h\nu \longrightarrow O + O \tag{R32}$$

$$O + O_2 + M \longrightarrow O_3 + M \tag{R33}$$

$$O_3 + h\nu \longrightarrow O_2 + O \tag{R34}$$

$$O_3 + O + M \longrightarrow 2\,O_2 + M \tag{R35}$$

Ozone is photochemically active and absorbs harmful UV radiation (see R34). Depending on the wavelength of the photons, either a $O(^1D)$ radical ($\lambda < 310\,\text{nm}$) or a ground state O ($310\,\text{nm} < \lambda < 1140\,\text{nm}$) is created (see Kozakis et al., 2022). $O(^1D)$ can be then quenched back to O or oxidizes other species in the stratosphere/mesosphere. The $O_3$ formation (R33) quickly consumes the atomic oxygen. Thus, the sink of $O_3$ is reaction R35, where the sum of O and $O_3$ is denoted as odd oxygen $O_x$ (Kozakis et al., 2022).

As briefly mentioned above, $HO_x$ and $NO_x$ have an influence on the ozone budget. Both families act in catalytic cycles to destroy significant amount of $O_3$. For $HO_x$ (R36–R38), this catalytic cycle is important at higher altitudes above 60 km (Bates & Nicolet, 1950).

$$H + O_3 \longrightarrow OH + O_2 \tag{R36}$$

$$\underline{OH + O \longrightarrow H + O_2} \tag{R37}$$

$$\textbf{net:}\;\; O_3 + O \longrightarrow 2\,O_2 \tag{R38}$$

Crutzen (1970) suggests that in the altitudes below (25 km–40 km), an important sink of odd oxygen ($O_x$) species is due to the $NO_x$ family. The reactions of the corresponding

catalytic cycle are shown in R39–R41. As explained above, the initial NO for this cycle can be produced by energetic particles or additionally by the photolysis of $NO_2$.

$$NO + O_3 \longrightarrow NO_2 + O_2 \tag{R39}$$

$$\underline{NO_2 + O \longrightarrow NO + O_2} \tag{R40}$$

$$\textbf{net:}\ \ O_3 + O \longrightarrow 2\,O_2 \tag{R41}$$

Furthermore, $N_2O$, which is also formed during energetic particle events, serves as a reservoir species for NO and is produced via the reaction of $O(^1D)$ with $N_2O$ (Crutzen et al., 1975).

For the sake of completeness, it should also be mentioned at this point that ozone depletion in the Earth's stratosphere is also catalyzed by reactive halogen species like chlorine (Cl), which originates from anthropogenic sources. This mechanism was first described theoretically by Molina and Rowland (1974) and is based on the same principle as the $NO_x$ catalytic cycle. R42–R44 show the efficient reaction chain, which consumes an $O_3$ molecule.

$$Cl + O_3 \longrightarrow ClO + O_2 \tag{R42}$$

$$\underline{ClO + O \longrightarrow Cl + O_2} \tag{R43}$$

$$\textbf{net:}\ \ O_3 + O \longrightarrow 2\,O_2 \tag{R44}$$

Since Cl is a very long-lived species (40 – 150 years) and is not consumed in the catalytic cycle, many $O_3$ molecules can be destroyed. This is the main driver of the antarctic ozone hole, which was discovered by Farman et al. (1985).

### 2.3.3 Ionization in more Exotic Atmospheres

The diversity of various types of atmospheres also includes those with significant amount of carbon dioxide (e.g. Mars and Venus). Thus, the initial impact of energetic particles mainly affects $CO_2$ and lead to its ionization or dissociation (R45 – R47, (Itikawa, 2002; Herbst et al., 2024)).

$$CO_2 + \boldsymbol{x}^* \longrightarrow {CO_2}^+ + e^- + \boldsymbol{x}^* \tag{R45}$$

$$CO_2 + \boldsymbol{x}^* \longrightarrow CO^+ + O + e^- + \boldsymbol{x}^* \tag{R46}$$

$$CO_2 + \boldsymbol{x}^* \longrightarrow CO + O + \boldsymbol{x}^* \tag{R47}$$

Recombination of $CO_2^+$ via R48, where $X^-$ denotes a negative charged particle (ion or $e^-$), delivers a source of atomic oxygen in the atmosphere (Sinnhuber et al., 2012).

$$CO_2{}^+ + X^- \longrightarrow CO + O \tag{R48}$$

In the Martian atmosphere, the charge exchange reaction R49 creates ionized molecular oxygen $O_2^+$, which is the initial source for forming water cluster ions and the release of $HO_x$ species (see 2.3.1 and Nakamura et al. (2023)) leading to ozone loss besides the photolysis of water vapour (Määttänen et al., 2022, and references therein)

$$CO_2{}^+ + O_2 \longrightarrow O_2{}^+ + CO_2 \tag{R49}$$

Additional to the ion-chemistry, photolysis of $CO_2$ plays an important role in the Martian atmosphere for providing atomic oxygen to initiate the Chapman mechanism for ozone production (Määttänen et al., 2022). $CO_2$ is photolyzed by photons with $\lambda < 202\,\text{nm}$ (see R50).

$$CO_2 + h\nu \longrightarrow CO + O \tag{R50}$$

According to Ranjan et al. (2023), the UV flux of M-dwarf stars in the corresponding wavelength range is higher compared to the sun, which increases the efficiency for splitting $CO_2$ apart. This study suggests, that it is unlikely to accumulate molecular oxygen by the photolysis of $CO_2$, but can't rule out the possibility that $O_3$ is detectable by observations with the James Webb Space telescope (JWST).

#### $H_2$ and $H_2O$

Besides $CO_2$-dominated atmospheres, there could be also atmospheres of heavier planets in which $H_2$ and $H_2O$ are the dominant trace gases. Thus, their ionization plays a more important role. The reactions with energetic particles are shown in equations R51 to R55 (Itikawa & Mason, 2005; Straub et al., 1996).

$$H_2 + \boldsymbol{x}^* \longrightarrow H_2{}^+ + e^- + \boldsymbol{x}^* \tag{R51}$$

$$H_2 + \boldsymbol{x}^* \longrightarrow H^+ + H + e^- + \boldsymbol{x}^* \tag{R52}$$

$$H_2O + \boldsymbol{x}^* \longrightarrow OH^+ + H + e^- + \boldsymbol{x}^* \tag{R53}$$

$$H_2O + \boldsymbol{x}^* \longrightarrow H^+ + OH + e^- + \boldsymbol{x}^* \tag{R54}$$

$$H_2O + \boldsymbol{x}^* \longrightarrow {H_2}^+ + O + e^- + \boldsymbol{x}^* \tag{R55}$$

$$H_2O + \boldsymbol{x}^* \longrightarrow O^+ + H_2 + e^- + \boldsymbol{x}^* \tag{R56}$$

However, these types of atmospheres can be found on terrestrial planets only in their early phase, but on more massive planets they are more common. The ionization of water vapor contributes to the formation of $HO_x$ species. Regarding $H_2$-dominated atmospheres, Rimmer and Helling (2013) suggests an increased electron density in the upper atmosphere by energetic particles, which impacts the ionosphere of such planets. Additionally, the dissociative ionization of $H_2$ facilitates escape of $H/H^+$ in the thermosphere.

### 2.3.4 Reaction Rate

The concentrations for ion and neutral chemical reactions are subject to reaction kinetics. For a reaction of type $A + B \rightarrow C$, the change in the concentration of specie C over time (reaction rate) is given by

$$v = \frac{d[C]}{dt} = k(T) \cdot [A] \cdot [B], \tag{2.6}$$

where $k(T)$ denotes the rate constant and [C] the number density of specie C (Mickey, 1980). The rate constant is either a constant or can be calculated by the Arrhenius equation 2.7

$$k(T) = A \cdot \exp\left(\frac{-E_a}{RT}\right) \tag{2.7}$$

$E_a$ represents the activation energy, R is the universal gas constant (8.314 J/mol K), and A is the individual constant Arrhenius prefactor (Laidler, 1984). In climate chemistry models, changes in the concentration of a species are calculated numerically as the balance between production and loss (see chapter 3).

## 2.4 Observation of Exoplanetary Atmospheres

At the beginning of exoplanetary research, extrasolar planets must first be discovered in order to be able to characterize them at a later stage. Encrenaz and Haghighipour (2020) reviews various methods that are used for this purpose and where the most common are shortly introduced in the following. A system of planet and star orbits a common center of mass, which also leads to a movement of the star itself. This movement shifts the spectrum of the star according to the Doppler effect. By measuring the spectrum, one can obtain the radial velocity of the star and use it to determine the mass of the orbiting planet. This method is therefore often referred as the radial velocity method. Another technique for exoplanet detection is the so-called transit method. A periodic dip in the measured stellar flux indicates the existence of a planet. The method can be also used for the characterization of exoplanetary atmospheres, which will be described in section 2.4.1. In contrast, extrasolar planets can be detected by direct imaging. This method is quite challenging, because the emitted flux of the planet is very small compared to the star. Since most star systems do not carry out transits, this method will become increasingly important in the future as soon as it is technically advanced enough.

Advancing technology and more precise measurement methods based on knowledge from Earth observation open up the possibility of characterizing the atmospheres of planets around other stars. Recent and past space telescope missions like James Webb (JWST) and Hubble (HST) use transit spectroscopy to characterize exoplanetary atmospheres in the visible or infrared spectrum.

### 2.4.1 Transmission Spectroscopy

A detailed overview of the transit method, following Roberge and Seager (2018), is described in this section. If the conditions and geometry are favorable, a planet orbiting its host star can pass between star and the line of sight of the observer. The planet covers a part of the star disk, similar to a solar eclipse on Earth. When measuring the brightness as a function of time, this will result in a decrease during the transit, which is related to the planet-to-star ratio of the radii. This can be seen in figure 2.5 for the hot gas giant WASP-96b, where the line of datapoints is called light curve. It can be measured for different wavelengths.

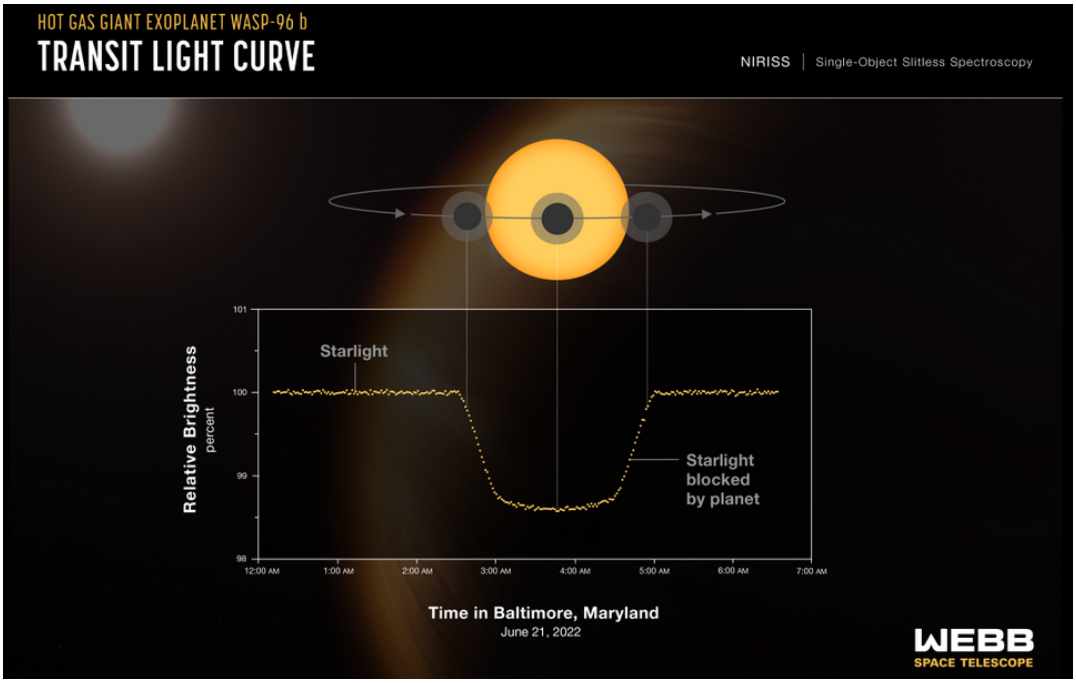


**Figure 2.5: Principle of transit observations.** The illustration shows most common method for analyzing the atmosphere of extrasolar planets. A transiting planet blocks parts of the received stellar flux. Depending on its size, the dip in the light curve is deeper and thus it is easier to obtain a spectrum if the planet to star ratio is bigger. An atmosphere around the rocky core changes the effective size of the planet. Depending on the abundance of atmospheric gases, which absorb light differently at certain wavelengths, the planetary radius appears to vary with wavelength (Credit: NASA, ESA, CSA, STScI. Lisence: public domain[4].)

Both the fixed planetary diameter and the surrounding atmosphere contribute to the minimum of this light curve. Due to absorption of the transmitted starlight, the atmospheric contribution to the planetary radius varies with wavelength, which can be plotted as a Transmission spectrum. This kind of spectral analysis is sensitive to thin atmospheres, or to the upper parts of dense atmospheres. Mathematically, the measured relative brightness can be expressed by the transit depth T,

$$T = \frac{\Delta F}{F_\star} = 1 - \left(\frac{F_{trans}}{F_\star}\right) = \left(\frac{R_p}{R_\star}\right)^2 . \tag{2.8}$$

$F_{trans}$ represents the flux at the bottom of the light curve dip, and $F_\star$ is the flux of the host star. Without an atmosphere, the transit depth is simply given by the ratio of the planetary radius and the star.

[4] Source: https://webbtelescope.org/contents/media/images/2022, last visited on December 9, 2025.

Including an atmosphere, the transit depth is wavelength-dependent and is determined by the absorption within an atmospheric annulus of width $R_{ann}$ (transparent ring in Fig. 2.5). Thus, the planetary radius $R_p$ gets an additional contribution, which depends on the wavelength (see 2.9). This sum is known as the effective radius $R_{eff}$. The transit depth

$$R_{eff}(\lambda) = R_p + R_{ann} \cdot \left(1 - \frac{F_{ann}(\lambda)}{F_\star(\lambda)}\right) \tag{2.9}$$

$\frac{F_{ann}(\lambda)}{F_\star(\lambda)}$ is the flux ratio, which is transmitted through the area of the annulus. If there is no atmosphere ($F_{ann} = F_\star$), $R_{eff}$ would equal $R_p$. Inserting $R_{eff}$ (2.9) into equation 2.8, the transit depth would be

$$T(\lambda) = \left(\frac{R_{eff}}{R_\star}\right)^2 = \left(\frac{R_p}{R_\star}\right)^2 + \left(\frac{2R_P R_{ann}}{R_\star^2}\right) - \left(\frac{2R_p R_{ann}}{R_\star^2}\right) \cdot \left(\frac{F_{ann}(\lambda)}{F_\star(\lambda)}\right). \tag{2.10}$$

Since $R_{ann} \ll F_\star$, the ratio $R_{ann}^2/R_\star^2$ can be neglected. The trace gases within the atmosphere increase the transit depth and show up as peaks in the transmission spectra, which can be attributed to certain absorption bands. As this method is very useful, it is used in the only space-based telescopes currently available, HST and JWST. The following section contains some general information and examples.

### 2.4.2 Currently Operating Instruments

In order to avoid the influence of the Earth's atmosphere, it makes sense to move the observation of exoplanets into space. HST and JWST have made it possible to do just that since the 90s of the last century using different wavelength ranges. HST operates in the visible and near-IR, whereas JWST covers the near infrared and infrared (IR) region.

To illustrate the power of JWST compared to HST, figure 2.6 shows the same cosmic structure for both instruments. JWST observation on the right is sharper and more detailed than HST on the left.

**Figure 2.6: Comparison between HST and JWST.** The pictures show the pillars of creation in the eagles nebula of the constellation serpens observed with the two different space telescopes Hubble (left) and James Webb (right). The IR instruments of JWST reveal more details, penetrate through the cosmic dust and have an even higher resolution compared to Hubble. This demonstrates the capabilities of JWST (Credit: NASA, ESA, CSA, STScI, Hubble Heritage Project (STScI, AURA). License: public domain[5]).

IR radiation can better penetrate dust clouds and reveals the inner part of star formation regions. Due to the cosmic redshift, IR observations are able to look deeper into the universe than ever before.

JWST consists of four different instruments, three of which are designed for the near-infrared range from 0.6 $\mu$m to $\sim$ 5 $\mu$m (NIRCam (Rieke et al., 2003), NIRSpec (Jakobsen, P. et al., 2022) and NIRISS (Doyon et al., 2012)) and one for the mid-infrared range from 4.9 $\mu$m to $\sim$ 27.9 $\mu$m (MIRI (Glasse et al., 2015)). NIRSpec and NIRISS are spectrographs specifically designed for spectroscopy of transiting extrasolar planets. MIRI shifts the observing capabilities to even longer wavelengths, where IR-absorbing species like $O_3$ have their maximum.

According to the JWST mission description by Gardner et al. (2006), the IR observations require very cool instruments in order to prevent interference with radiation from the telescope itself. Thus it orbits the 2$^{nd}$ lagrange point (L2) of the Sun-Earth system, where the Sun, Earth and Moon can be shielded in the back. The side facing the sun supplies the

[5] Source: https://webbtelescope.org/contents/media/images/2022/, last visited on December 9, 2025.

energy for the electrical devices via the solar panels and, due to the quasi-stable L2, JWST requires almost no fuel except for orbit corrections. Furthermore, long-term observations can be made in L2, as there are no sunrises and sunsets or planets in between. An example of a Transmission spectrum obtained by JWST is given in figure 2.7 for the Jupiter-like extrasolar planet WASP-39b. The data was recorded by the NIRSpec PRISM instruments of JWST in the near-IR/IR range of the electromagnetic spectrum.

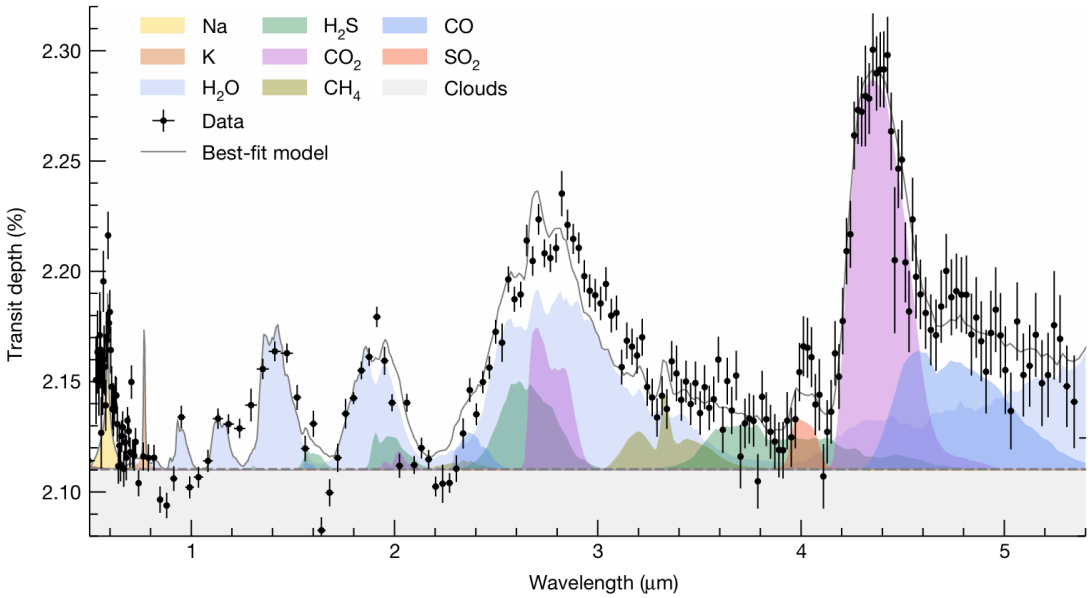


**Figure 2.7: Example of a Transmission spectrum obtained from JWST NIRSpec.** Here, the variation of the transit depth (transmission spectrum) of the Jupiter-sized exoplanet WASP-39b is shown. The data is obtained by the NIRSpec PRISM instrument of the James Webb Space telescope in the near-IR/IR wavelength range (black datapoints with $1\sigma$ uncertainty) and fitted with a radiative transfer code (grey line). The colors represent the absorption features of different species at different wavelengths. One can clearly see the $CO_2$ peak (magenta) at 4.3 $\mu$m. The figure is from Rustamkulov et al. (2023), licensed under CC BY 4.0).

At 1.4 $\mu$m, 1.9 $\mu$m and $\sim$ 2.8 $\mu$m one can clearly see the contribution of water vapor to the absorption within the atmosphere. The prominent $CO_2$ feature at 4.3 $\mu$m and a small contribution from $SO_2$ at $\sim$ 4 $\mu$m can be seen as well.

But the most promising application of the four instruments carried by JWST is the characterization of exoplanetary atmospheres. Most of the species related to life absorb in the IR bands of the electromagnetic spectrum. So JWST opens up the possibility to detect $CO_2$, $CH_4$, $H_2O$, $O_3$ or $N_2O$.

# 3 Methods

This chapter will provide an overview of the different models used in this thesis. It starts with a detailed workflow description of the 1D ion chemistry model ExoTIC with its neutral and ion chemistry modules and then explains the scientific and technical developments carried out as part of this work. Then it moves on to an overview of the other models used within the INCREASE project (see section 3.2, Herbst et al. (2022) and Herbst et al. (2019a)). They are used to generate the starting atmospheres and provide ionization rates to exploit the ion chemistry.

## 3.1 The Ion Chemistry Model ExoTIC

The **Exo**planetary **T**errestrial **I**on **C**hemistry model (ExoTIC) is a 1D stacked box model that calculates both the neutral and ion composition of different atmospheres, but does not consider diffusion and horizontal or vertical transport (Borthakur, 2025). Thus, ExoTIC can only be used for calculating atmospheric changes on short timescales (several days) that are smaller than the mixing lifetimes (Winkler, 2008). ExoTIC is therefore well-suited for model experiments of the immediate and short-term impact of energetic particle events on atmospheric composition.

The latest development also includes the possibility of modeling planets other than Earth, especially rocky exoplanets (Herbst et al., 2022). ExoTIC consists of two modules: the neutral chemistry module adapted from Chipperfield (1999) and the ion chemistry module of the University of Bremen Ion Chemistry (UBIC) model, which was first developed for the terrestrial D-region (Winkler et al., 2009; Winkler, 2008). Ion chemistry models are necessary for studying the impact of energetic particles on the atmospheric composition in detail.

### 3.1.1 Overall Model Workflow

Before starting with the actual chemical calculations, different input data need to be prescribed within ExoTIC. On the one hand, these are the initial atmospheric temperature and pressure profiles, which determine ExoTIC's vertical extent of currently 100 levels. On the other hand, these are the stellar spectrum, the orbital parameters, the initial trace gas profiles and the ionization rates.

The stellar spectrum is used to generate a pre-calculated table for the photolysis rates used by the neutral chemistry module (see section 3.1.2). In combination with the orbital parameters, which determine the stellar zenith angle, and the $O_2/O_3$ column above each level, the photolysis rates are calculated at the beginning of each chemical time step. In the case of tidally locked planets the stellar zenith angle is considered as constant throughout the model experiments.

The collision of the energetic particles with the surrounding atmospheric species can lead to dissociation, dissociative ionization, ionization, and excitation processes (Sinnhuber et al., 2012; Herbst et al., 2022). Hence, the starting point for the chemical calculations of the impact of energetic particle events are the initial trace gas profiles, which are here provided by DLR's climate model (1D-TERRA, see section 3.2.1).

ExoTIC uses these input profiles to calculate the time-dependent volume mixing ratios of the neutral species (Borthakur, 2025). Various input parameters can be used to control how often the neutral chemistry should be called up per hour. It is also possible to determine when, how long and at which levels the ion chemistry is calculated. This means that the ion chemistry module (see 3.1.3) is always called alternately with the neutral chemistry module. The ion chemistry exploits the wide range of reactions of the implemented charged species and computes the net effective production and loss rates of the neutral species (highlighted **bold** in Table 3.1) after reaching an equilibrium (Schleif, 2024; Borthakur, 2025). The production rates are then returned to neutral chemistry and added to the volume mixing ratio as chemical trends until the next iteration step of the ion chemistry begins. This iteration lasts until the ionization rates are greater than zero (Borthakur, 2025).

The species vary their concentration on different time scales, because the reaction rates between neutral and ionic reactions can differ by orders of magnitudes. This is why there is a distinction between long-lived and integrated species, which leads to separation of the neutral and ion chemistry module.

### 3.1.2 Neutral Chemistry Module

The neutral chemistry module of ExoTIC is based on the **S**ingle **L**ayer **I**sentropic **M**odel of **C**hemistry **a**nd **T**ransport (SLIMCAT) by Chipperfield (1999). The atmospheric chemistry is dominated by bimolecular and trimolecular and photodissociation reactions (Winkler, 2008). SLIMCAT originally consisted of 53 different atmospheric species (ExoTIC currently uses 63 species). In addition, the species that are important for sulfur chemistry and the photochemical reactions in which they are involved have been implemented in a recent masters thesis (Schleif, 2024). In total, ExoTIC comprises now 53 photolysis reactions (Schleif, 2024). Furthermore, the reactions important for the abiotic production of $N_2O$ were added during this work. Table 3.1 provides an overview of all the currently implemented neutral species.

**Table 3.1: Neutral species available in ExoTIC.** The table provides the neutral species currently used in the integration routine of ExoTIC and is a summary of previous works (Winkler, 2008; Sinnhuber et al., 2012; Borthakur, 2025). The highlighted species (orange) were added by Schleif (2024), and those in blue and/or **bold** are also used within the ExoTIC's ion-chemistry module.

| Long-lived Species | Integrated Species |
|---|---|
| $CH_4$, **CO**, **$CO_2$**, $CFCl_3$, $CF_2Cl_2$, $CH_3Cl$, $CHF_2Cl$, $C_2F_3Cl_3$, $CH_3CCl_3$, $CCl_4$, $CBrClF_2$, $CBrF_3$, $CH_3Br$, HF, $COF_2$, COFCl, $N_2$, **$H_2$** | Br, HOBr, HBr, $BrNO_3$, BrCl, BrO, $CH_3O_2$, $CH_3O$, $CH_3OOH$, **HCO, ClO**, $Cl_2O_2$, **Cl, O, $O_3$, NO, N, N($^4$S), $NO_2$, H, OH, O($^1$D), $HO_2$, $N_2O_5$, $HNO_3$, $HNO_2$, $ClNO_3$, HCl**, $HNO_4$, **HOCl**, OClO, $H_2O_2$, **$NO_3$**, $CH_2O$, **$H_2O$, $Cl_2$, $O_2$, $N_2O$**, SO, $SO_2$, S, $SO_3$, **$H_2SO_4$**, ClCO, $ClCO_3$ |

According to Winkler (2008), the variation of the concentration of the different species $C_i$ over time can be defined by a set of coupled differential equations given in 3.1.

$$\frac{d[C_i]}{dt} = \left( \sum_{jk,k\neq i} k_{jk}[C_j][C_k] + \sum_{k,k\neq i} J_k[C_k] \right) - \left( \sum_j k_{ij}[C_j][C_i] + J_i[C_i] \right) = P_i - L_i. \quad (3.1)$$

Here, $[C_{ijk}]$ are the concentrations (molecules/cm$^3$) of different involved species, changing the overall concentration of specie $C_i$. $k_{jk}$ is the reaction rate constant (cm$^3\cdot$ molecules$^{-1}\cdot$ s$^{-1}$) and $J_i$ is the photolysis rate constant (s$^{-1}$). For different species, this lead to a set of differential equations, which can be numerically integrated by various methods.

For the long-lived species, whose lifetime exceed the model timestep, SLIMCAT uses a simple forward-Euler approach (Chipperfield, 1999; Winkler, 2008) with a time step of 15

minutes, while for the other ones a semi implicit scheme (SIS) method is used (originally from Ramaroson, 1989). The following explanation of this integration scheme is based on Winkler (2008).

According to equation 3.1, the change in the concentration $C_i$ over time is a function of concentrations $C_{ijk}$. To numerically integrate the differential equations with specie C, 3.1 can be approximately written as

$$\frac{dC}{dt} \approx \frac{\Delta C}{\Delta t} = f(C(t)). \tag{3.2}$$

For the interval [t, t+Δt], one can use the trapezoidal rule and integrate equation 3.2. Thus the change in the concentration will be given by

$$\Delta C = C(t + \Delta t) - C(t) \approx \frac{\Delta t}{2} \cdot \left( f(C(t + \Delta t)) + f(C(t)) \right). \tag{3.3}$$

For small Δt, a first order taylor expansion $f(C(t + \Delta t)) \approx f(C(t)) + \mathbf{J}_f \cdot \frac{\Delta C}{\Delta t} \cdot \Delta t$ can be applied to the right hand side of equation 3.3, which leads to

$$\Delta C \approx \frac{\Delta t}{2} \cdot \left( 2 \cdot f(C(t)) + \mathbf{J_f} \cdot \Delta C \right), \tag{3.4}$$

where $\mathbf{J}_f$ is known as the Jacobian matrix of the function $\mathbf{f}$. If $\mathbf{f}$ is divided into two homogeneous functions consisting of the bimolecular ($f_{bim}$) and the photolysis ($f_{phot}$) contribution and both fulfill the condition $f(\lambda C(t)) = \lambda^k f(C(t))$, then it follows from Euler's theorem, that $f(C) = k^{-1}\mathbf{J_f} \cdot C$. Here, the index $k$ shows the degree of homogeneity. Using a degree of $k = 1$ for the photolysis part, $k = 2$ for the bimolecular reactions and $C(t) = C(t + \Delta t) - \Delta C$, equation 3.4 can be written as

$$\Delta C \approx \frac{\Delta t}{2} \cdot \left( \mathbf{J_{bim}} \cdot C(t + \Delta t) + 2 \cdot \mathbf{J_{phot}} \cdot C(t + \Delta t) - \mathbf{J_{phot}} \cdot \Delta C \right) \tag{3.5}$$

Rearranging the parts and neglecting $\Delta C \Delta t$, one can obtain the solution for

$$C(t + \Delta t) \approx \left( \mathbb{1} - \frac{\Delta t}{2} \cdot \mathbf{J_{bim}} - \Delta t \cdot \mathbf{J_{phot}} \right)^{-1} \cdot C(t), \tag{3.6}$$

which has the form $x = A^{-1}y$. The inverse of the matrix is calculated by Gaussian elimination. The SIS approach is very robust, and can therefore be used for atmospheres

with fast reactions like the thin atmospheres here, which have rapid changes of the concentrations due to photochemistry. Therefore, the time step has to be smaller (1 to 5 minutes), which makes the SIS in addition to the larger amount of integrated species rather time consuming. The efficiency can be increased by including an adaptive timestep, which is determined by the reaction velocity. Hence, for faster reactions, the timestep of the integration would be smaller, for slower reactions it would be bigger.

### 3.1.3 Ion Chemistry Module

The heart of ExoTIC is the ion chemistry module, which currently contains 108 charged (positive and negative) and the excited states of N, $N_2$ and O. As mentioned above, it is based on the ion chemistry module of the University of Bremen Ion Chemistry model (UBIC), which as a whole was developed by Winkler (2008). The main interest in this thesis is to study the impact of stellar particle events (SPE) on planetary atmospheres.

Therefore, the ion chemistry module uses prescribed ionization rates, provided by the AtRIS code (see section 3.2.2). The first step is to calculate the formation rates of the primary ions. This includes the dissociation, dissociative ionization and ionization of $N_2$, $O_2$ (Sinnhuber et al., 2012) and $CO_2$ (Herbst et al., 2024), the ionization of atomic oxygen (Sinnhuber et al., 2012), as well as the new implemented primary ionization of $H_2$, $H_2O$ and the excitation of $N_2$. R57–R61 recaps the reactions initiated by an energetic particle $\boldsymbol{x}^*$. For reasons of clarity, only the resulting ions/excited states are shown as products. The full reaction equations are listed in chapter 2.

$$N_2 + \boldsymbol{x}^* \longrightarrow ({N_2}^+, N^+ \text{ or } N^*) + \boldsymbol{x}^* + e^- \tag{R57}$$

$$O_2 + \boldsymbol{x}^* \longrightarrow ({O_2}^+, O^+ \text{ or } O) + \boldsymbol{x}^* + e^- \tag{R58}$$

$$H_2 + \boldsymbol{x}^* \longrightarrow ({H_2}^+, H^+) + \boldsymbol{x}^* + e^- \tag{R59}$$

$$CO_2 + \boldsymbol{x}^* \longrightarrow ({CO_2}^+, CO^+) + \boldsymbol{x}^* + e^- \tag{R60}$$

$$H_2O + \boldsymbol{x}^* \longrightarrow ({H_2O}^+, OH^+, {H_2}^+, H^+ \text{ or } O^+) + \boldsymbol{x}^* + e^- \tag{R61}$$

The corresponding ion formation rates P are based on equation 2.3 presented in section 2.3.1. For historical reasons, the total ionization cross-section is scaled to the total cross-section of $O_2$. This leads to the modified version of equation 2.3, given by

$$P(c^+) = \frac{\sigma_c^+ \cdot \frac{\sigma_{tot,c}}{\sigma_{tot,O_2}} \cdot [C] \cdot IPR}{\sum_i \frac{\sigma_{tot,i}}{\sigma_{tot,O_2}} \cdot [C_i]} = \frac{\sigma_c^+ \cdot \frac{\sigma_{tot,c}}{\sigma_{tot,O_2}} \cdot [C] \cdot IPR}{Q_{tot}}. \tag{3.7}$$

The total ionization cross-sections used in ExoTIC for calculating $Q_{tot}$ and finally P($c^+$) are $O_2$, $N_2$, O, (Kieffer and Dunn, 1966; Sinnhuber et al., 2012, values also used by Nieder et al., 2014 before) , $CO_2$ (based on Knudsen et al., 1995, already used in Herbst et al., 2024), $H_2O$ (Itikawa & Mason, 2005) and $H_2$ (Straub et al., 1996; Yoon et al., 2008). $\sigma_c^+$ is the cross-section of creating an ion $c^+$ and can therefore be interpreted as a branching ratio. If, for example, ions out of $N_2$ are formed, $\sigma(N^+) + \sigma(N_2^+)$ is equal to the total ionization cross-section $\sigma(N_2)$. Table 3.2 provides an overview of the resulting ion production rates for the different ions produced by primary ionization.

**Table 3.2: Ion production rates of primary ions and excited species.** The table provides the numbers used for calculating the ion production rates due to primary ionization and the calculation of the total produced charge. Things highlighted in blue were added during this thesis.

| Ion | Rate of Production[1] |
|---|---|
| $N^+$ | $0.24 \cdot 0.8978 \cdot [N_2] \cdot IPR/Q_{tot}$ |
| $N_2^+$ | $0.76 \cdot 0.8978 \cdot [N_2] \cdot IPR/Q_{tot}$ |
| $O^+$ | $(0.33 \cdot [O_2] + 0.56 \cdot [O] + 0.89 \cdot 1.2 \cdot 0.13 \cdot [CO_2] + 0.0285 \cdot 0.68 \cdot [H_2O]) \cdot IPR/Q_{tot}$ |
| $O_2^+$ | $0.67 \cdot [O_2] \cdot IPR/Q_{tot}$ |
| $H_2^+$ | $(0.0003 \cdot 0.68 \cdot [H_2O] + 0.94 \cdot 0.21 \cdot [H_2]) \cdot IPR/Q_{tot}$ |
| $H^+$ | $(0.15 \cdot 0.68 \cdot [H_2O] + 0.06 \cdot 0.21 \cdot [H_2]) \cdot IPR/Q_{tot}$ |
| $CO_2^+$ | $0.75 \cdot 0.89 \cdot 1.2 \cdot [CO_2] \cdot IPR/Q_{tot}$ |
| $CO^+$ | $0.12 \cdot 0.89 \cdot 1.2 \cdot [CO_2] \cdot IPR/Q_{tot}$ |
| $H_2O^+$ | $0.61 \cdot 0.68 \cdot [H_2O] \cdot IPR/Q_{tot}$ |
| $OH^+$ | $0.20 \cdot 0.68 \cdot [H_2O] \cdot IPR/Q_{tot}$ |
| $N_2(A^3\Sigma_u^+)$ | $0.35 \cdot IPR^2$ |

*Continued on the next page*

| Total produced charge |
|---|
| $Q_{tot} = 0.8978 \cdot [N_2] + 1.0 \cdot [O_2] + 0.56 \cdot [O] +$ $0.89 \cdot 1.2 \cdot [CO_2] + 0.68 \cdot [H_2O] + 0.21 \cdot [H_2]$ |

[1] $\sigma_c^+$ for the products of $H_2O$ (Itikawa & Mason, 2005) and for $H_2$ (Straub et al., 1996; Yoon et al., 2008).
[2] The production rate of $N_2(A^3\Sigma_u^+)$ is based on Zipf and Prasad (1980).

The interaction of the primary produced ions with the surrounding atmospheric constituents enable further reactions producing ions through neutral, neutral-ion and ion-ion gas-phase reactions, as well as through photolysis, photo-electron attachment and detachment reactions (Sinnhuber et al., 2012; Borthakur, 2025). An overview of the currently included ions and ion clusters is given in Table 3.3.

**Table 3.3: Negative and positive ions available in ExoTIC.** The table provides the currently in ExoTIC available positive and negative ions as well as ion clusters and short-lived neutrals. It includes the work of Winkler (2008) and Sinnhuber et al. (2012) and is adapted from Borthakur (2025). The highlighted ions (blue) were added during this work.

| Positive Ions | Negative Ions |
|---|---|
| $N^+$, $N_2^+$, $NO^+$, $NO_2^+$, $O(^4S)^+$, $O(^2D)^+$, $O(^2P)^+$, | $O^-$, $O_2^-$, $O_3^-$, $O_4^-$, $CO_3^-$, $CO_4^-$, $CH_3^-$ |
| $O_2^+$, $O_4^+$, $O_5^+$, $H^+$, $CO^+$, $CO_2^+$, $HCO^+$, | $CO_3^-$ $(H_2O)$, $CO_3^-$ $(H_2O)_2$, $HCO_3^-$, |
| $O_2^+(H_2O)$, $H_2O^+$, $H^+(H_2O)$, $H^+(H_2O)(OH)$, | $NO_2^-$, $NO_2^-$ $(H_2O)$, $NO_2^-$ $(H_2O)_2$, |
| $H^+(H_2O)_2$, $H^+(H_2O)_3$, $H^+(H_2O)_4$, | $OH^-$, $Cl^-$, $Cl_2^-$, $Cl_3^-$, $Cl^-$ $(HCl)$, |
| $H^+(H_2O)_5$, $H^+(H_2O)_6$, $H^+(H_2O)_7$, | $Cl^-$ $(H_2O)$, $Cl^-$ $(CO_2)$, $Cl^-$ $(HO_2)$, |
| $NO^+(H_2O)$, $NO^+(H_2O)_2$, $NO^+(H_2O)_3$, | $O^-$ $(H_2O)$, $O_2^-$ $(H_2O)$, $O_2^-$ $(H_2O)_2$, |
| $NO^+(CO_2)$, $NO^+N_2$, $NO_2^+(H_2O)$, | $O_3^-$ $(H_2O)$, $O_3^-$ $(H_2O)_2$, $NO_3^-$ $(H_2O)$, |
| $NO_2^+(H_2O)_2$, $NO^+(H_2O)(CO_2)$, | $NO_3^-$ $(H_2O)_2$, $NO_3^-$ $(HCl)$, |
| $NO^+(H_2O)_2(CO_2)$, $NO^+(H_2O)N_2$, | $NO_3^-$ $(HNO_3)$, $NO_3^-$ $(HNO_3)_2$, |
| $NO^+(H_2O)_2N_2$, $H^+(H_2O)(CO_2)$, | $NO_3^-$ $(HNO_3)_3$, $NO_3^-$ $(HNO_3)_4$, |
| $H^+(H_2O)_2(CO_2)$, $H^+(H_2O)N_2$, | $OH^-$ $(H_2O)_2$, $ClO^-$, $NO_3^-$, $HSO_4^-$, |
| $H^+(H_2O)_2N_2$, $H^+(CH_3CN)$, | $HSO_4^-$ $(H_2SO_4)$, $HSO_4^-$ $(H_2SO_4)_2$ |
| $H^+(CH_3CN)(H_2O)$, $H^+(CH_3CN)(H_2O)_2$, | $HSO_4^-$ $(H_2SO_4)(H_2O)$, |
| $H^+(CH_3CN)(H_2O)_3$, $H^+(CH_3CN)(H_2O)_4$, | $HSO_4^-$ $(HNO_3)$, $HSO_4^-$ $(HNO_3)_2$, |

*Continued on the next page*

| Positive Ions | Negative Ions |
|---|---|
| $H^+(CH_3CN)(H_2O)_5$, $H^+(CH_3CN)(H_2O)_6$, $H^+(CH_3CN)_2$, $H^+(CH_3CN)_2(H_2O)$, $H^+(CH_3CN)_2(H_2O)_2$, $H^+(CH_3CN)_2(H_2O)_3$, $H^+(CH_3CN)_2(H_2O)_4$, $H^+(CH_3CN)_3$, $H^+(CH_3CN)_3(H_2O)$, $H^+(CH_3CN)_3(H_2O)_2$, ***$H_2^+$***, ***$OH^+$*** | $HSO_4^-$ $(HNO_3)(H_2O)$, $HSO_4^-$ $(HNO_3)_2(H_2O)$, $HSO_4^-$ $(H_2SO_4)(HNO_3)$, $HSO_4^-$ $(H_2SO_4)(HNO_3)(H_2O)$ |
| | Short-lived/Excited Species |
| | $N(^2D)$, ***$N_2(A^3\Sigma_u^+)$***, $ClONO_2$, $ClNO_2$ |

During this work, I added two new ions ($H_2^+$, $OH^+$) and the excited state of molecular nitrogen ($N_2(A^3\Sigma_u^+)$) to the ion chemistry module (colored in Table 3.3). Including the ionization of $H_2O$ and $H_2$ is important to better understand the impact of energetic particles on water- and/or hydrogen-rich atmospheres. The former can be caused by the increase in surface temperature due to impacting planetesimals and subsequent degassing of $H_2O$ (Matsui & Abe, 1986), whereas the latter are remnants of the early accretion process within the stellar nebula (Lammer, 2012). The created ions interact with the surrounding atmospheric constituents through various reactions with neutrals or other charged particles.

In ExoTIC, two different types of reactions are included, temperature-dependent and temperature-independent reactions. For $H_2^+$ and $OH^+$, these reactions can be found in Tables 3.4 and 3.5 with the corresponding rate coefficients and, if applicable, the branching ratios. A detailed description of the other reactions implemented can be found in Sinnhuber et al. (2012).

**Table 3.4: Overview of temperature dependent reactions for $H_2^+$ and $OH^+$ ions.** This table shows the recently added temperature dependent reactions for species involved in the $H_2$ and $H_2O$ ionization. It includes dissociative, recombination and charge exchange reactions.

| Reaction Equation | Rate coefficient ($cm^3s^{-1}$) | Reference |
|---|---|---|
| $OH^+ + OH \longrightarrow H_2O^+ + O$ | $7.0 \times 10^{-10} \cdot (T/300)^{-0.5}$ | Millar et al. (2024) |
| $OH^+ + e^- \longrightarrow O + H$ | $3.75 \times 10^{-8} \cdot (T/300)^{-0.5}$ | Millar et al. (2024) |
| $CO^+ + OH \longrightarrow OH^+ + CO$ | $3.1 \times 10^{-10} \cdot (T/300)^{-0.5}$ | Millar et al. (2024) |
| $N_2{}^+ + OH \longrightarrow OH^+ + N_2$ | $6.3 \times 10^{-10} \cdot (T/300)^{-0.5}$ | Millar et al. (2024) |
| $H^+ + OH \longrightarrow OH^+ + H$ | $2.1 \times 10^{-9} \cdot (T/300)^{-0.5}$ | Millar et al. (2024) |
| $O^+ + OH \longrightarrow OH^+ + O$ | $3.6 \times 10^{-10} \cdot (T/300)^{-0.5}$ | Millar et al. (2024) |
| $O^+ + HCO \longrightarrow OH^+ + CO$ | $4.3 \times 10^{-10} \cdot (T/300)^{-0.5}$ | Millar et al. (2024) |
| $H_2{}^+ + H_2O \longrightarrow H_2O^+ + H_2$ | $3.9 \times 10^{-9} \cdot (T/300)^{-0.5}$ | Millar et al. (2024) |
| $H_2{}^+ + OH \longrightarrow OH^+ + H_2$ | $7.6 \times 10^{-10} \cdot (T/300)^{-0.5}$ | Millar et al. (2024) |
| $H_2{}^+ + e^- \longrightarrow H + H$ | $1.6 \times 10^{-8} \cdot (T/300)^{-0.43}$ | Millar et al. (2024) |
| $H_2{}^+ + OH \longrightarrow H_2O^+ + H$ | $7.6 \times 10^{-10} \cdot (T/300)^{-0.5}$ | Millar et al. (2024) |
| $H_2{}^+ + HCO \longrightarrow HCO^+ + H_2$ | $1.0 \times 10^{-9} \cdot (T/300)^{-0.5}$ | Millar et al. (2024) |
| $H^+ + HCO \longrightarrow H_2{}^+ + CO$ | $9.4 \times 10^{-10} \cdot (T/300)^{-0.5}$ | Millar et al. (2024) |

**Table 3.5: Overview of temperature independent reactions containing $H_2^+$ and $OH^+$ ions.** This table shows the recently added temperature independent reactions for species involved in the $H_2$ and $H_2O$ ionization. It includes dissociative and charge exchange reactions.

| Reaction Equation | | | Rate coefficient ($cm^3s^{-1}$) | Reference |
|---|---|---|---|---|
| $OH^+ + H_2$ | $\longrightarrow$ | $H_2O^+ + H$ | $1.01 \times 10^{-9}$ | J. Jones et al. (1981) |
| $OH^+ + H_2O$ | $\longrightarrow$ | $H_2O^+ + OH$ | $2.89 \times 10^{-9} \cdot 0.55$ [a] | Huntress Jr (1977) |
| $OH^+ + O_2$ | $\longrightarrow$ | $O_2{}^+ + OH$ | $5.9 \times 10^{-10}$ | J. Jones et al. (1981) |
| $OH^+ + NO$ | $\longrightarrow$ | $NO^+ + OH$ | $1.3 \times 10^{-9} \cdot 0.95$ [a] | Karpas and Huntress (1978) |
| $OH^+ + CO$ | $\longrightarrow$ | $HCO^+ + O$ | $1.05 \times 10^{-9}$ | Karpas and Huntress (1978) |
| $O^+ + H_2$ | $\longrightarrow$ | $OH^+ + H$ | $1.58 \times 10^{-9}$ | Huntress Jr (1977) |
| $OH^+ + HCO$ | $\longrightarrow$ | $CO + H_2O^+$ | $1.05 \times 10^{-9}$ | Millar et al. (2024) |
| $H_2{}^+ + O_2$ | $\longrightarrow$ | $O_2{}^+ + H_2$ | $8.0 \times 10^{-10}$ | Millar et al. (2024) |
| $H_2{}^+ + CO$ | $\longrightarrow$ | $CO^+ + H_2$ | $6.44 \times 10^{-10}$ | Millar et al. (2024) |
| $H_2{}^+ + H$ | $\longrightarrow$ | $H^+ + H_2$ | $6.4 \times 10^{-10}$ | Millar et al. (2024) |
| $H_2{}^+ + CO$ | $\longrightarrow$ | $HCO^+ + H$ | $2.16 \times 10^{-9}$ | Millar et al. (2024) |
| $H_2{}^+ + NO$ | $\longrightarrow$ | $NO^+ + H_2$ | $1.10 \times 10^{-9}$ | Millar et al. (2024) |
| $H_2{}^+ + O$ | $\longrightarrow$ | $OH^+ + H$ | $1.5 \times 10^{-9}$ | Millar et al. (2024) |

[a] Branching ratios are from given references

As already mentioned in chapter 2, the excited state of the nitrogen molecule is important, because it plays a key role in the abiotic production of nitrous oxide ($N_2O$) during energetic

particle events via the $N_2(A^3\Sigma_u^+)$, especially in the upper atmospheric layers (Kelly et al., 2018). Hence, these reactions were also included in ExoTIC. Table 3.6 summarizes the newly implemented reactions that can form $N_2O$ or reduce $N_2(A^3\Sigma_u^+)$ by de-excitation. The Table also includes the corresponding reaction rates.

**Table 3.6: Abiotic $N_2O$ production by the excited state of molecular nitrogen ($N_2(A^3\Sigma_u^+)$).** This table shows the different reactions, also $N_2O$ production, recently added to the ExoTIC chemistry and ion chemistry modules. Additionally, the reactions for de-excitation of $N_2(A^3\Sigma_u^+)$ are shown as well.

| Reaction Equation | Rate coefficient ($cm^3s^{-1}$) | Reference |
|---|---|---|
| $N + NO_2 \longrightarrow N_2O + O$ | $5.8 \times 10^{-12} \cdot exp(1/T)^{220}$ | Wennberg et al. (1994) |
| $N_2(A^3\Sigma_u^+) + O_2 \longrightarrow N_2O + O$ | $1.9 \times 10^{-12} \cdot 0.005$ [a] | Zipf and Prasad (1980) |
| $N_2(A^3\Sigma_u^+) + O_2 \longrightarrow N_2 + 2\,O$ | $1.9 \times 10^{-12} \cdot 0.995$ [a] | Zipf and Prasad (1980) |
| $N_2(A^3\Sigma_u^+) + O \longrightarrow N_2 + O$ | $2.5 \times 10^{-11}$ | Herron (1999) |

[a] Branching ratios from Kelly et al. (2018).

After calculating the formation rates, the concentrations of the ions have to be determined. Thus, equation 3.1 can be modified by neglecting photolysis and adding the ion formation to the production term. This leads to

$$\frac{d[C_i]}{dt} = \underbrace{P(C_i) + \sum_{jk} k_{jk}[C_j][C_k]}_{\text{Production Term}} - \underbrace{[C_i] \cdot \sum_{j} k_{jk}[C_j]}_{\text{Loss Term}}. \tag{3.8}$$

Here, $[C_i]$ also includes the ion species. Assuming equilibrium conditions $d[C_i]/dt = 0$, the above equation 3.8 simplifies to

$$[C_i] = \frac{Production}{Loss/[C_i]}. \tag{3.9}$$

Since $[C_i]$, $[C_j]$ and $[C_k]$ are dependent on each other, this procedure has to be iterated until it converges. As the ions can form neutral species, for example due to recombination reactions, the production rate of a neutral specie $C_i$ is calculated by

$$Prod(C) = (Production - Loss)/IPR. \tag{3.10}$$

They are used as tendencies for the neutral chemistry module (Borthakur, 2025). According to this method, the production rates from the positive and negative ion chemistry are calculated separately.

### 3.1.4 Technical Developments

Apart from the scientific additions to ExoTIC (mentioned above), the ion chemistry with its many reactions is computationally very expensive. For each vertical level, the model has to solve the chemical equations and reach the ion-chemical equilibrium. The original code (Winkler et al., 2009) does this in a serial way, resulting in long runtimes of several days for a multi-hour energetic particle event. It would be better to run the model on an HPC cluster, which offers the advantage of parallelizing certain processes with MPI. During this work, ExoTIC was moved to bwUniCluster (2.0/3.0) to reduce the model runtime of the ionchemical processes.

#### Message Passing Interface (MPI)

Like many other climate chemistry models, ExoTIC is written in Fortran, a fast programming language to implement mathematical, physical or chemical equations. HPC Clusters such as bwUniCluster (2.0/3.0) are designed in a multi-node structure. MPI offers the user the possibility to use this structure for computationally expensive processes[1]. MPI can be integrated into the Fortran files using the command *use mpi*. The actual files are then compiled with *mpif90*, a wrapper for *gfortran*, which ensures that all libraries are loaded correctly. As already mentioned, the most computationally intensive part of the code is the ion chemistry, in particular the iteration until the ionic species have been brought into equilibrium.

[1] https://www.mpi-forum.org/docs/mpi-5.0/mpi50-report.pdf

```
call MPI_Barrier(MPI_COMM_WORLD, ierror)
IF (size_Of_Cluster > 1) THEN
    IF (size_Of_Cluster > (IONEND-IONSTART)+1) THEN
        write(*,*) '-------------------------------------'
        write(*,*) 'MPI_ERROR: Number of tasks have to be lower than (IONEND-IONSTART)+1
             or equal (IONEND-IONSTART)+1'
        call MPI_Abort(MPI_COMM_WORLD,1,ierror)
    END IF

    ! Partition, i.e. get local number of columns
    nloc = ((IONEND-IONSTART)+1) / size_Of_Cluster
    IF (mod((IONEND-IONSTART)+1,size_Of_Cluster) > process_Rank) THEN
        nloc = nloc + 1
        !write(*,*) 'nloc:', nloc
    END IF

    IF (process_Rank == 0) THEN
        istart = IONSTART
        iend   = nloc + IONSTART - 1
        call MPI_SEND(iend,1,MPI_INT,process_Rank+1,0,MPI_COMM_WORLD,ierror)
        !write(*,*) 'istart:', istart, 'iend:',iend,'myid:',myid,'nloc:',nloc
    ELSE
        call mpi_RECV(iend,1,MPI_INT,process_Rank-1,0,MPI_COMM_WORLD,MPI_STATUS_IGNORE,
            ierror)
        istart = iend + 1
        iend   = istart + nloc - 1
        !write(*,*) 'istart:',istart,'iend:', iend, 'myid:', myid,'nloc:',nloc
        IF (process_Rank < size_Of_Cluster-1) THEN
            call MPI_SEND(iend,1,MPI_INT,process_Rank+1,0,MPI_COMM_WORLD,ierror)
        END IF
    END IF
    !write(*,*) 'istart:',istart,'iend:', iend, 'process_Rank:', process_Rank, 'nloc:',
        nloc
ELSE
    ...
    istart = IONSTART
    iend   = IONEND !i - 1
    nloc   = (IONEND-IONSTART) + 1
    write(*,*) 'istart: ', istart, 'iend: ', iend, 'nloc: ', nloc
END IF
```

**Code 3.1: MPI splitting of the ion chemistry into multiple tasks.** This snippet provides the code used to divide the ion chemistry into several tasks, depending on the specified cluster size. Thus, one task for each level will be created.

The idea is therefore to split the vertical levels into several tasks. Their maximum possible number results from the number of nodes multiplied by the number of tasks per node. The vertical levels are independent of each other, so it is possible to use one task for each level to run the ion chemistry. This is shown in the code snippet 3.1. The code calculates how many levels one task has to do depending on the overall number of tasks. The variables *istart* and *iend* define the new start and end point of the do loop in which the ion chemistry routines are called for this new level. Once this loop is complete, the resulting production rates of every task are stored in an array, whose size depends on the number of used tasks. For example, if 50 tasks are used, this array consists of two vertical levels for which all the production rates of the species are calculated. In the end, all arrays of each task are merged back into an array over the entire 100 vertical levels, which is shown in the code snippet 3.2.

```
! gather the arrays of each subprocess within the ionization Range into the root process
DO I=1,NUMION2
    call MPI_Allgather(loc_IONSneg(:,I),nloc*2,MPI_REAL,IONSneg(IONSTART:,I),nloc*2,
        MPI_REAL,MPI_COMM_WORLD,ierror)
END DO
call MPI_Barrier(MPI_COMM_WORLD, ierror)
DO I=1,NUMION2
    call MPI_Allgather(loc_prodRates_neg(:,I),nloc*2,MPI_REAL,prodRates_neg(IONSTART:,I)
        ,nloc*2,MPI_REAL, &
         MPI_COMM_WORLD,ierror)
END DO
call MPI_Barrier(MPI_COMM_WORLD, ierror)
DO I=1,NUMION
    call MPI_Allgather(loc_IONS(:,I),nloc*2,MPI_REAL,IONS(IONSTART:,I),nloc*2,MPI_REAL,
        MPI_COMM_WORLD,ierror)
END DO
call MPI_Barrier(MPI_COMM_WORLD, ierror)
DO I=1,NUMION
    call MPI_Allgather(loc_prodRates_pos(:,I),nloc*2,MPI_REAL,prodRates_pos(IONSTART:,I)
        ,nloc*2,MPI_REAL, &
         MPI_COMM_WORLD,ierror)
END DO
call MPI_Barrier(MPI_COMM_WORLD, ierror)
```

**Code 3.2: Merging process within MPI.** This snippet provides the code used to merge the results back into one array.

The runtime of the ion chemistry loop depends on the ionization rates and is different for each of the levels. To ensure that the merge order is done correctly, all tasks have to be

at the same position before continuing with the next part of the code. In MPI this can be done by using the command *call MPI_Barrier(MPI_COMM_WORLD, ierror)*, which waits for all tasks reaching that position in the code. This reduces the runtime of the model to several hours instead of days.

#### Network Common Data Format (netCDF) Output

In climate science, the most common output format for post-processing is netCDF. It provides an efficient structure for storing different variables as multidimensional arrays. Thus, it is easier to structure and access the gridded data and reduce the storage space compared to ASCII-files. These advantages are enough to use netCDF also as a common format for ExoTIC, since ASCII-files were used as input/output at the beginning of the thesis. Therefore, several new modules were added to the source code, which includes netCDF routines for the output of the volume mixing ratios, production rates and photolysis rates. To use there the whole functions of Fortran netCDf modules, the netCDf libraries (lnetcdff) have to be added as additional compiler flags. The snippet 3.3 shows a part of the routine to create the netCDF files, where the built-in functions of the netCDF libraries are used.

```
subroutine create_netcdf_file (NSPEC, NLVLS, ZLEV, PLEV, SPEC_TYPE, id_event,
    mult_events)
    use netcdf
    implicit none

    [...] ! Definition of the arrays, the variable names and the file paths

    ! Create the file.
    call check( nf90_create(Out_file_name, nf90_clobber, ncid) )
    ! Define the dimensions. The record dimension is defined to have
    ! unlimited length - it can grow as needed. In this example it is
    ! the time dimension.
    call check( nf90_def_dim(ncid, LVL_NAME, NLVLS, lvl_dimid) )
    call check( nf90_def_dim(ncid, LAT_NAME, NLATS, lat_dimid) )
    call check( nf90_def_dim(ncid, LON_NAME, NLONS, lon_dimid) )
    call check( nf90_def_dim(ncid, REC_NAME, NF90_UNLIMITED,rec_dimid) )
    ! Define the coordinate variables.
    [...]
    call check( nf90_def_var(ncid, LAT_NAME, NF90_DOUBLE, lat_dimid,lat_varid) )
    call check( nf90_def_var(ncid, LON_NAME, NF90_DOUBLE, lon_dimid,lon_varid) )
    call check( nf90_def_var(ncid, LVL_NAME, NF90_DOUBLE, lvl_dimid,lvl_varid) )
```

```
        [...] ! Assign attributes to the variables and coordinates as well as global
            attributes

        ! The dimids array is used to pass the dimids of the dimensions of
        ! the netCDF variables. Both of the netCDF variables we are creating
        ! share the same four dimensions. In Fortran, the unlimited
        ! dimension must come last on the list of dimids.
        dimids = (/ lon_dimid, lat_dimid, lvl_dimid, rec_dimid /)
        ! Define the netCDF variable for the stellar zenith angle and eday
        call check( nf90_def_var(ncid, 'eTime', NF90_INT, rec_dimid, eTime_id) )
        call check( nf90_def_var(ncid, 'P', NF90_DOUBLE, lvl_dimid, pl_id) )
        call check( nf90_def_var(ncid, 'T', NF90_DOUBLE, dimids, temp_id) )
        call check( nf90_def_var(ncid, 'Density', NF90_DOUBLE, dimids, den_id) )

        ! Define the netCDF variables for the different data output sets.
        if ( SPEC_TYPE == 'vmr' ) then
            call check( nf90_def_var(ncid, 'sza', NF90_DOUBLE, dimids, sza_id) )
            do i = 1, NSPEC
                call check( nf90_def_var(ncid, VAR_NAME(i), NF90_DOUBLE,dimids, array_id(i))
                     )
            end do
        else if ( SPEC_TYPE == 'ions_pos' ) then
            do i = 1, NSPEC
                call check( nf90_def_var(ncid, VAR_NAME_IONS_POS(i),NF90_DOUBLE, dimids,
                    array_id(i)) )
            end do
        else if ( SPEC_TYPE == 'ions_neg' ) then
            do i = 1, NSPEC
                call check( nf90_def_var(ncid, VAR_NAME_IONS_NEG(i),NF90_DOUBLE, dimids,
                    array_id(i)) )
            end do
        else if ( SPEC_TYPE == 'prodRates_pos' .or.SPEC_TYPE == 'prodRates_neg' ) then
            do i = 1, NSPEC
                call check( nf90_def_var(ncid, VAR_NAME_PRODRATES(i),NF90_DOUBLE, dimids,
                    array_id(i)) )
            end do
        else if ( SPEC_TYPE == 'photo_rates' ) then
            call check( nf90_def_var(ncid, 'sza', NF90_DOUBLE, dimids, sza_id) )
            do i = 1, array_count
                write(*,*) 'trim(selected_arrays(i)%name) (in define variables): ', trim(
                    selected_arrays(i)%name)
                call check( nf90_def_var(ncid, trim(selected_arrays(i)%name), NF90_DOUBLE,
                    dimids, array_id(i)) )
            end do
!           write(*,*) 'Spec_type in define variables: ', SPEC_TYPE
```

```
      end if
      [...] ! Assign attributes to the netCDF sza, eTime and specie variable
      ! End define mode.
      call check( nf90_enddef(ncid) )

      ! Write the coordinate variable data. This will put the latitudes
      ! and longitudes of our data grid into the netCDF file.
      call check( nf90_put_var(ncid, lat_varid, lats) )
      call check( nf90_put_var(ncid, lon_varid, lons) )
      call check( nf90_put_var(ncid, lvl_varid, zlev) )
      ! These settings tell netcdf to write one timestep of data. (The
      ! setting of start(4) inside the loop below tells netCDF which
      ! timestep to write.)
      count = (/ NLONS, NLATS, NLVLS, 1 /)
      start = (/ 1, 1, 1, 1 /)
      ! Write the pretend data. This will write our surface pressure and
      ! surface temperature data. The arrays only hold one timestep worth
      ! of data. We will just rewrite the same data for each timestep. In
      ! a real :: application, the data would change between timesteps.
      start(4) = 1
      call check( nf90_put_var(ncid, temp_id, temp_out, start = start,count = count) )
      call check( nf90_put_var(ncid, den_id, den_out, start = start,count = count) )
      call check( nf90_put_var(ncid, sza_id, sza_out, start = start,count = count) )
      call check( nf90_put_var(ncid, eTime_id, eTime) )
      call check( nf90_put_var(ncid, pl_id, pl_out) )

      [...] ! Put in the values for the different variables.

      ! Close the file. This causes netCDF to flush all buffers and make
      ! sure your data are really written to disk.
      call check( nf90_close(ncid) )
      [...]
  end subroutine create_netcdf_file
```

**Code 3.3: Creation of a netCDF file.** This snippet provides the code used to create a netCDF file for the different outputs of ExoTIC. The source code has been shortened for better explanation as an example.

After creating the netCDF files with all used variables, the output has to be written after each specific time step, defined in the initialization file. Therefore, a similar subroutine is applied to append the new calculated values to the existing netCDF files. This is repeated until the model reaches the end.

With the newly implemented netCDF and MPI routines, it is now possible to run multiple energetic particle events in a row, setting the corresponding variable in the initialization

file to *'.true.'*. This forces ExoTIC to create a new netCDF file after each particle event. For bigger events with a longer runtime, ExoTIC can then be restarted with the last output file via the netCDF read-in routine. It is based on the same principle as the file creation process, but uses slightly different commands from the netCDF library. This is also a safety feature if the model crashes or reaches the time limit of the HPC-Cluster for one job.

## 3.2 Description of the INCREASE Workflow

ExoTIC is part of a bigger framework, called INCREASE. The abbreviation stands for **IN**fluence of **C**osmic **R**ays on **E**xoplanetary **A**tmo**S**pher**E**s. It consists of four different models, the atmospheric climate chemistry model 1D-TERRA (DLR-Berlin), the ion chemistry model ExoTIC (KIT), the **At**mospheric **R**adiation **I**nteraction **S**imulator (AtRIS, CAU) and the **G**eneric **A**tmospheric **R**adiation **L**ine-by-line **I**nfra-red **C**ode (GARLIC, DLR) (Herbst et al., 2022; Herbst et al., 2019a).

Since 1D-TERRA does not include an ion chemistry scheme, ExoTIC has to take over this part of the model chain. Figure 3.1 shows the current INCREASE workflow of the different models involved. The chemistry-climate model 1D-TERRA (green box) provides the vertical atmospheric composition, the pressure and temperature profile, and feeds it to AtRIS (magenta box) and ExoTIC (blue box). AtRIS computes the ionization rates with the respective atmosphere and provides them to ExoTIC. Together with the stellar spectrum and the atmospheric profiles, it calculates the ionchemical impact and the corresponding production rates, which are fed back to 1D-TERRA. The chemical composition of the atmosphere after the ion-chemistry is used as input to calculate transmission spectra with GARLIC (red arrow in Fig. 3.1, and light green box). Compared to Herbst et al. (2019a), where the entire workflow is iterated until the results converge, this is not done in the context of this thesis due to personnel fluctuations at DLR. In the following subsections, the other models besides ExoTIC (section 3.1) will be described in more detail.

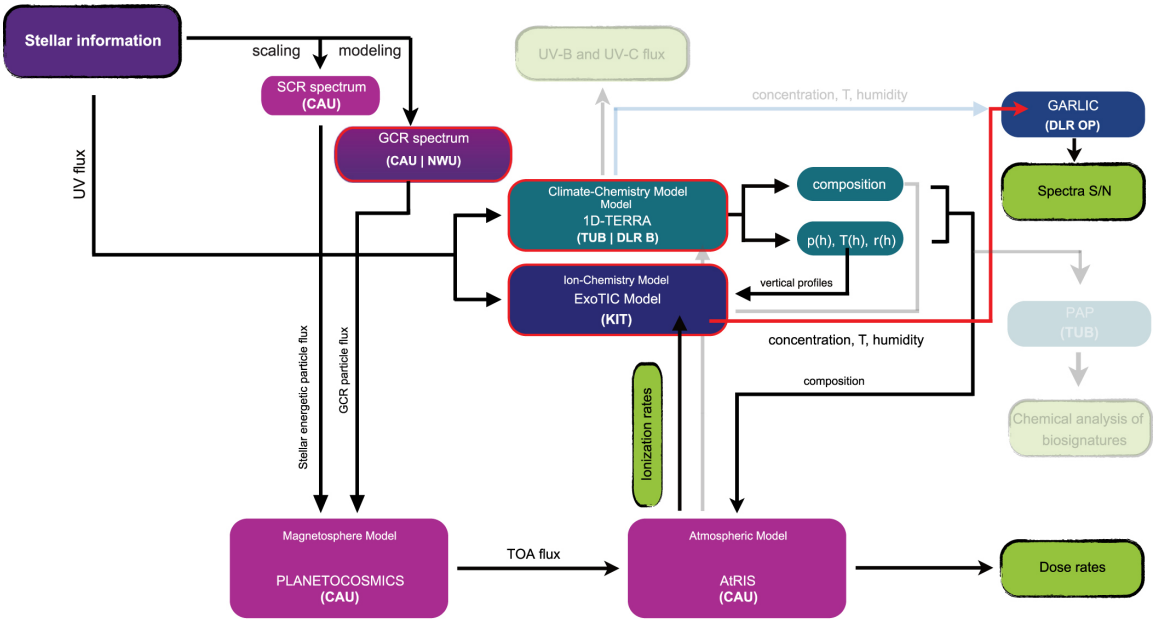


**Figure 3.1: Models and workflow of the INCREASE project.** This figure provides the interplay between the different models used in the INCREASE project. The magenta boxes show the part used at the University of Kiel (CAU), which provide the partner with ionization rates. The dark green boxes highlight the part used at DLR Berlin, calculating the atmospheric composition. The blue box represent work done at KIT, which compute the impact of ion chemistry on the atmospheric composition. Lastly, the light green boxes show the point, where spectra or dose rates are obtained. Compared to the full model suite (Herbst et al., 2019a), the red outlines indicate changes made since Herbst et al. (2019a) and the transparent boxes show unused models. The figure is from Herbst et al. (2024), licensed under CC BY 4.0. No changes were made.

### 3.2.1 1D-TERRA

1D-TERRA is a global-mean, stationary, cloud-free coupled convective-climate-photochemical column model. The model extends from the surface to ~100 km for modern Earth with 100 vertical grid cells. 1D-TERRA features two main modules: The climate module with the radiative transfer scheme REDFOX (Scheucher et al., 2020, and references therein) and the chemistry module including the chemistry / photochemistry scheme BLACKWOLF (Wunderlich et al., 2020). REDFOX computes radiative heating and cooling rates from the radiative transfer equation for discrete levels. It uses the stellar spectrum, initial temperature/pressure profiles and an initial atmospheric composition as inputs.

According to Scheucher et al. (2020), the calculations of the cross sections are based on the correlated-k approach to save computational resources, where the wavelengths are binned into larger spectral bands (128). The used spectrum ranges from $10^5$ cm$^{-1}$ to 0

$cm^{-1}$ (100 nm – ∞) and includes 20 different absorbers (HITRAN 2016)[2] in the infrared and 81 in the visible / UV spectral range. The pressure and temperature range extends from $10^3$ bar - $10^{-2}$ Pa and from 100 - 1000 K. REDFOX also considers Rayleigh scattering and collision-induced absorption (CIA). With all these parameters and the source function (blackbody emission based on Planck's law), the radiative transfer is solved with the two-stream approximation (Meador & Weaver, 1980). This results in the gradient $\frac{dF(z)}{dp(z)}$, which is then used to calculate the temperature profile by equation 3.11, where $c_p$ is the heat capacity and $g(z)$ the gravitational acceleration for each level.

$$\frac{dT(z)}{dt} = \frac{-g(z)}{c_p(T,z)} \cdot \frac{dF(z)}{dp(z)} \tag{3.11}$$

The chemistry module consisting of BLACKWOLF (Wunderlich et al., 2020) includes 1127 reactions for 128 different species. These are divided into termolecular, bimolecular, photolysis and thermodissociation (unimolecular) reactions. The photolysis regime consists of 81 absorbers and uses spectral data between 100 and 800 nm, which is binned to 133 bands. More information about the included reactions can be found in Wunderlich et al. (2020) and references therein. Vertical mixing is added via eddy diffusion.

With these reactions and parameters, BLACKWOLF solves the chemical continuity equation 3.12

$$\frac{dn}{dt} = \frac{\partial}{\partial z}\left(K \cdot \frac{\partial}{\partial z}\right) + P - nL, \tag{3.12}$$

with the eddy diffusion coefficient K, the production term P and the loss term L (Wunderlich et al., 2020). An overview of 1D-TERRA and the interaction between the two modules is shown in Fig. 3.2. The climate module runs until it converges and feeds the temperature, pressure and water profile to the chemistry to compute the atmospheric composition (Grenfell et al., 2012). Since stellar energetic particle events are short-lived, their atmospheric impact is masked due to mixing into an equilibrium state.

[2] HITRAN 2016 based on Gordon et al. (2017)

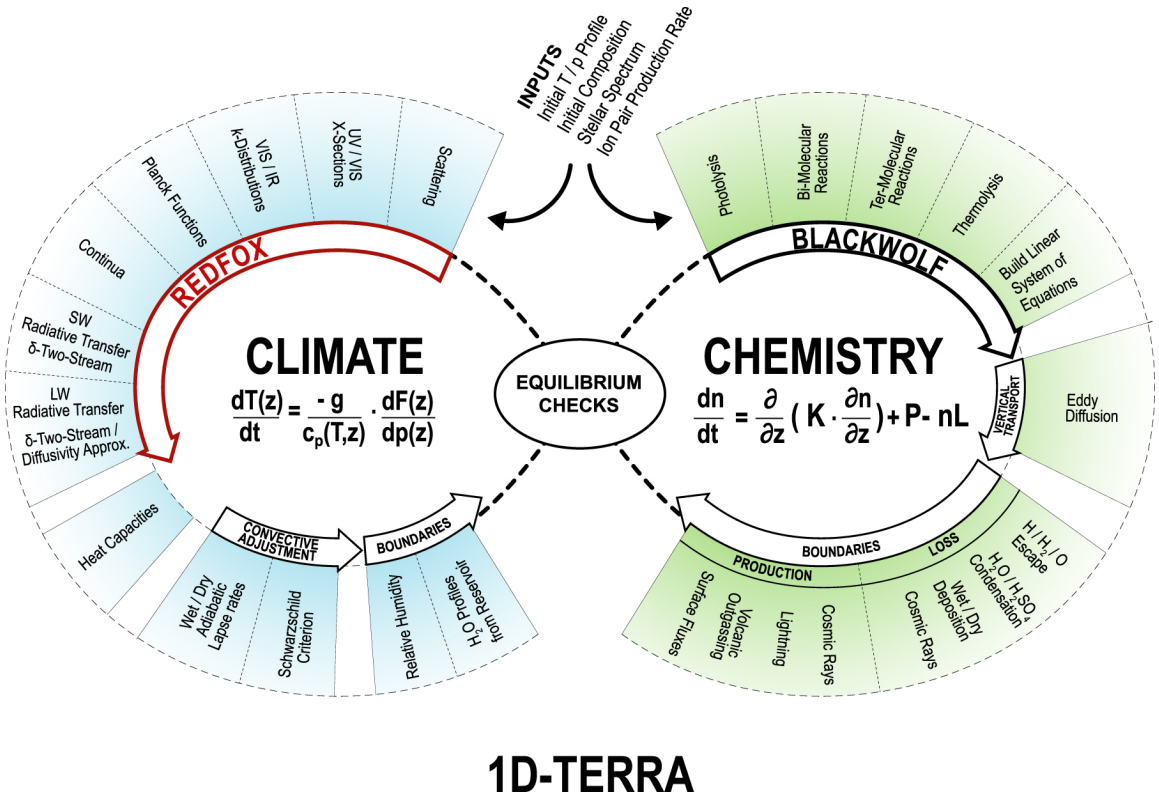


**Figure 3.2: Schematic overview of 1D-TERRA.** The figure shows the different input parameters needed for the calculation as well as the interaction between the two modules (climate and chemistry) of 1D-TERRA (Scheucher et al. (2020), reproduced with permission of the authors).

### 3.2.2 AtRIS

AtRIS was developed by Banjac et al. (2019) and models the interaction of energetic particles and electromagnetic radiation with the surrounding planetary atmosphere. It is based on the **GE**neration **AN**d **T**racking of particles version 4 (GEANT4) code and provides the needed ionization rates used in ExoTIC (Herbst et al., 2019a). It uses a Monte Carlo approach to simulate the path of energetic particles through matter (Agostinelli et al., 2003; Banjac et al., 2019). AtRIS opens up the possibility of using any kind of atmosphere (also exoplanetary), produced by chemistry climate models. It also includes features for calculating the effect of galactic cosmic ray induced interactions (Banjac et al., 2019).

As already mentioned, AtRIS relies on the GEANT4 code and uses primary particles, described by their quantities energy, position and direction. The propagation of the particles through the atmosphere follows a step-by-step method and uses probability density functions (PDFs) of the physical processes to evaluate the effect on the surrounding

atmosphere. This continues until the particles have nonzero kinetic energy. In the end, AtRIS provides the ionization rate of these particles dependent on the altitude levels (Banjac et al., 2019).

### 3.2.3 GARLIC

GARLIC stands for **G**eneric **A**tmospheric **R**adiation **L**ine-by-line **I**nfrared **C**ode and is used for calculating synthetic transmission or emission spectra of the modeled atmospheres by taking as input the atmospheric composition, pressure and temperature profiles from 1D-TERRA infrared code. It is a line-by-line infrared code and uses molecular data from the HITRAN database (Herbst et al., 2019a; Herbst et al., 2022). GARLIC solves the radiative transfer, described by the Schwarzschild equation, using Beer's law to account for molecular absorption (Schreier et al., 2014).

In the line-by-line approach, the absorption cross sections of the molecules are given as a superposition of many lines. Each of them is a combination of the line strength (temperature-dependent) and the different broadening mechanisms, like pressure and Doppler broadening. For numerical reasons the radiative transfer equations have to be solved in discrete steps. Therefore, the atmosphere is divided into homogeneous layers for which the transmission is calculated and the product of all layers gives the total transmission (Schreier et al., 2014). The resulting theoretical transmission or emission spectra provide a crucial link with observations since they can be used to calculate the detectability (signal-to-noise ratio) of a particular absorption band for a given species (the "signal") against the computed net noise threshold of an instrument simulator (the "noise") over a given viewing period.

The method, which includes the different models and was presented in this chapter is applied to various atmospheric scenarios in the following chapters. The model chain shown in figure 3.1 is an efficient way to link detailed and computationally intensive models. The development of ExoTIC plays a key role in investigating the scientific case and forms the basis to produce transmission spectra that could be measured by current and future missions.

# 4 Sensitivity Studies – Experiments with Modern Earth

As part of my doctoral thesis, new reaction pathways described in chapter 3 for $H_2/H_2O$ ionization and formation of $N_2O$ were implemented. A master's thesis supervised there also included sulfur chemistry to account for Venus-like atmospheres (Schleif, 2024). The formation of $N_2O$ in Earth's atmosphere has already been measured (Sheese et al., 2016). The ionization of $H_2/H_2O$ and sulfur chemistry are happening in Earth's atmosphere as well, but should play a minor role compared to $N_2O$ formation.

This chapter uses the well-studied solar particle event known as the Halloween storm in 2003 to examine the impact of these reactions in a familiar scenario. An important question is whether the results are consistent with previous measurements or observations and whether the implementation of $H_2/H_2O$ ionization and sulfur chemistry leads to unrealistic results.

## 4.1 Ionization Rates

To validate the new reactions, ExoTIC uses the ionization rates (IRs) of the Halloween storm in 2003, which was a solar proton event (SPE), one of the strongest in recent history, well documented and observed by spacecraft and satellite instruments like the solar and heliospheric observatory SOHO (Tsurutani et al., 2005). The ionization rates of the Halloween SPE are based on the **A**tmospheric **I**onization during **S**ubstorm **A**ctivity (AISstorm) model. It is the successor of the ionization model AIMOS, which computes atmospheric ion pair production rates out of particle flux measurements (Wissing et al., 2010). Figure 4.1 (a) shows the averaged IRs of the Halloween SPE for the period from $28^{th}$ to $29^{th}$ of October, where the solar storm had its peak. In the following sections, it is thus possible to evaluate the model, in particular the reactions with the excited state of molecular nitrogen against other models and observations (Baumgaertner et al., 2010, Funke et al., 2011, Kelly et al., 2018).

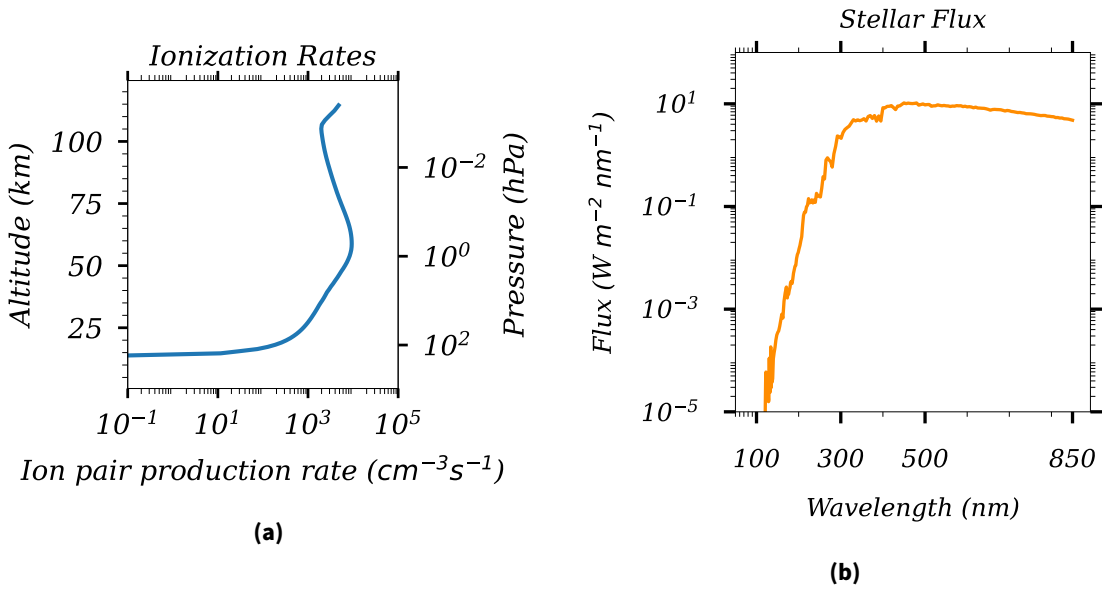


**Figure 4.1: Ion pair production rates and solar flux.** The figure shows the ion pair production rates (a) of the Halloween storm 2003 calculated by the AISstorm model on a daily output (Borthakur, 2025). The peak of this solar storm was on the 28$^{th}$ and 29$^{th}$ of the year 2003. The blue line in plot (a) indicates the average over these two days. It is used as input in the ExoTIC run with atmospheric conditions of modern Earth. The right plot (b) shows the stellar/solar flux at top of atmosphere (TOA), which is used for the photochemical module of ExoTIC.

## 4.2 Simulation Setup

In this validation setup, an atmosphere with composition of modern Earth provided by 1D-TERRA (DLR) is used. Figure 4.2 (b) shows the volume mixing ratio of various selected species like $N_2$, $O_2$, $H_2O$ or $O_3$, which are comparable to the mean profiles of modern Earth (see 2.1). The ozone profile peaks at an altitude of ~ 30 km and ~ 85 km, indicating the main ozone layer in the Earth's stratosphere and the secondary ozone layer in the mesosphere (Evans & Llewellyn, 1972). The water profile shows a decrease of the volume mixing ratio up to the tropopause and stays nearly constant up to the thermosphere, which is consistent with data obtained by the **M**ichelson **I**nterferometer for **P**assive **A**tmospheric **S**ounding (MIPAS) instrument (Stiller et al., 2012).

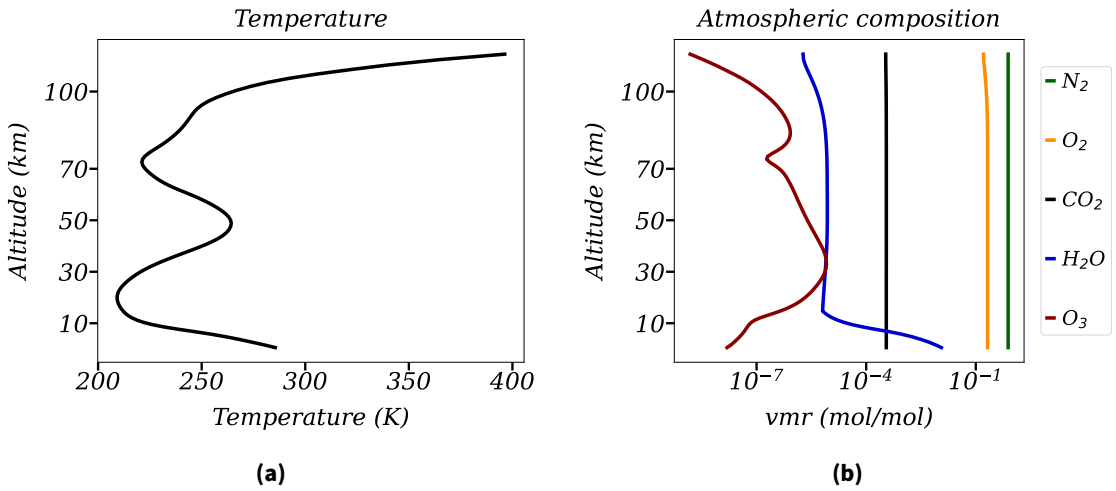


**Figure 4.2: Temperature and atmospheric profile of modern Earth model run.** The temperature (a) and atmospheric profile of different species (b) of modern Earth. Together with various other species –the most important ones are shown for clarity – the profiles are used as initial values for the ExoTIC model runs.

To calculate the temperature-dependent rate coefficients of the chemical equations within ExoTIC, a temperature profile has to be provided by 1D-TERRA (shown in figure 4.2 (b)). After an initial decrease in temperature from ~ 285 K at the surface layer to ~ 210 K at the tropopause, the profile clearly shows an increase within the stratosphere up to the stratopause at around 50 km, followed by another decrease up to the mesopause (~ 80 km). Above, the thermosphere or ionosphere is characterized by an increase in temperature.

The second input needed is the ionization profile, provided by the AISstorm model (see Figure 4.1 (a)) and peaking around 50 km with maximal values approaching $10^4$ $cm^{-3}s^{-1}$. This is in good agreement with previous studies of the Halloween event (Jackman et al., 2005, Funke et al., 2011). The photochemistry is driven by the spectrum of the sun. Figure 4.1 (b) shows the input data for the flux at the top of atmosphere (TOA) within a range from 120 to 850 nm.

ExoTIC can distinguish between different planets, whereas the Earth with its specific orbital parameters is used in this chapter. They are listed in the table 4.1 and determine the solar/stellar zenith angle (SZA), which is important for the photochemistry and the calculation of the photolysis rates.

**Table 4.1: Overview of the used physical model parameters for Earth.** The table shows the physical parameters used for the model simulations of modern Earth.

| Parameter | Value |
|---|---|
| surface pressure (hPa) | 1013.0 |
| length of day (h) | 24.0 |
| length of year (d) | 365.256 |
| planet mass (kg) | $5.9722 \times 10^{24}$ |
| planet radius (km) | 6371.0 |
| solar mass (kg) | $1.988\,55 \times 10^{30}$ |
| mean surface albedo | 0.3 |

Figure 4.3 illustrates the calculated values of the SZA for Earth. Since ExoTIC is a 1D model, there is only one latitude and longitude, which are set to 60° N and 0° for this model run, respectively. 60° N is within the polar cap and directly affected by energetic particle events. The chemistry is performed over the full range of 100 vertical levels.

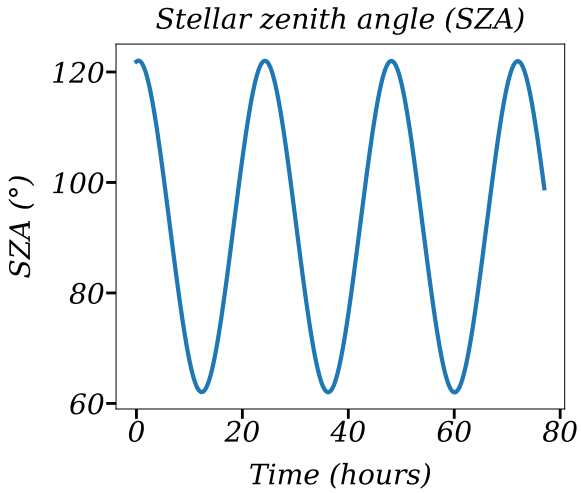


**Figure 4.3: Stellar zenith angle for the Earth.** The plot shows the Earth's stellar zenith angle of the ExoTIC output at 60° N, starting with nighttime conditions (SZA > 90°).

The ionization event starts in the 24$^{\text{th}}$ model hour after a preceding spin-up period and lasts for 24 hours. Due to the limited time available on the HPC cluster for one job, the ion chemistry runs in parallel (one task for each of the 100 layers) and is restarted for every model hour during the event. This reduces the amount of requested time for one job and accelerates the scheduling process.

Within one model hour, ExoTIC performs 20 chemical timesteps and as soon as the ionization event starts, the ion chemistry routine is called at every second chemical time step (six minutes), producing the chemical production rates, which are used for the next neutral chemistry step as well. The runs finish after ~80 model hours with a time resolution of 15 minutes. For the actual validation of the newly implemented reactions, four different setups have been created. Starting from a reference run with the original chemical setup, the reactions shown in Tables 3.4, 3.5, and 3.6, as well as the sulfur chemistry, which was implemented by Schleif (2024), are gradually added. The final result is a version that contains all new reactions. Table 4.2 summarizes these different sensitivity cases.

**Table 4.2: Overview of the performed model runs for the validation.** The Table gives an overview over the different sensitivity cases, indicating which part of the (ion)chemistry is switched on or off. The new reactions are gradually added to the reference case, ended up in a version including all extensions.

| Model Run | $H_2/H_2O$ ionization | Sulfur Chemistry | Excitation of $N_2$ |
|---|---|---|---|
| Reference (original setup) | off | off | off |
| $N_2O$ formation | off | off | on |
| Sulfur chemistry | off | on | on |
| $H_2/H_2O$ ionization | on | on | on |

To evaluate the actual effects of these reactions during an energetic particle event on the atmosphere compared to the original chemical setup, a difference of a difference can be calculated. Firstly, the influence of the background is eliminated by subtracting a base run without an event from the run with a particle event. This is done for each of the individual model setups of Table 4.2. Subsequently, one can subtract the event-adjusted model run without newly implemented reactions from all other model runs. This kind of analysis is used and shown in most of the upcoming plots.

## 4.3 Model Simulations

Firstly, this section compares the response of NO, $NO_2$ and Ozone ($O_3$), since these are well known from model studies and measurements. Subsequently, the abiotic formation of $N_2O$ is analyzed and evaluated against observations. Finally, the effects of $H_2/H_2O$ ionization on the directly affected species $H_2O$ and H are investigated.

## Nitrogen Oxides (NO, $NO_2$) and Ozone ($O_3$)

The composition changes of nitrogenic species and ozone during the Halloween storm in October 2003 have been observed especially by the MIPAS instrument and have been modeled by several studies (Baumgaertner et al., 2010, Funke et al., 2011). The measurements of this energetic particle event provide a good basis to validate the new implemented (ion)chemical reactions, mentioned in chapter 3. Figures 4.4 – 4.6 show the results of the different sensitivity experiments for NO, $NO_2$ and $O_3$.

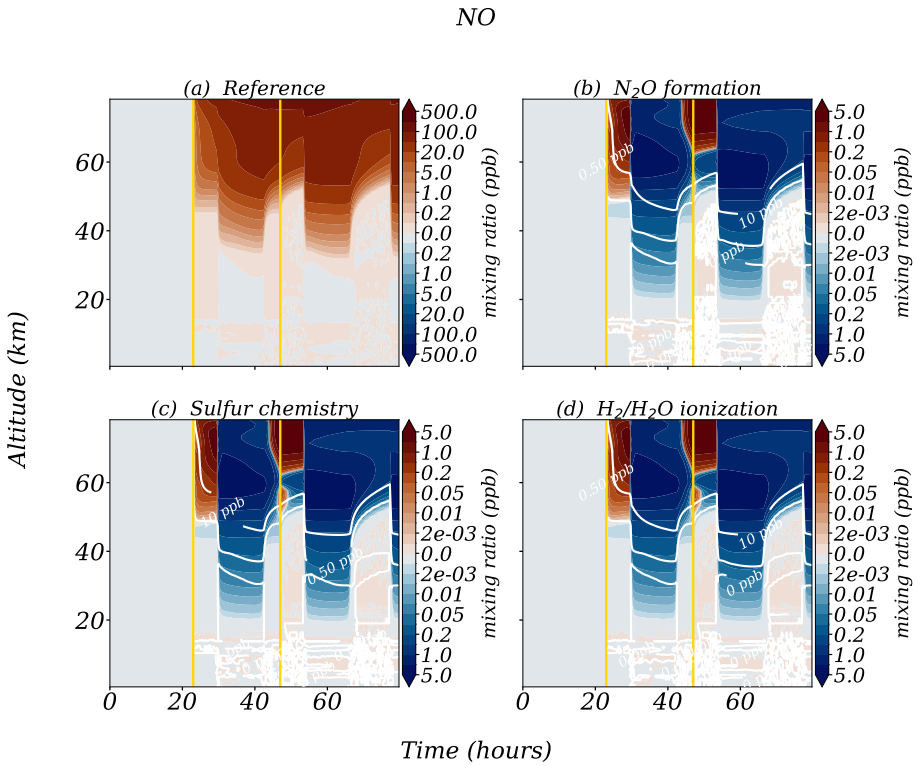


**Figure 4.4: Absolute differences in the volume mixing ratio for NO.** Plot (a) of this figure shows the absolute difference between a model run with and without ion chemistry for the original (ion)chemical setup. The same is done for the remaining three setups whose results are indicated by the white contour lines. For these three setups, plot (a) is additionally subtracted to obtain the actual changes when modifying the (ion)chemical setup. This is shown by the colored contours of the modified model runs (b–d). The vertical yellow lines indicate the start and end points of the ionization event. The spacing of the contour lines within each order of magnitude is 1, 2, 5. For clarity, only every fourth white contour line is shown. Note the different scale of the colorbars between (a) and (b–d).

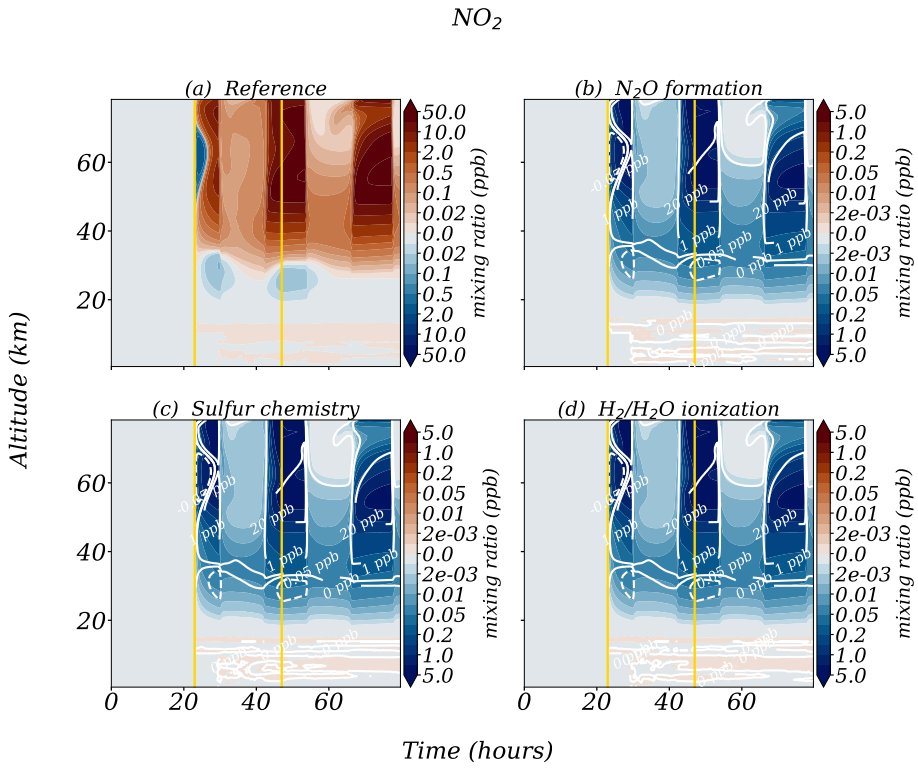


**Figure 4.5: Absolute differences in the volume mixing ratio for $NO_2$.** Same analysis as figure 4.4 but for $NO_2$.

First, looking at the model run with the original chemical setup (a). The mixing ratio at around 60 km changes within the particle event by ~50 ppb for NO and ~30 ppb for $NO_2$. This is in good agreement with the studies of Funke et al. (2011) and Baumgaertner et al. (2010), where the changes in NO and $NO_2$ during the particle event on October 29 are comparable in magnitude. Additionally, the ExoTIC data show a clear diurnal cycle of the two $NO_x$ species beginning with the first sunrise after the event start. For $O_3$, there is an overall decrease by about 1–5 ppm (Fig. 4.6 (a)), which corresponds to an ozone loss of up to 60 – 90% (Fig. 4.7 (a)). This also matches the observations of MIPAS during the Halloween storm between 50 and ~70 km (Baumgaertner et al., 2010).

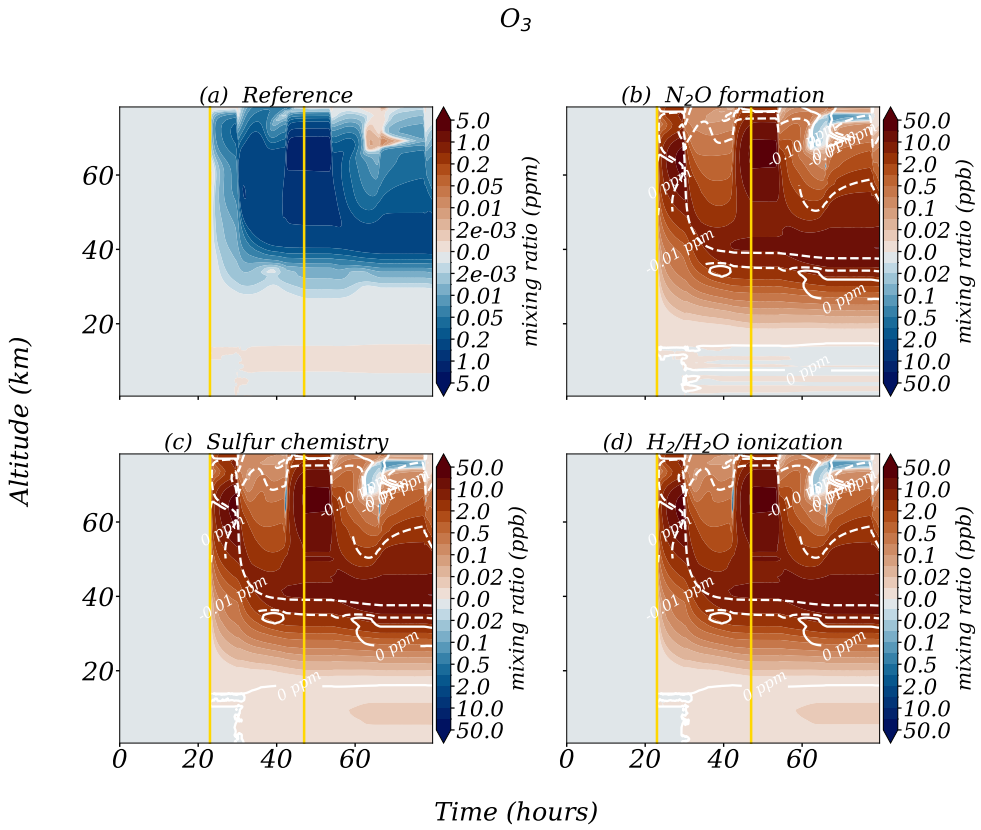


**Figure 4.6: Absolute differences in the volume mixing ratio for $O_3$.** Same analysis as figure 4.4 but for $O_3$.

By including the different reactions (plots (b–d)), there is an additional ~5 ppb of NO at the beginning of the particle event compared to the original setup in Fig. 4.4 (a). On the other hand, $NO_2$ is reduced by ~5 ppb immediately after the particle event (Fig. 4.5 (b–d)), but then recovers with the onset of daylight, only showing a difference of several ppt[1]. In contrast, the NO mixing ratio is reduced up to 5 ppb in all other sensitivity runs after the first sunrise during the particle event (Fig. 4.4 (b–d)). The plots show that the changes in the mixing ratio for the two $NO_x$ species NO and $NO_2$ aren't influenced by $H_2/H_2O$ ionization and sulfur chemistry, but only by $N_2O$ formation. The changes of about 5 ppb are small compared to the original case (a) and still match the observations by Baumgaertner et al. (2010) and Funke et al. (2011).

[1] ppt: parts per trillion ($10^{-12}$ mol/mol)

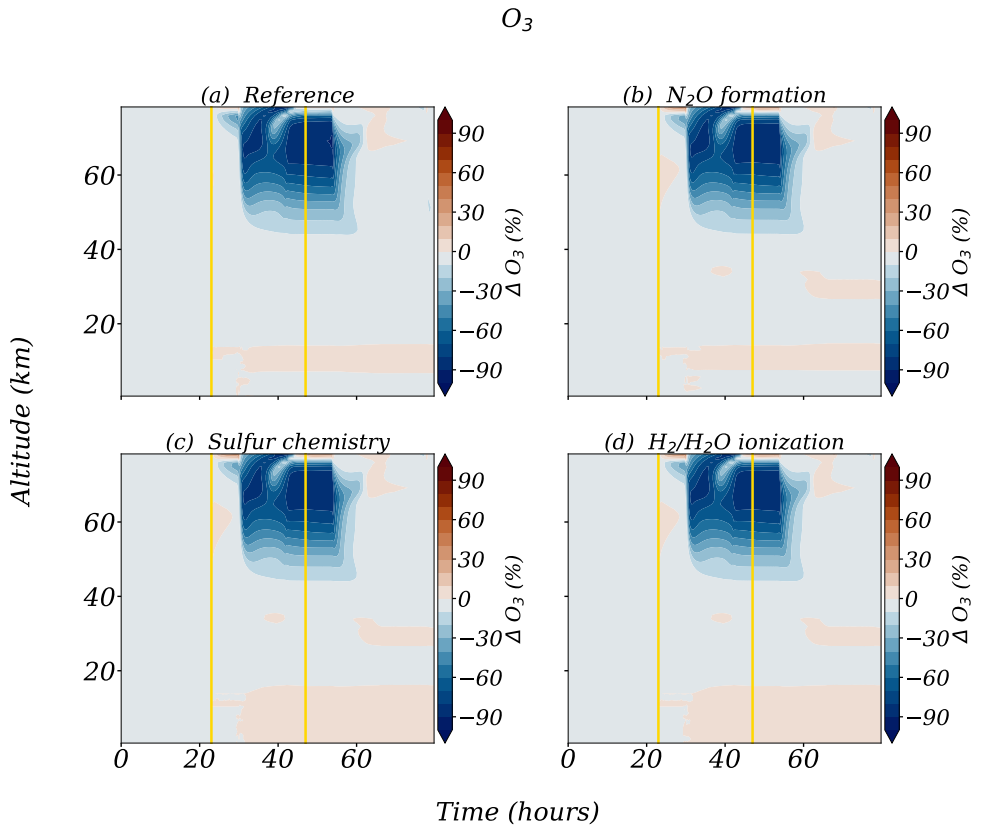


**Figure 4.7: Relative change (%) in the $O_3$ mixing ratio for all sensitivity experiments.**

The same holds for $O_3$, where the mixing ratio increases by about 50 ppb compared to the reference run, but there is still an ozone loss of 60 – 90% above ~50 km. Here, only $N_2O$ formation changes the mixing ratios. Overall, it also agrees with the observations by Baumgaertner et al. (2010) and Funke et al. (2011).

This overall ozone loss during the energetic particle event is due to the enhanced production of NO/$NO_2$ and H/OH species, enabling the catalytic cycles R36–R38 and R39–R41. The efficiency of the $NO_x$ catalytic cycle increases during daytime, because of the photolysis of $NO_2$. Now let's have a look at the differences between the original chemical setups in (a) and the other sensitivity experiments in plots b to d. Besides the $N_2O$ forming process (R21 and R22), the excited state of $N_2$ also forms additional atomic oxygen by reaction R24. The higher amount of atomic oxygen leads to more ozone production due to R33 right after the start of the particle event (see Fig. 4.6). Subsequently, more ozone produces more NO via R62.

$$N + O_3 \longrightarrow NO + O_2 \qquad \text{(R62)}$$

Thus, the balance between formation and loss of NO is at higher values compared to the model run without excited $N_2$, leading to a positive difference for NO seen in figure 4.4 (b–d). Regarding the $NO_2$ mixing ratio in figure 4.5 (b)–(d), the reduction by ~5 ppb arises from the additional $N_2O$ producing pathway R22, which consumes $NO_2$ molecules.

Due to the initial loss of $NO_2$ by R22, less NO is produced during daytime by the photolysis of $NO_2$, which leads to less NO compared to the reference run without $N_2O$ formation reactions. Within the $NO_x$ cycle, the equilibrium between NO and $NO_2$ is shifted towards $NO_2$, reducing the initial difference caused by R22. Within the next part, the actual $N_2O$ producing mechanism is discussed in more detail.

### Abiotic production of $N_2O$

The results by adding the $N_2O$ formation mechanism to the ExoTIC model are shown in figure 4.8. As in the previous section, four different sensitivity experiments were performed according to Table 4.2. The comparison between the model runs with and without energetic particles shows differences of ~1 ppt for the reference run without $N_2O$ production (Fig. 4.8 (a)). These changes occur with the first sunrise after the particle event starts. By including $N_2O$ production, the changes differ drastically compared to (a). The sensitivity experiments (b–d) show increased $N_2O$ of 10–50 ppb above 60 km, which leads to the conclusion that the major differences arise from the new $N_2O$ producing reactions. Thus, $H_2/H_2O$ ionization and sulfur chemistry do not have a significant influence.

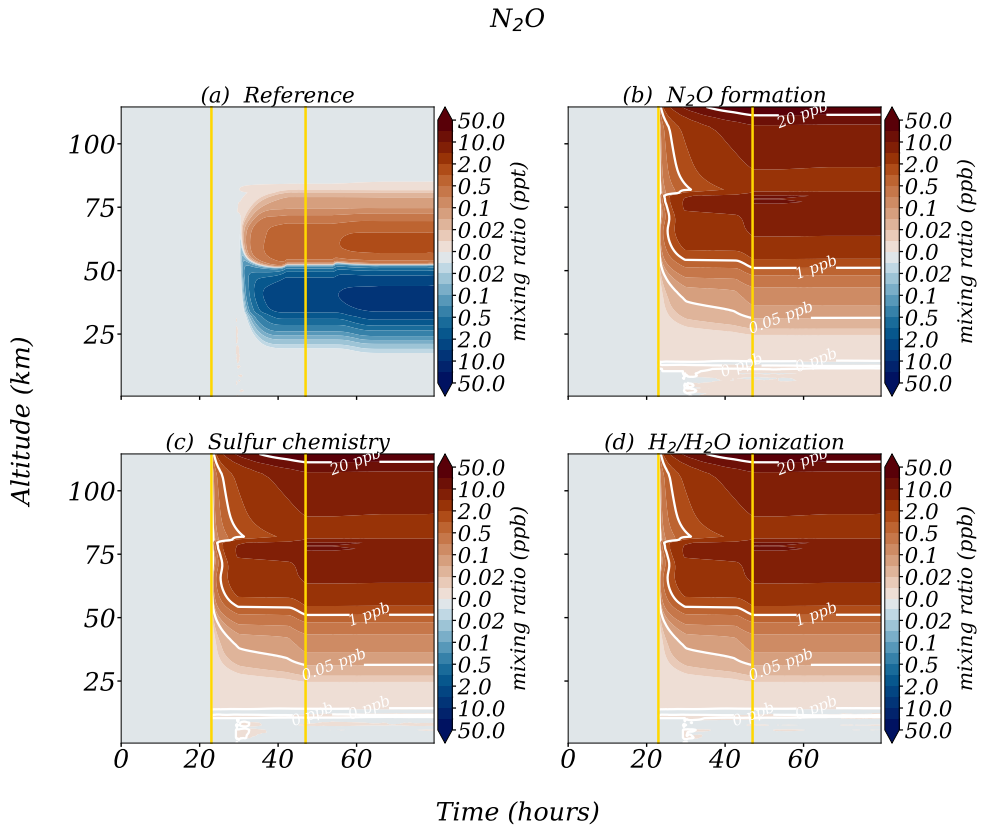


**Figure 4.8: Absolute difference in the volume mixing ratio for $N_2O$.** Same analysis as figure 4.4 but for $N_2O$.

For the reference run, the differences can be explained by the reaction of $N_2O$ with $O(^1D)$. Above ~50 km, less reactive $O(^1D)$ (see Fig. 4.9 (a)) is produced by R63 during the particle event, because $O_3$ is destroyed by the $NO_x$ and $HO_x$ catalytic cycles.

$$O_3 + h\nu \longrightarrow O_2 + O(^1D) \tag{R63}$$

This is not visible for the cases (b–d), because the production of $N_2O$ is orders of magnitude larger and slower depletion of $N_2O$ via $O(^1D)$ is insignificant. Baumgaertner et al. (2010) compares MIPAS measurements of $N_2O$ with EMAC model output during the Halloween storm in October 2003. The amounts of produced $N_2O$ (Fig. 4.8 (b–d)) of about 1–10 ppb at the particle storm's peak at an altitude of ~60 km are in good agreement with this study.

As mentioned in chapter 2 and 3, there are different ways of producing abiotic $N_2O$. On the one hand, through reaction R21 and on the other hand via reaction R22.

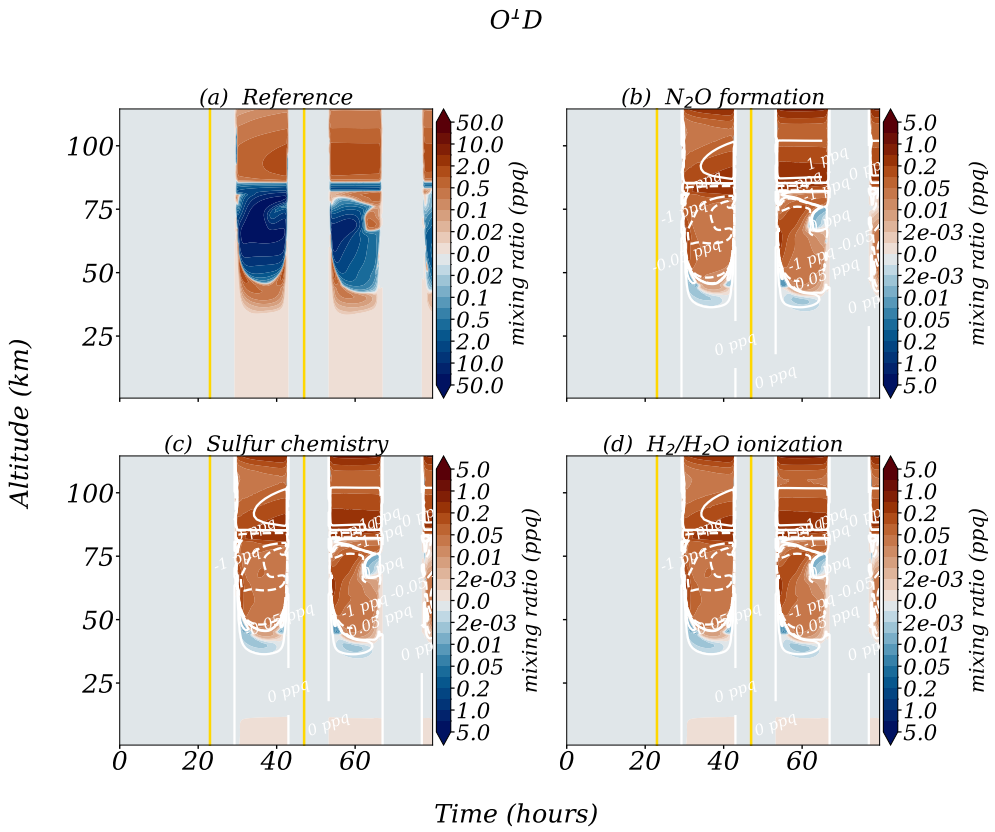


**Figure 4.9: Absolute difference in the volume mixing ratio for O($^1$D).** Same analysis as figure 4.4 but for O($^1$D).

Kelly et al. (2018) mentioned that the production path via the excited state of $N_2$ plays an important role above ~90 km. At lower altitudes, reaction R22 gains more importance due to the production of atomic nitrogen. To verify this behavior also within ExoTIC, one can use the reaction rates (see 2.6) of the involved chemical equations. Figure 4.10 shows the reaction rate of these two $N_2O$ producing pathways. In 60–80 km, reaction R22 is dominating. Above 80 km and below 60 km, the chemical reaction rate via the excited $N_2$ is predominant.

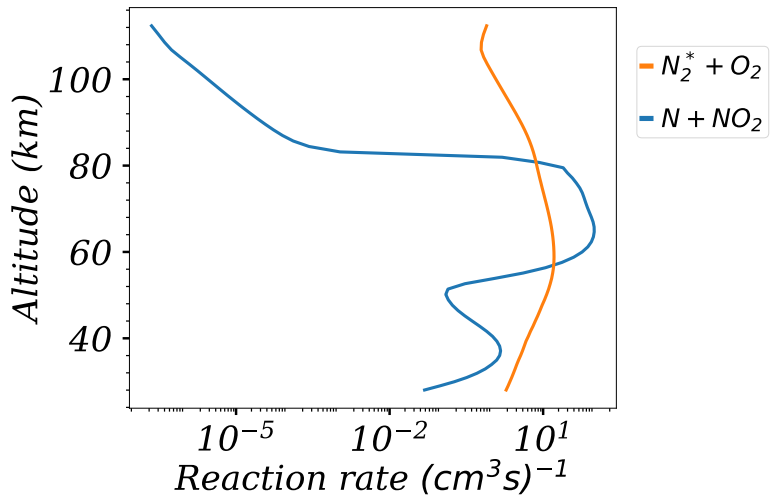


**Figure 4.10: Reaction rates of the $N_2O$ producing reactions.** The figure shows the mean reaction rate of the $N_2O$ producing pathways (blue and orange line). The mean covers the period of the Halloween event in the ExoTIC model runs.

### Impact on H and $H_2O$

Lastly, the influences of $H_2$ and $H_2O$ ionization are briefly discussed in this part. Figure 4.11 shows the changes of atomic hydrogen for the different sensitivity setups given in table 4.2. Compared to the sensitivity runs without $H_2$ and $H_2O$ ionization (Fig. 4.11 (a–c)), there is an increase of H by about 10 ppb in the thermosphere above 90 km. In this context, additional sulfur chemistry and $N_2O$ formation have no significant influence on H in this altitude region, as the changes are in the ppt range (Fig. 4.11 (b+c)).

The energetic particles for example form $H_2^+$ ions, which can then recombine with surrounding electrons to atomic hydrogen. This happens in the lower thermosphere above ~90 km and can explain the additional H when $H_2/H_2O$ ionization is included. Since the concentration of atomic hydrogen on Earth is in the ppm range, $H_2$ ionization could have a significant impact on planets with $H_2$-dominated atmospheres.

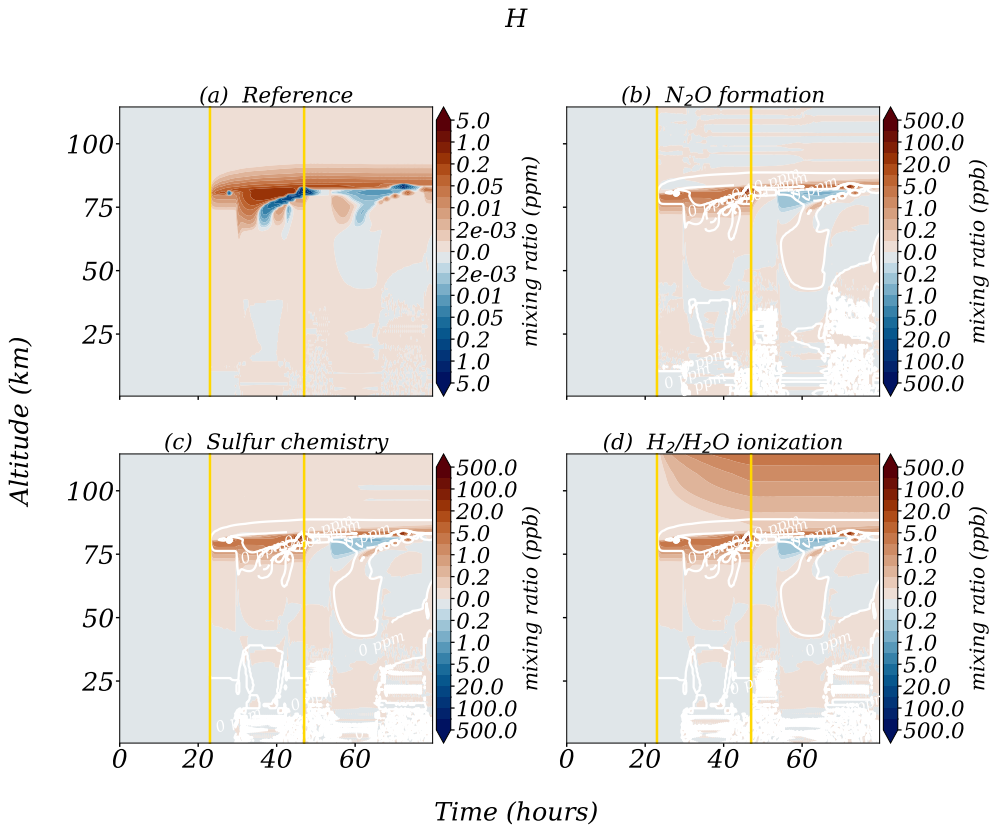


**Figure 4.11: Absolute difference in the volume mixing ratio for atomic hydrogen (H).** Same analysis as figure 4.4 but for atomic hydrogen.

Regarding the $H_2O$ ionization, there is a similar effect in the lower thermosphere. Above 90 km, the water vapour vanishes by a few ppt (Fig. 4.12 (d)) compared to the model run without water vapour ionization (b+c). The ionizing particles lead to the dissociative ionization of water vapour and reduce its amount. This small difference can be explained by the fact that the water mixing ratio at this height is rather small.

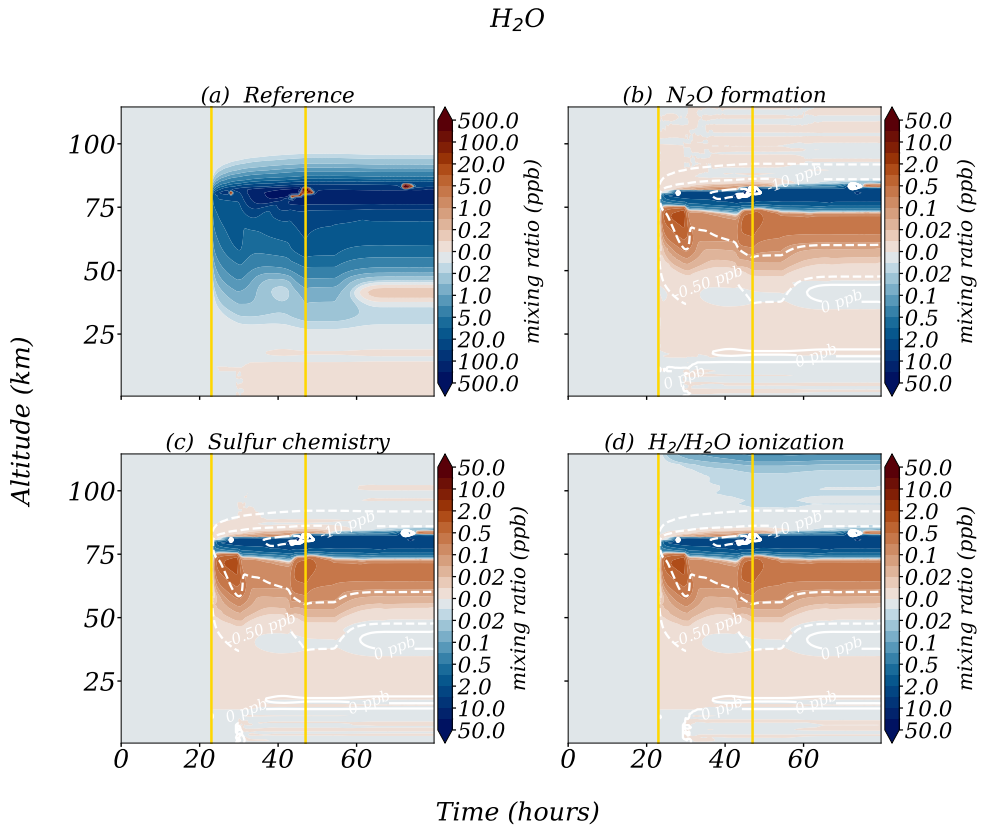


**Figure 4.12: Absolute difference in the volume mixing ratio for water vapour ($H_2O$).** Same analysis as figure 4.4 but for $H_2O$.

At ~75 km and below, there is an enhancement of water vapor in the model runs with additional $N_2O$ chemistry of ~2 ppb. The additional atomic oxygen by R21 and R22 reduces the hydroxyl radical OH (R64). The produced hydrogen in Fig. 4.11 (b–d) then forms water via reaction R65.

$$OH + O \longrightarrow O_2 + H. \tag{R64}$$

$$H + HO_2 \longrightarrow H_2O + O. \tag{R65}$$

These changes are at least an order of magnitude smaller than the water loss and subsequent $HO_x$ production during the actual particle event between ~50 and ~70 km (Sinnhuber et al., 2012) (Fig. 4.12(a)). In the next chapter, the latest setup will be applied with all new reactions to more exotic atmospheres in order to investigate their effects on atmospheric composition in more detail.

# 5 Particle Precipitation in Exoplanetary Atmospheres

The model versions described in chapter 3 and evaluated in chapter 4, are used for performing different model simulations with various planets orbiting around M-dwarf stars. Since current knowledge about the exact composition of exoplanetary atmospheres is limited, it is a good approach to start by investigating Earth-like atmospheres around M-type stars. The favored target TRAPPIST-1 (Gillon et al., 2016), which is a particular active M-dwarf star with enhanced particle fluxes, motivates the investigation of the effects of energetic particle events on the composition of such planets.

In addition to quite active stars, stars with lower activity are also observed, including the red dwarf LHS 1140. Here, galactic cosmic rays are a more important component of energetic particles. Since the planet around LHS 1140 is bigger than Earth, there is the possibility to investigate more exotic atmospheres compared to the planets around TRAPPIST-1. Hence, this chapter presents the ion-chemical impact on the atmospheres of two planets within those planetary systems and discusses the influence on observable transmission spectra.

## 5.1 TRAPPIST-1 e – Planet around an active M-dwarf Star

The TRAPPIST-1 planetary system was discovered by Gillon et al. (2016) using the TRAPPIST telescope (**TRA**nsiting **P**lanets and **P**lanest**I**simals **S**mall **T**elescope), which also gives the system itself its prominent name. First, the authors reported three Earth-sized planets around an already known and classified cool M8 star, located at a distance of 12 pc[1] (Gillon et al., 2016). Later it turned out that this planetary system consists of seven almost Earth-sized planets, three of which are close to or in the habitable zone and potentially harbor liquid water (Gillon et al., 2017). They are referred to as TRAPPIST-1 e, f and g.

[1] Parsec: $1\,\mathrm{pc} = 3.26\,\mathrm{ly} = 3.09 \times 10^{13}\,\mathrm{km}$

Figure 5.1 shows a comparison between the solar terrestrial planets (blue-dotted circles) and the TRAPPIST-1 system with its seven rocky Earth-sized planets. The habitable zone of the planetary system is indicated by the brown band at the top edge of the inner picture. As already mentioned, the luminosity of M-dwarf stars is lower than for G-type stars (Fig. 2.1), the habitable zone is much closer to the host star in order to get almost the same amount of irradiation.

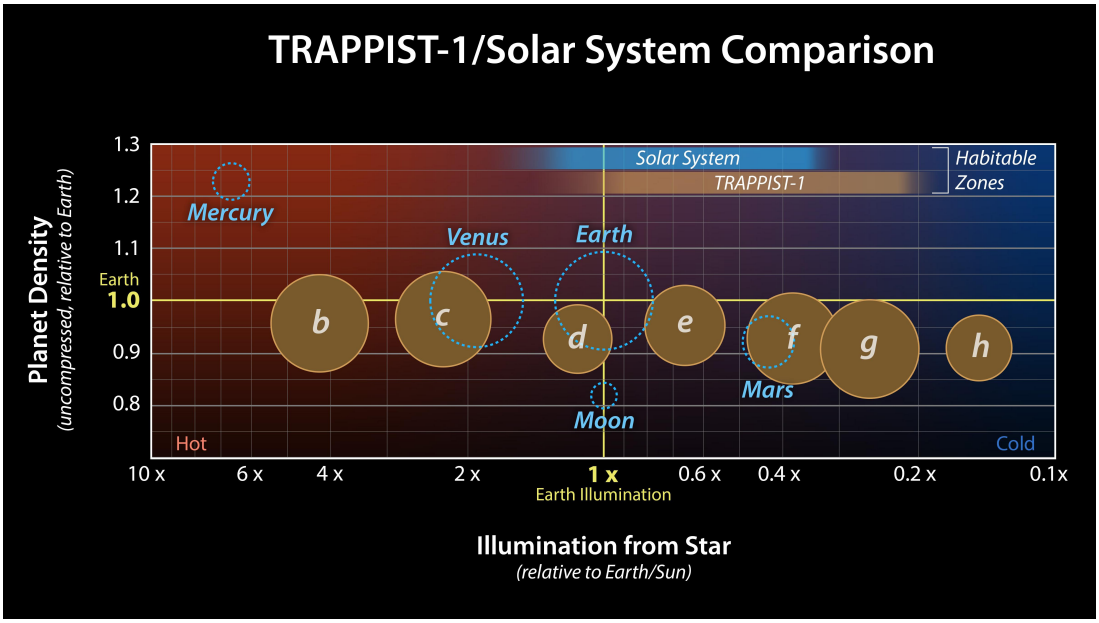


**Figure 5.1: Comparison of the Trappist-1 system with the solar system.** This figure compares the sizes of the rocky solar system planets to the TRAPPIST-1 system. All seven planets (b–h) are almost Earth-sized and receive 4 to ~0.15 times the solar irradiation $S_{\odot}$. The figure is taken from[2](credit: NASA/JPL-Caltech).

The focus in this section is on the planet TRAPPIST-1e, located at the inner edge of the habitable zone around TRAPPIST-1. Table 5.1 gives an overview of the main physical properties of TRAPPIST-1e and its host star, which are used in the model simulations with ExoTIC. The upcoming section describes the simulation setup in more detail.

[2] https://www.jpl.nasa.gov/images/, last visited on December 9, 2025.

**Table 5.1: Overview of the physical parameters for the TRAPPIST-1e system.** This table shows the physical parameters of the TRAPPIST-1 system. The planet TRAPPIST-1 (e) is an Earth-sized planet in the habitable zone of TRAPPIST-1 (see Fig. 5.1). The same values for day and year indicate the most likely tidally locked character.

| Parameter | Value | Reference |
|---|---|---|
| Stellar Mass ($M_\odot$) | $0.089 \cdot M_\odot$ | Grootel et al. (2018) |
| Stellar Radius ($R_\odot$) | $0.121 \cdot R_\odot$ | Grootel et al. (2018) |
| Stellar Temperature (K) | 2516 | Grootel et al. (2018) |
| Length of Day (Earth days) | 6.1 | Agol et al. (2021) |
| Length of Year (Earth days) | 6.1 | Agol et al. (2021) |
| Planet Mass ($M_\oplus$) | $0.692 \cdot M_\oplus$ | Agol et al. (2021) |
| Planet Radius ($R_\oplus$) | $0.920 \cdot R_\oplus$ | Agol et al. (2021) |
| Mean Surface Albedo | 0.255 | Wunderlich et al. (2020) |
| Orbital Distance (AU) | 0.029 | Wunderlich et al. (2020) |

### 5.1.1 Simulation Setup

The close orbit at a distance of 0.029 AU and the same values for day and year indicate that TRAPPIST-1e is potentially tidally locked, showing always the same side to the star. Thus, the stellar zenith angle within the ExoTIC model runs is fixed to 60° to approximate the global mean chemistry on the dayside. The orbital distance leads to an incident stellar flux at TOA of 0.604 $S_\odot$, where $S_\odot$ denotes the irradiation at Earth's TOA of 1361 $\mathrm{Wm}^{-2}$ (Wunderlich et al., 2020). Figure 5.2 shows the stellar spectrum received by TRAPPIST-1e. As already mentioned in chapter 2, the flux in the UV and visible part of the electromagnetic spectrum is smaller for M-stars compared to Sun-like stars, but is stronger in the Lyman-$\alpha$ line (around ~120 nm). This spectrum is used as input for the photochemistry module within the ExoTIC model runs.

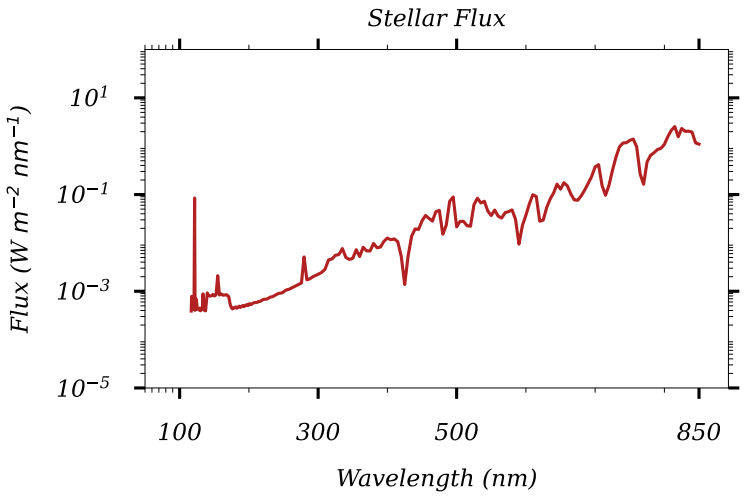


**Figure 5.2: Stellar spectral flux at top of atmosphere for TRAPPIST-1e.** The figure shows the stellar energy distribution at top of atmosphere of TRAPPIST-1e. The stellar spectrum of TRAPPIST-1 is obtained by the Mega-MUSCLES Treasury Survey (Wilson et al., 2021) and scaled to a total integrated energy of 1361 Wm$^{-2}$, corresponding to Earth's received irradiation. Then, the incident radiation on TRAPPIST-1e is equivalent to 0.604 $S_{\odot}$.

### Initial Atmospheres

Since there is currently no confirmed atmospheric composition of rocky Earth-like planets, it is a good starting point to begin with Earth-like atmospheres. The input for ExoTIC is calculated by 1D-TERRA (see 3.2.1) and is based on the work of Wunderlich et al. (2020). There, the authors suggest different $N_2$- and $CO_2$-dominated model scenarios for the almost Earth-sized planet TRAPPIST-1e. The different scenarios each have a $CO_2$ partial pressure of 0.1 or 1 bar in the lowermost atmospheric layer. In total, all model runs have a range of 100 layers from 0 to ~100 km. The scenarios with their mass fraction in the lowermost atmospheric layer are listed in Table 5.2. Three scenarios with varying amounts of water and oxygen are chosen, which are called (according to their respective water and oxygen amounts) Dry or Wet, and dead or alive.

**Table 5.2: Overview of the used model scenarios for TRAPPIST-1e.** The table gives a short overview of the different model experiments used for TRAPPIST-1e and shows the percentage amount of trace gases in the lowermost layer that are important for the atmosphere of the selected scenarios. The $CO_2$ partial pressure changes from 0.1 bar to 1 bar for the different scenarios. The table is adapted from Herbst et al. (2024).

| Scenario | $CO_2$ (%) | $N_2$ (%) | $H_2O$ (%) | $O_2$ (%) |
|---|---|---|---|---|
| Dry-dead (0.1 bar $CO_2$) | 13.3 | 84.0 | $3.47 \times 10^{-4}$ | $2.14 \times 10^{-1}$ |
| Wet-dead (0.1 bar $CO_2$) | 13.4 | 85.0 | $1.49 \times 10^{-1}$ | $7.01 \times 10^{-3}$ |
| Wet-alive (0.1 bar $CO_2$) | 12.8 | 51.7 | $1.95 \times 10^{-1}$ | 34.04 |
| Dry-dead (1 bar $CO_2$) | 61.1 | 34.4 | $2.24 \times 10^{-3}$ | 1.14 |
| Wet-dead (1 bar $CO_2$) | 63.0 | 32.0 | 0.3 | $4.27 \times 10^{-3}$ |
| Wet-alive (1 bar $CO_2$) | 61.2 | 1.13 | 3.82 | 32.77 |

The 'Dry-dead' atmospheric cases assume only volcanic outgassing, whereas the 'Wet' and 'dead' scenarios also assume an ocean. 'Wet-alive' indicates biogenic and volcanic surface fluxes that are measured for Earth, as well as an ocean. The volcanic and/or biogenic emissions can be found in Wunderlich et al., 2020 (Table 4+5). Figure 5.3 shows the full vertical profile of the three different scenarios, 'Dry-dead' (a), 'Wet-dead' (b) and 'Wet-alive' (c) for various atmospheric trace gases. The higher $CO_2$ partial pressure cases are indicated by the dashed-dotted lines. For the 'Wet' scenarios with an additional ocean (b+c), the water vapor content in the troposphere is much higher compared to the 'Dry' scenario. Due to the higher amount of $O_2$, the ozone layer (black curve) is more pronounced for the 'alive' atmosphere (c) in relation to plots (a) and (b).

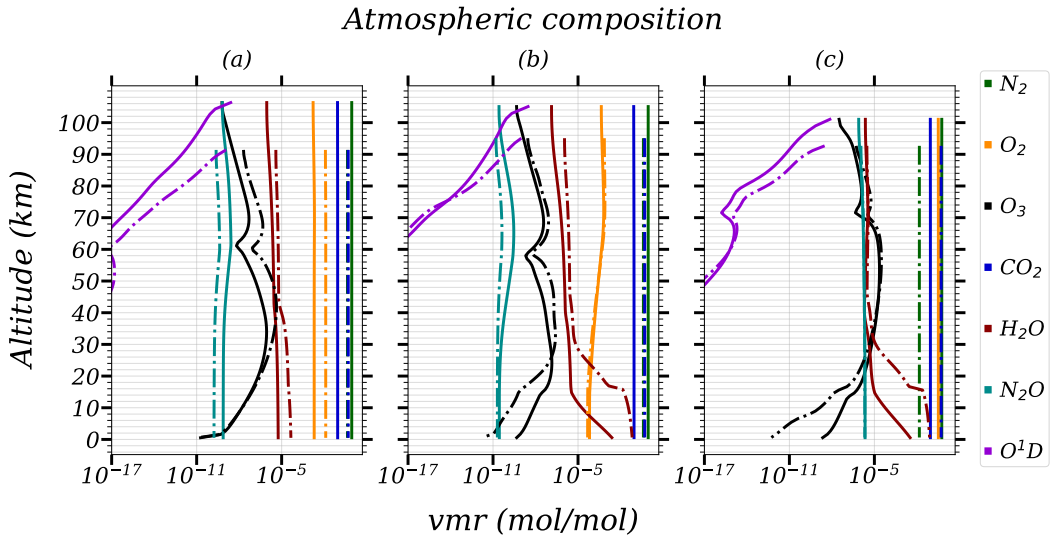


**Figure 5.3: Initial atmospheric composition for the TRAPPIST-1e scenarios.** This figure shows the vertical profiles of various trace gases for the different atmospheric scenarios 'Dry-dead' (a), 'Wet-dead' (b) and 'Wet-alive' (c). The dashed-dotted lines indicate the scenarios with 1 bar of $CO_2$.

In the 'dead' scenarios, oxygen is released from the high amounts of $CO_2$ by reaction with $O(^1D)$ and photodissociation in the upper part of the atmosphere, forcing the abiotic buildup of $O_2$ (Wunderlich et al., 2020). This effect is bigger for the 1 bar scenarios, since there is more available $CO_2$. A higher amount of $O_2$ corresponds to a higher amount of $O_3$ (panels a and b, black lines). Compared to the scenarios with biogenic fluxes (panel (c) in Fig. 5.3), the ozone layers are less pronounced (Wunderlich et al., 2020).

The corresponding temperature profiles based on the initial atmospheric composition of Wunderlich et al. (2020) are shown in Figure 5.4. There are no major differences in the shapes of the temperature profiles, with a very high tropopause up to ~40 km altitude, and a sharp transit from the strato-mesosphere into the thermosphere around 90–100 km. However, a higher surface temperature of 15–20 K can be observed for the scenarios with included ocean, which is attributable to the higher amount of the natural greenhouse gas $H_2O$ (solid lines). Due to higher initial $CO_2$ and $H_2O$ in the 1 bar scenarios, the surface temperature increases up to 340 K (Fig. 5.4, dashed-dotted lines). Wunderlich et al. (2020) also mentions the absent of a temperature inversion in the middle atmosphere compared to Earth, which can be also seen in figure 5.4. This is a result of less stellar flux in the Hartley (200—310 nm), Huggins (310—400 nm), and Chappuis (400—850 nm) bands for M-stars. These bands are responsible for the radiative heating by photochemical depletion of $O_3$ (Wunderlich et al., 2020).

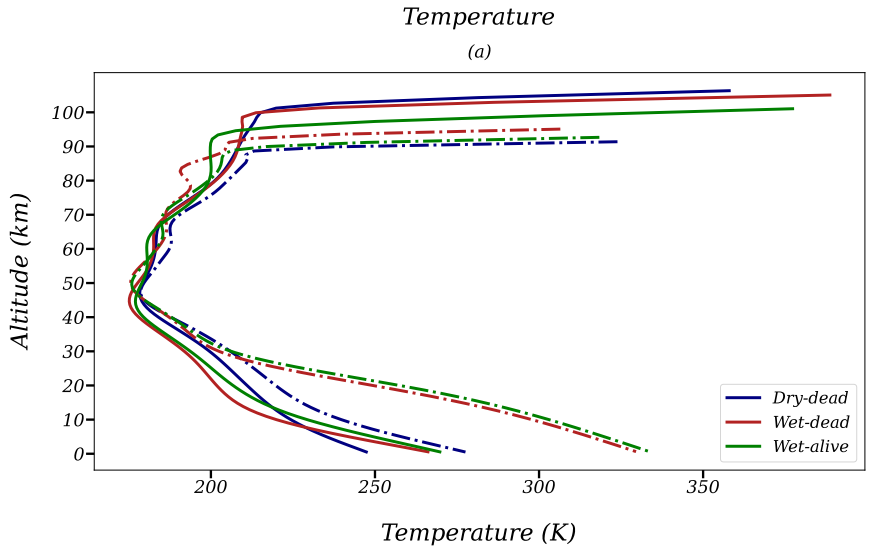


**Figure 5.4: Initial temperature profile for the TRAPPIST-1e model simulations.** The figure illustrates the vertical temperature profile up to ~110 km for the different model simulations 'Dry-dead' (blue), 'Wet-dead' (red) and 'Wet-alive' (green). The surface temperature ranges from ~250 K to ~330 K, allowing liquid water on the surface in particular for the 'Wet' scenarios. The dashed-dotted lines indicate the 1bar $CO_2$ scenarios.

### Ionization Rates

In the solar system, one of the strongest recorded flares was the Carrington event in 1859 with an estimated energy of $\sim 10^{33}$ erg (Cliver et al., 2022). This flare resulted in a huge geomagnetic storm, which affected the atmosphere of Earth (Herbst et al., 2024). In a study from Vida et al. (2017), the measured light curves of the M8 dwarf star TRAPPIST-1 showed multiple flares with energies up to $1.24 \times 10^{33}$ erg every ~50 days. This is within the order of the Carrington event and is a good benchmark for the ExoTIC model runs.

According to Herbst et al. (2024), the modeling of historical particle events is based on the spectral profile of measured terrestrial ground level enhancements (GLE). For the Carrington event, the reference is the spectral shape of GLE44, which was detected in October 1989. To use this for TRAPPIST-1e, it is scaled to its orbital distance at 0.029 AU by using the inverse-square law $1/r^2$. Subsequently, it is referred to as a Carrington-like event. Thus, it forms the basis for calculating ionization rates using AtRIS, which are required by ExoTIC for computing the ion chemistry in addition to the stellar spectrum, initial temperature, and atmospheric profiles (Herbst et al., 2024). The results for the different atmospheres ('Dry-dead' (a), 'Wet-dead' (b), 'Wet-alive' (c), solid/dashed-dotted lines) are shown in Figure 5.5. All cases show a similar structure with a maximum of $\sim 2 \times 10^8$ Ions

$cm^{-3}s^{-1}$ between ~30 and 50 km. The atmosphere at this altitude becomes denser, and the energy spectrum of the particles determines the ionization peak.

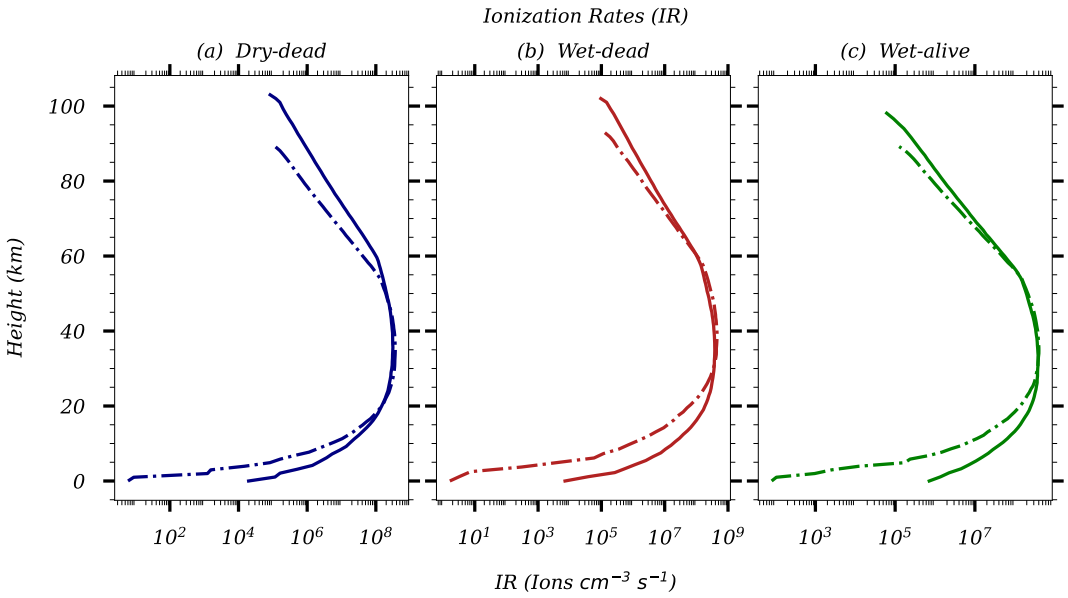


**Figure 5.5: Ion pair production rates for different input atmospheres of TRAPPIST-1 (e).** The Figure shows the ion pair production rates for the energetic particle Carrington-like for the different input atmospheres, 'Dry-dead' (a), 'Wet-dead' (b) and 'Wet-alive' (c). The solid (dashed-dotted) lines indicate the scenarios with 0.1 bar (1 bar) $CO_2$ partial pressure. These ionization rates are published in Herbst et al. (2024).

### 5.1.2 Single Ionization Event

During this doctoral thesis, results of ExoTIC model runs with its older version without additional sulfur chemistry, $H_2/H_2O$ ionization and abiotic $N_2O$ production were carried out by me and published in the peer-reviewed publication Herbst et al. (2024). The following section is based on this study and focuses on the most important findings.

Figure 5.6 shows the vertical profile of the mean differences between a Carrington-like event and a corresponding reference run without particle event for several trace gases and different atmospheric scenarios presented in Herbst et al. (2024). In addition, the plot for $N_2O$ (panel (f) in Fig. 5.6), which is not shown in the publication, was created with the same dataset. The Carrington-like event starts within the $24^{th}$ model hour and lasts for six hours. For all scenarios, there is production of $HO_x$ in the ppb–ppm range throughout the atmosphere during the particle event. The same is true for the production of $NO_x$ up to

70 km. Ozone (Fig. 5.6, panel c) shows alternating regions with formation or loss for all atmospheric scenarios and over all altitudes. For $N_2O$, the most obvious change can be seen in the Wet-alive model runs (green lines), with production up to ~10 ppt between 20 and 70 km.

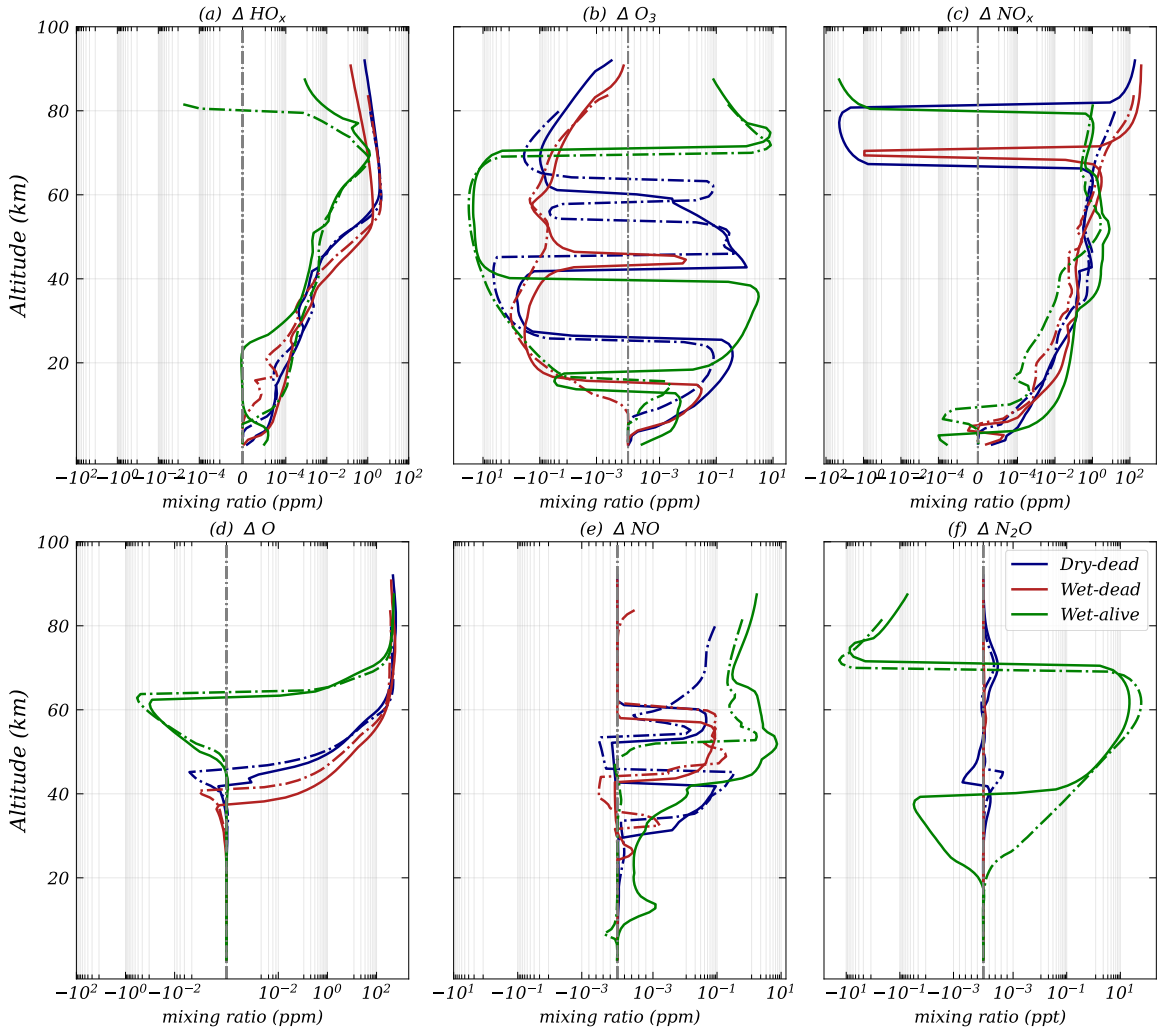


**Figure 5.6: Mean absolute differences in the mixing ratio of various trace gases for TRAPPIST-1e during a Carrington-like event.** The figure shows the mean difference in the mixing ratio of $HO_x$ (H, OH, $HO_2$), $NO_x$ (N, NO, $NO_2$), $O_3$, atomic oxygen (O), NO and $N_2O$ for the scenarios with 0.1 bar $CO_2$ (solid) and 1 bar $CO_2$ (dashed-dotted) during a Carrington-like ionization event. The different colors indicate the various atmospheric scenarios. The plots are based on the dataset, which was used for the publication of Herbst et al. (2024).

The energetic particle event produces $NO_x$ by ionization and dissociative ionization of $N_2$ (Sinnhuber et al., 2012) and $HO_x$ by the formation of water cluster ions with subsequent release of $HO_x$ species (Solomon et al., 1981), leading to overall water loss shown in Fig. 6

in Herbst et al. (2024). Ozone formation above 70 km is likely initiated by the dissociation of $O_2$ and $CO_2$ during the energetic particle event (see Fig. 5.6 (d)). Subsequently, the atomic oxygen produces $O_3$ via reaction R33. The Ozone loss in the 0.1 bar 'Wet-alive' scenario between 40 and 70 km is likely due to $NO_x$ and $HO_x$ catalytic cycles (R36–R41), which is comparable to Earth. For the 'dead' scenarios (blue and red), the alternating $O_3$ formation and depletion between 40 and 70 km can be explained by enhanced production of atomic oxygen (O) during the particle event (Fig. 5.6 d). Since both atmospheric cases show production of O, overall $O_3$ formation or depletion is determined by the initial values of $O_2$. They are higher for the 'Dry-dead' cases, which lead to $O_3$ formation compared to the 'Wet-dead' scenarios.

Grenfell et al. (2013) and Herbst et al. (2024) mention that for M-stars, the ozone production via the so-called smog mechanism is more important compared to the Chapman mechanism on Earth due to the lower UV flux of M-stars. This mechanism is shown in reactions R66–R71.

$$\mathrm{CO + OH \longrightarrow CO_2 + H} \tag{R66}$$

$$\mathrm{H + O_2 + M \longrightarrow HO_2 + M} \tag{R67}$$

$$\mathrm{NO + HO_2 \longrightarrow NO_2 + OH} \tag{R68}$$

$$\mathrm{NO_2 + h\nu \longrightarrow NO + O} \tag{R69}$$

$$\mathrm{O + O_2 + M \longrightarrow O_3 + M} \tag{R70}$$

$$\textbf{net: } \mathrm{CO + 2\,O_2 \longrightarrow CO_2 + O_3} \tag{R71}$$

$NO_2$ is photolyzed in the visible and releases atomic oxygen (O) for ozone formation via R33, which is more efficient for M-stars than photolysis of $O_2$ (Grenfell et al., 2013). Thus, less O is also available to enable $NO_x$ catalytic ozone loss like on Earth (Lary, 1997). Whether ozone loss or production dominates below ~40 km is determined by the availability of $HO_x$ and $NO_x$. In the 'Wet-alive' 0.1 bar $CO_2$ case, more $NO_x$ favors reaction R68 and enables ozone production via the smog mechanism. This is in agreement with Grenfell et al. (2007), which suggests $O_3$ production via smog mechanism, stimulated by enhanced $NO_x$ during particle precipitation. For the 'Wet-alive' 1 bar $CO_2$ scenario, the smog mechanism between 20 and 40 km is limited due to lower values of $NO_x$, and the higher amount of $O_3$ (see Fig. 5.3) in this region favors reaction R39, leading to ozone loss, rather than ozone production. In the 'dead' scenarios with less initial $O_3$ in the lower atmosphere (below ~20 km), reaction R39 is limited and the $O_3$ production via R33 exceeds the loss. More initial $O_2$ in the 'Dry-dead' scenario (blue lines in Fig. 5.6) leads to enhanced $O_3$ production up

to ~20 km compared to the 'Wet-dead' case (red lines in Fig. 5.6). Lower $NO_x$ and $O_2$ for the 'Wet-dead' 1 bar $CO_2$ scenario (red dashed-dotted) suppress the smog mechanism and lead to ozone loss right from the ground upwards. Between 20 and 40 km, the $O_3$ loss within the 'Dry-dead' scenarios is most likely due to enhanced $O_3$ peak, which favors in combination with more NO (Fig. 5.6 (e)) reaction R39 and exceeds $O_3$ formation via the smog mechanism. In general, the ozone budget is quite complex and depends strongly on the atmospheric conditions.

The $N_2O$ production in the 'Wet-alive' scenarios corresponds to ozone loss between 40 and 70 km. Less ozone provides less $O(^1D)$ via the photolysis reaction R34. Thus, the destruction of nitrous oxide by reaction with $O(^1D)$ is slower. In general, the formation of $N_2O$ is small (less than a ppt nearly everywhere) within the version without abiotic $N_2O$ production.

### 5.1.3 Multiple Ionizatios Events

Compared to the previous section with the single ionization event, this section focuses on the evaluation of model runs with multiple ionization events. For reasons of clarity, the TRAPPIST-1e atmosphere most similar to Earth, with 0.1 bar of $CO_2$, is shown in the following. The ExoTIC model runs are started with the parameters and input profiles described in section 5.1.1. In order to account for the multiple flares of TRAPPIST-1, nine different-sized Carrington-like events are used in this work. Vida et al. (2017) suggests that the flare frequency of TRAPPIST-1 is one Carrington-like event every ~50 (Earth) days. This results in a Carrington-like event at the beginning and end of a 1200 hours long model run. The first one starts in the $24^{th}$ model hour and the last one at the beginning of day 48. In between, there is a medium-sized event (0.1 x Carrington-like), surrounded by three small events (0.01 x Carrington-like) on either side. The interval between the events after the first one is held to 144 model hours. As in chapter 4, ExoTIC performs 20 chemical timesteps per model hour and additionally calls the ion-chemistry routine during the actual event in every 2nd timestep. Here, the newest version of ExoTIC with all changes discussed in chapters 2 and 3 is used.

The frequency of the particle events is indicated in Figure 5.7 within a time series of the water vapor mixing ratio for the three atmospheric scenarios 'Dry-dead', 'Wet-dead' and 'Wet-alive'. The strong and medium-sized events are highlighted by the black arrows. In all scenarios, there is a significant reduction in the water vapor mixing ratio after each event between 40 and ~50 km. The decrease in the water vapor content is much stronger for the strong and medium-sized events compared to the small events in between, especially

for case (c). The time from one event to the next is not long enough for water vapor to recover, and the values stay lower than the initial values throughout the whole model run in this altitude range.

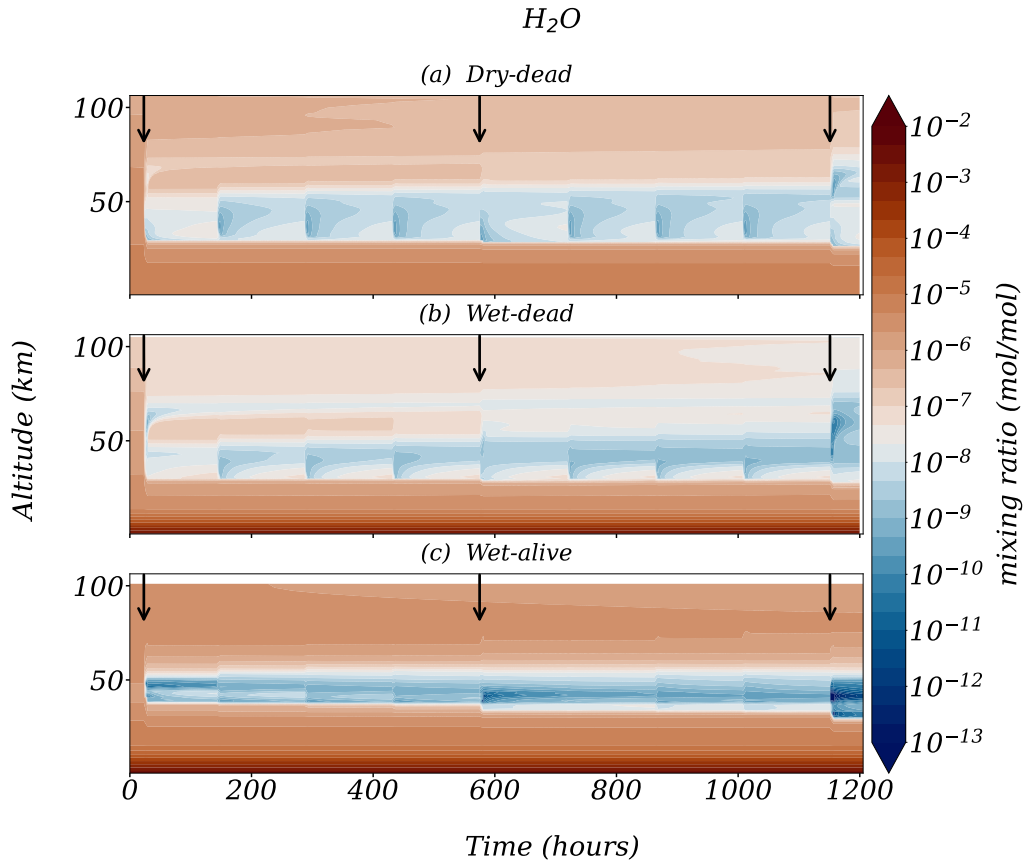


**Figure 5.7: Time series of the water vapor mixing ratio.** The figure shows a time series of the water vapor mixing ratio (mol/mol) for the three atmospheric scenarios ('Dry-dead' (a), 'Wet-dead' (b) and 'Wet-alive' (c)) including nine energetic particle events with various strength. A Carrington-like event starts after 23 and ~1150 model hours (48 days), a medium-sized event (0.1 x Carrington-like) after ~570 model hours, and the small-sized events (0.01 x Carrington-like) are in between. The start of the strong and medium-sized events are indicated by the black arrows. Each SEP event lasts for six hours.

Figures 5.8 to 5.10 show the vertical profile of the mean differences between various Carrington-like events (events 1, 5 and 9) and a corresponding reference run without particle event for several trace gases. In order to make a good comparison, the averages are taken over the same event period of six hours for all three atmospheric cases. The different scenarios chosen are indicated by the colors and the results for the different events are illustrated by the solid, dashed-dotted and dotted lines.

Regarding the different particle events in Fig. 5.8 (a), it can be seen that within a range from 20 to 80 km, the water vapor mixing ratio decreases up to ~5 ppm for all three model scenarios. With further events happening, this trend continuous and shows similar values for event nine (dotted lines). For $N_2O$ (Fig. 5.8 (c)), the positive difference in all three atmospheric scenarios indicates higher $N_2O$ values during the energetic particle event compared to the reference run. The peak values range from ~2 ppm 'Dry-dead' (blue) and 'Wet-dead' (red) scenario to ~10 ppm for the 'Wet-alive' case (green). This is many orders of magnitude higher than in the previously mentioned single ionization event, where $N_2O$ formation due to reactions R21 and R22 was not included. The positive difference increases with more particle events (dashed-dotted and dotted lines in Fig. 5.8) and results in the accumulation of $N_2O$.

For the $NO_x$ (N, NO, $NO_2$) species shown in Fig. 5.10 (a), there is an increase up to ~10 ppm between ~40 and ~70 km for all scenarios and for all events, whereby the 'Wet-alive' scenario (green) shows the largest differences. In addition, the values for the stronger events 1 and 9 are larger (solid, dotted). When examined individually, NO and $NO_2$ show alternating increase and decrease over the entire altitude range compared to the reference run (see Fig. 5.9 a+b), in particular for the 'dead' scenarios (red, blue). For the $HO_x$ (H, OH, $HO_2$) species, a similar picture emerges as for $NO_x$. There is also an increase across all scenarios, especially above ~60 km. However, the increase is slightly higher for the bigger ionization event 1 at the beginning of the multiple event model runs (solid lines in Fig. 5.10 (c).

In Figure 5.10 (b), ozone shows alternating formation and loss during the energetic particle event for all atmospheric scenarios and different event times. In the 'Wet-alive' scenario (green), there is ozone loss between 40 and 70 km, whereas below and above, ozone is formed. However, the 'Dry-dead' scenario (blue) shows almost exclusively ozone formation from 15 to ~65 km for the bigger first and last event (solid and dotted lines in Fig. 5.10 (b)). In the 'Wet-dead' case (red) for the first particle event (solid), there is small ozone formation of 0.1 ppm below 20 km and ozone loss above, except for a range of roughly 10 km around an altitude of 40 km. This changes after several events and leads to an ozone loss below 40 km and ozone formation from 40 to ~75 km (dashed-dotted and dotted line in Fig. 5.10).

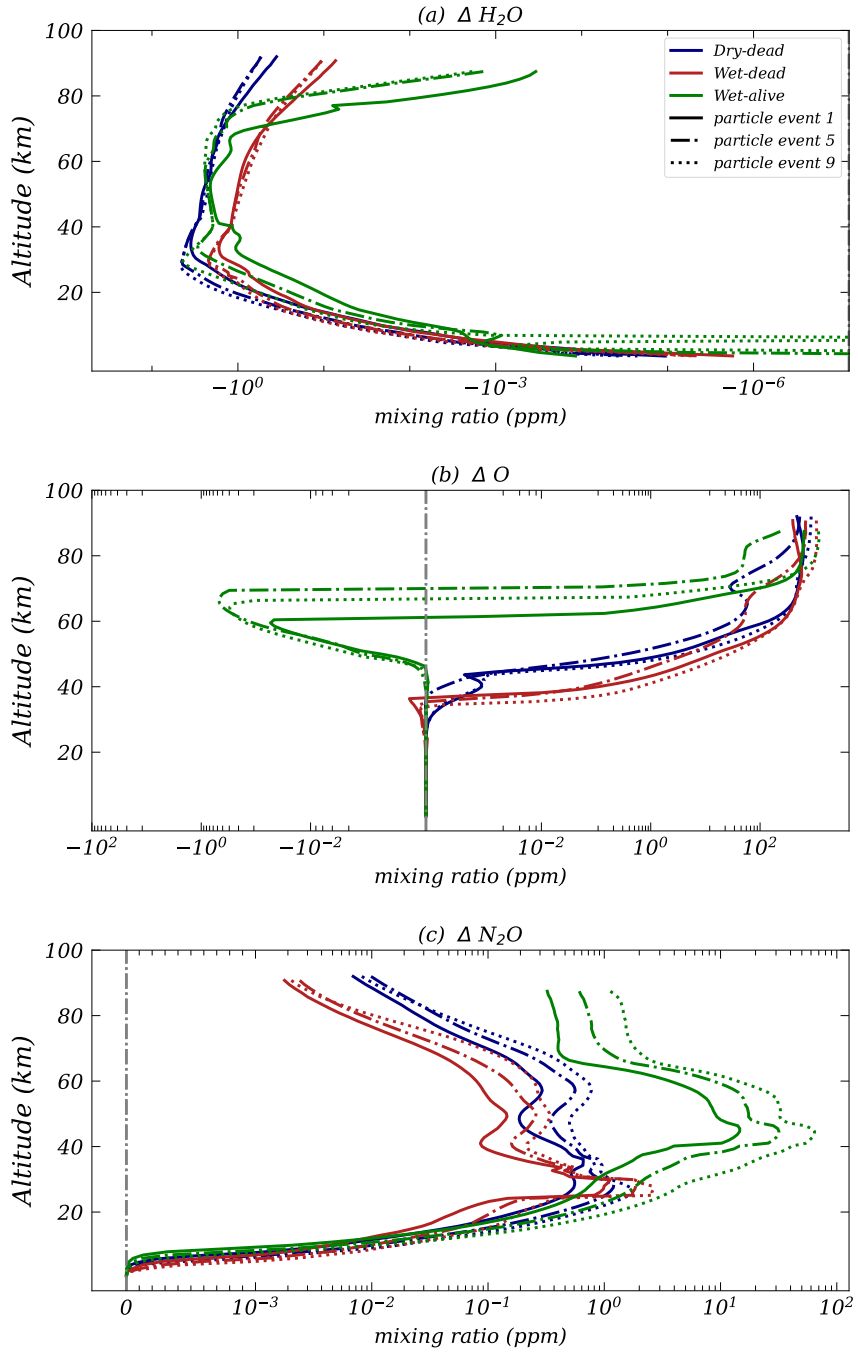


**Figure 5.8: Mean absolute differences in the mixing ratio of $H_2O$, O and $N_2O$ for TRAPPIST-1e during three energetic particle events.** The figure shows the mean difference in the mixing ratio of $H_2O$, O and $N_2O$ for TRAPPIST-1e during the 1st (solid lines), 5th (dashed-dotted) and 9th (dotted) particle event with respect to the corresponding reference run without particle event. The colored curves indicate the different atmospheric scenarios ('Dry-dead' (blue), 'Wet-dead' (red) and 'Wet-alive' (green)).

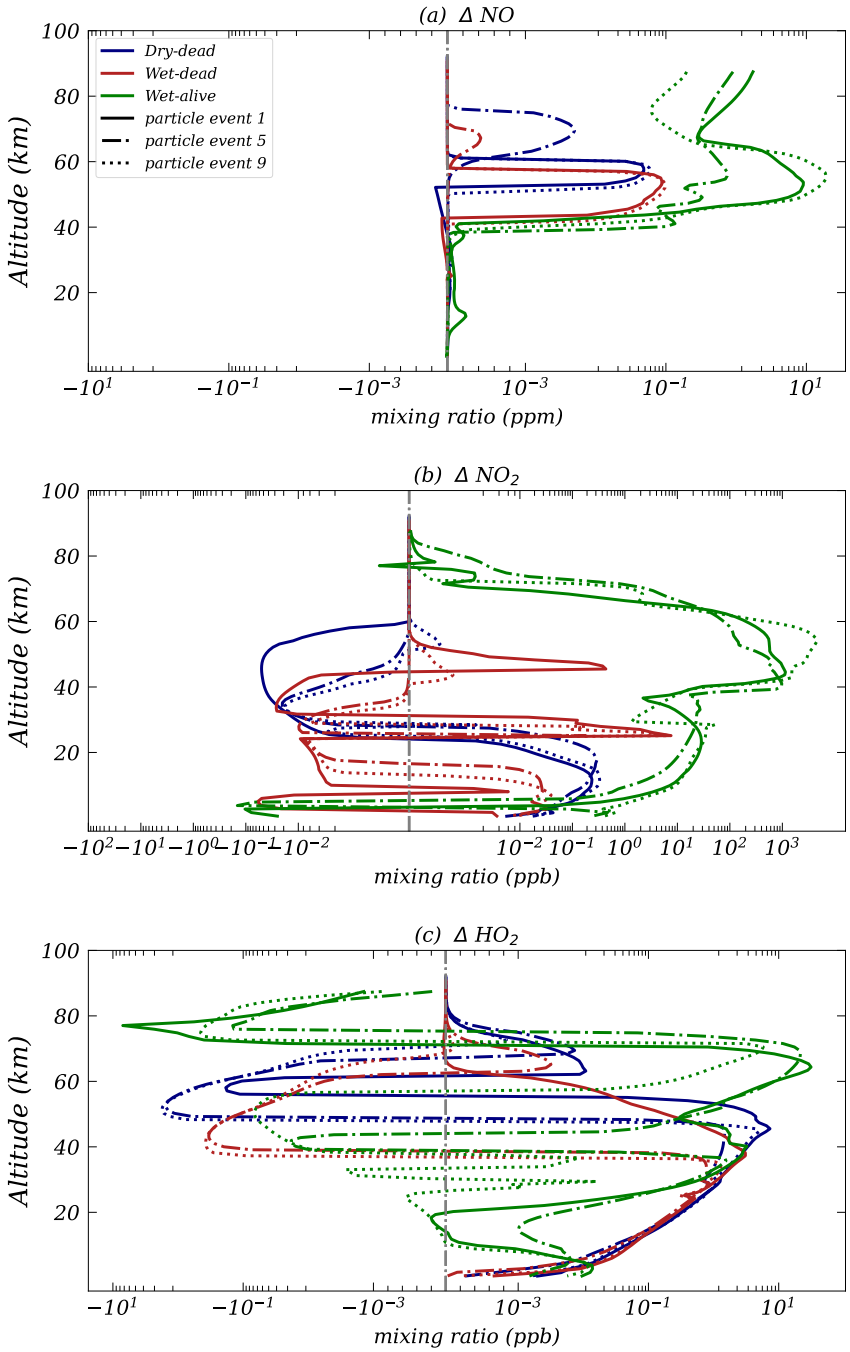


**Figure 5.9: Mean absolute differences in the mixing ratio of NO, $NO_2$ and $HO_2$ for TRAPPIST-1e during three particle events.** Same analysis as in Fig. 5.8, but notice the slightly different x-axis.

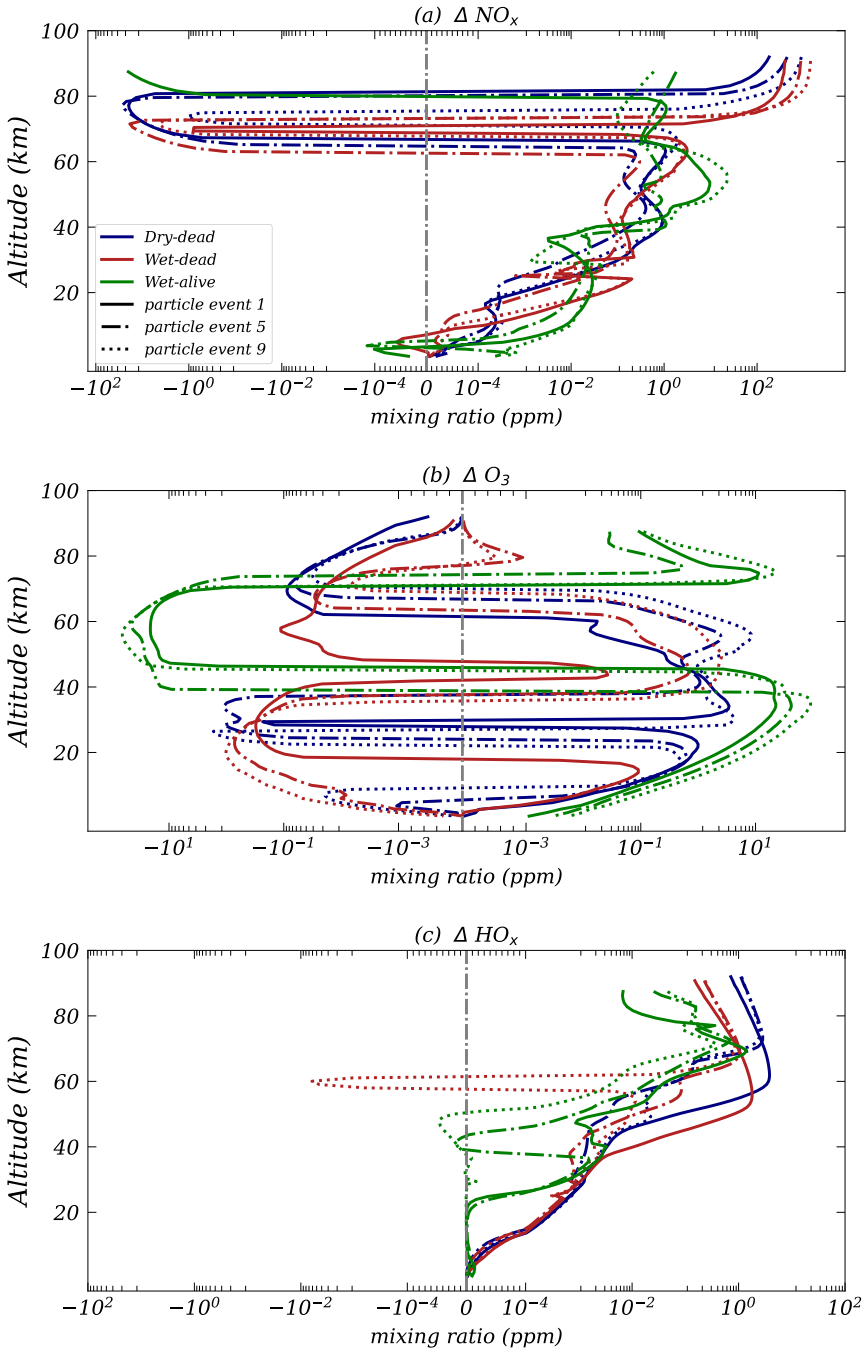


**Figure 5.10: Mean absolute differences in the mixing ratio of $NO_x$, $O_3$ and $HO_x$ for TRAPPIST-1e during three particle events.** Same analysis as in Fig. 5.8, but notice the slightly different x-axis.

The loss of water vapor (Fig. 5.8 (a)) during energetic particle events can be explained by the formation of water cluster ions (see sec. 2.3.1). These clusters release $HO_x$ species and lead to their enhancement in particular above 60 km (panel (c) of Figure 5.10) (Solomon et al., 1981). As with $HO_x$, the $NO_x$ (N, NO, $NO_2$) species are increasing during the particle events for all atmospheric scenarios below ~75 km, which is caused by the ionization and dissociative ionization of $N_2$ (Sinnhuber et al., 2012) in nitrogen-dominated atmospheres. The bigger ionization events lead to higher amounts of $NO_x$ due to higher ionization rates. This explains the differences between the big particle event (solid) and the medium-sized event (dashed-dotted).

As mentioned in chapter 2, the formation of $N_2O$ by charged particles (Zipf & Prasad, 1980) could play an important role, especially in $N_2$-dominated atmospheres. The similarly high amount of $N_2$ in the TRAPPIST-1e model scenarios compared to Earth leads to the abiotic production of 1 to ~70 ppm $N_2O$ in the middle atmosphere between 25 and 60 km. There, $N_2O$ is clearly enhanced compared to the model runs with single ionization event (see sec. 5.1.2). The amount of $N_2O$ is even higher for the 'Wet-alive' scenario compared to the 'dead' ones. There is more available $O_2$ for forming $N_2O$ out of the excited state of $N_2$ ($N_2(A^3\Sigma_u^+)$). $N_2O$ is photolyzed at wavelengths $\lambda$ < 170–240 nm (Selwyn et al., 1977). The stellar flux in that wavelength range is smaller for M-dwarf stars compared to Sun-like G-stars. Thus, the depletion of $N_2O$ is smaller, and it can accumulate in atmospheres around M-stars with a high flaring frequency. It should be noted here that ExoTIC does not have vertical transport and therefore accumulation could be locally overestimated, especially if the duration between events exceeds the vertical mixing timescale. In Sanchez-Lavega (2010), the eddy diffusion timescale is given by $\tau = H^2/D_{eddy}$ with scale height H and eddy diffusion coefficient $D_{eddy}$. For TRAPPIST-1e, Wunderlich et al. (2020) suggest that $D_{eddy} = 10^4 - 10^5$ $cm^2/s$ between 40 and 50 km, where $N_2O$ for example has its peak. Then the vertical mixing time scales are similar or higher than the frequency of the 1 x Carrington-like events. Thus, the vertical mixing should have minor effects.

Starting with the 'Wet-alive' scenario (green), the ozone formation above 70 km during all events is likely initiated by reaction R33, after prior dissociation of mainly $O_2$ due to the high amount of oxygen and smaller $HO_x$ formation. This is consistent with the findings in Herbst et al. (2024) and is also illustrated in the increase of atomic oxygen shown in Fig. 5.8 (b). Initial ozone peaks for the 'Wet-alive' scenario between 40 and 60 km. Hence, $O_3$ loss is due to the additional formation of $HO_x$ and $NO_x$ during the particle event, which enables the catalytic ozone loss cycles (R36–R38, R39–R41). As already explained for the single ionization event (section 5.1.2), below 40 km (Fig. 5.10, (b)), enhanced $NO_x$ during the

particle event enables the smog-mechanism (R66–R71), which results in ozone formation, rather than $O_3$ depletion.

The ozone formation within the first 20 km of the 'Dry-dead' case could be also referred to the smog mechanism (blue lines in Fig. 5.10 (b)). Although the $O_2$ content of the atmosphere is significantly lower than in the 'Wet-alive' scenario, $O_3$ formation is still sufficient to produce a surplus. Above ~40 km, atomic oxygen is produced likely from $CO_2$ dissociation during the particle event, since the initial $O_2$ values are even smaller compared to the 'Wet-alive' scenario. This additional O initiates formation of $O_3$ via R33, which exceeds the destruction by the $HO_x$ and $NO_x$ catalytic cycles. Above ~60 km, the higher amount of $HO_x$ surpasses the Ozone production and leads to $O_3$ depletion. The situation is similar for the 'Wet-dead' scenario (red lines in Fig. 5.10), whereby $O_3$ loss below 40 km dominates after several events. The initial $O_2$ in that altitude range is at least one order of magnitude lower compared to the 'Dry-dead' scenario. Thus, the smog mechanism is not sufficient anymore, which leads to overall $O_3$ depletion. Between ~40 to ~70 km, $HO_x$ decreases with further events and weakens the $O_3$ depletion via the $HO_x$ catalytic cycle. Hence, $O_3$ production via R33 again exceeds depletion. Above ~75 km, the higher production of $HO_x$ compared to the 'Wet-alive' scenario, leads to $O_3$ depletion in both 'dead' scenarios despite higher $CO_2$ and $O_2$ dissociation. In summary, it can be said that the results for the first particle event of the multiple event model runs with the new chemistry setup correspond well with the findings of Herbst et al. (2024). The newly implemented abiotic production of $N_2O$ causes significantly higher values compared to the older model version of the single ionization event (section 5.1.2) and shows accumulation after several energetic particle events.

#### Consequences for the Transmission Spectra

In this section, the influence of the changes of atmospheric trace gases presented in the previous subsection on transmission spectra as measured, e.g., by MIRI or NIRSPEC on the James Webb Space Telescope, are discussed by comparing two model runs with and without (reference) energetic particle events.

In our distributed project work, the spectral data have been calculated by Ben Taysum (DLR) using GARLIC (see 3.2.3) at a resolving power of 300 and have been visualised here to suite the objectives of the investigation. Figures 5.11 – 5.13 show the simulated transmission spectra (see 2.4.1) of the three atmospheric cases with and without energetic particles (upper panels) for the ionization events 1, 5 and 9. The lower panel of these figures illustrates the corresponding relative change within the transit depth in %.

Important absorption bands are $CO_2$ (4.3 $\mu$m), $H_2O$ (4.9–7.7 $\mu$m), $CH_4$ (5.8–9.2 $\mu$m), NO (5–5.7 $\mu$m), $NO_2$ (6–6.4 $\mu$m) and $O_3$ (8.1–10.4 $\mu$m) (Herbst et al., 2024). Furthermore, $N_2O$ has bigger absorption bands at 3.9 $\mu$m and 8.6 $\mu$m (Quanz, S. P. et al., 2022a). All scenarios show the prominent $CO_2$ feature due to the initial high $CO_2$ concentration and after several ionization events, there is no significant change compared to the reference run. In contrast, the transit depth in the most prominent water absorption band (4.9–7.7 $\mu$m) is reduced by about 0.25% (0.5%) for the two 'dead' scenarios during the first (last) particle event, which is consistent with the differences shown in Fig. 5.8 (a).

The 'Wet-alive' scenario shows peaks at the NO and $NO_2$ absorption bands masking the decrease in the water prominent band around 6 $\mu$m. During the last big ionization event nine (Fig. 5.13), the relative difference in the transit depth of the NO and $NO_2$ peak is bigger compared to the earlier events. This corresponds as well with the absolute differences shown in Fig. 5.9 (a+b). For both species, there is an increase up to ~10 ppm above an altitude of 50 km, where the observations are quite sensitive.

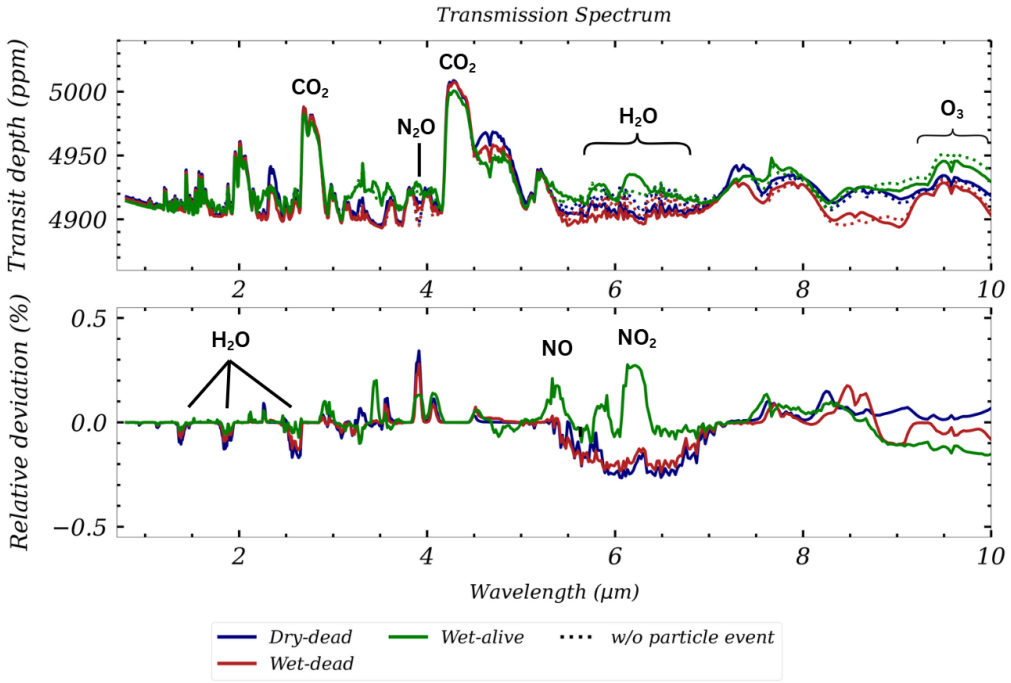


**Figure 5.11: Simulated transmission spectra for TRAPPIST-1e during the first ionization event.** The upper panel of this figure shows the simulated transmission spectrum (ppm) for the TRAPPIST-1e model runs, 'Dry-dead' (blue), 'Wet-dead' (red) and 'Wet-alive' (green) and the corresponding reference runs without particle event (dotted lines). The lower panel shows the relative deviation of the transit depth (%) for the model scenarios. The data for the transmission spectra were calculated with GARLIC at DLR using the output from the ExoTIC model runs at KIT. Subsequently, the results were visualised in the figure above and in the figures 5.12–5.13 to highlight the scenario differences.

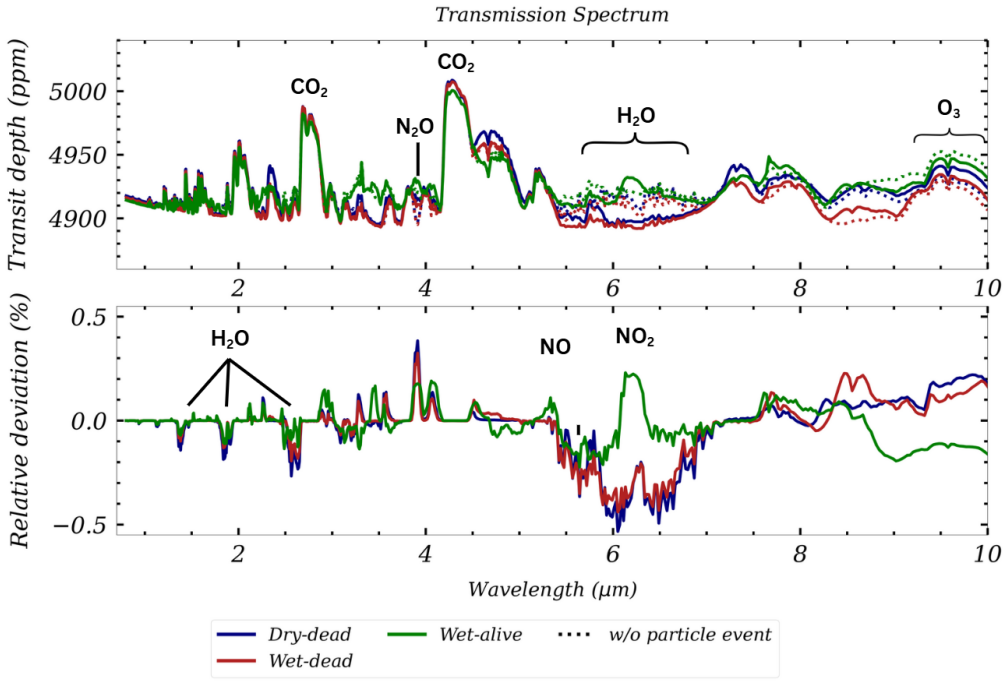


**Figure 5.12: Simulated transmission spectra for TRAPPIST-1e during the 5$^{th}$ ionization event.** Same as Fig. 5.11, but for the 5$^{th}$ ionization event.

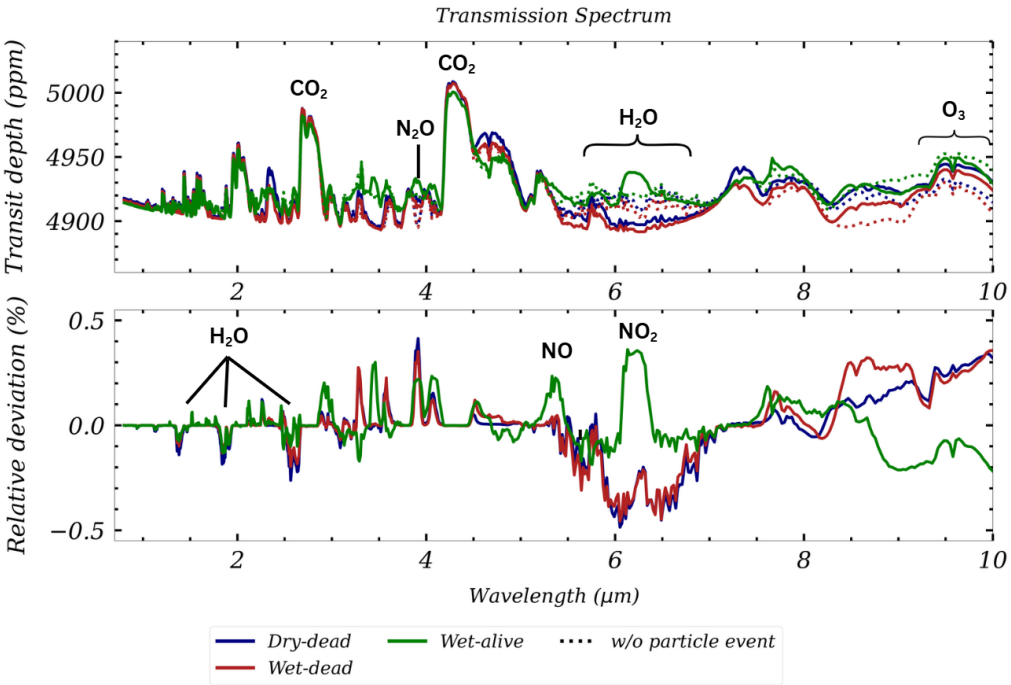


**Figure 5.13: Simulated transmission spectra for TRAPPIST-1e during the 9$^{th}$ ionization event.** Same as Fig. 5.11, but for the 9$^{th}$ ionization event.

Regarding $N_2O$, there is a clearly relative difference in the absorption line around 3.9 $\mu$m for all three atmospheric scenarios (Fig. 5.11–5.13) compared to the model runs without particle event. The relative changes in the transit depth are bigger for the 'dead' scenario in contrast to the 'alive' scenario. With an increasing number of particle events, these changes increase up to 0.45%, which is consistent with the modeled absolute accumulation of $N_2O$ over time. At 8.6 $\mu$m the changes are less prominent due to the overlapping features of $O_3$ and $CH_4$, which contribute to the total absorption. Because of higher initial concentrations and biogenic fluxes, the overall peak of $N_2O$ in the transit depth is higher for the 'alive' scenarios compared to the 'dead' ones (upper panel of Figs. 5.11–5.13). Thus, the additional produced $N_2O$ during energetic particle events has a much smaller contribution to the total absorption, because the band is more saturated.

Within the Ozone absorption band around 9.6 $\mu$m, the 'alive' scenario shows a relative decrease up to ~0.25%, which corresponds to the absolute decrease in Ozone between 40 and ~75 km (Fig. 5.10 (b)). For the other two scenarios (blue, red), the ozone transit depth changes up to 0.25% throughout the several events due to additional $O_3$ formation above ~45 km (Fig. 5.10 (b), dashed-dotted and dotted lines).

In the peer-reviewed study of Herbst et al. (2024), to which this doctoral thesis contributed, the model runs performed with ExoTIC did not take into account the abiotic production of $N_2O$ and only considered a single particle event. Except for the enhancement of $N_2O$ in all model runs and the enhancement of $O_3$ in some model runs during the particle event, the changes in the atmospheric composition for the other trace gases and therefore the variation in the transmission spectra are comparable. Additional $N_2O$ influences the $NO_x$ budget, and ozone is quite sensitive to it, which could explain the differences in the 'dead' scenarios compared to Herbst et al. (2024). Compared to a single particle event, several events show a continuous impact on the atmospheric composition without strong atmospheric relaxation between the particle events. As previously mentioned, frequent events can accumulate $N_2O$.

In general, this work shows that energetic particle events lead to significant changes in the atmospheric composition of $N_2$-dominated atmospheres on planets orbiting M-dwarf stars. The abiotic production of $N_2O$ leads to differences of about 0.45%, which is approximately 15–25 ppm in the absolute transit depth. Figure 5.14 shows a comparison between measured and simulated transit depth (ppm) for TRAPPIST-1e. The measured data points (black) are taken from Espinoza et al. (2025) and represent a single transit event of TRAPPIST-1e, measured on June 22, 2023. There, the authors suggest that the measurements are contaminated due to the high stellar activity of TRAPPIST-1.

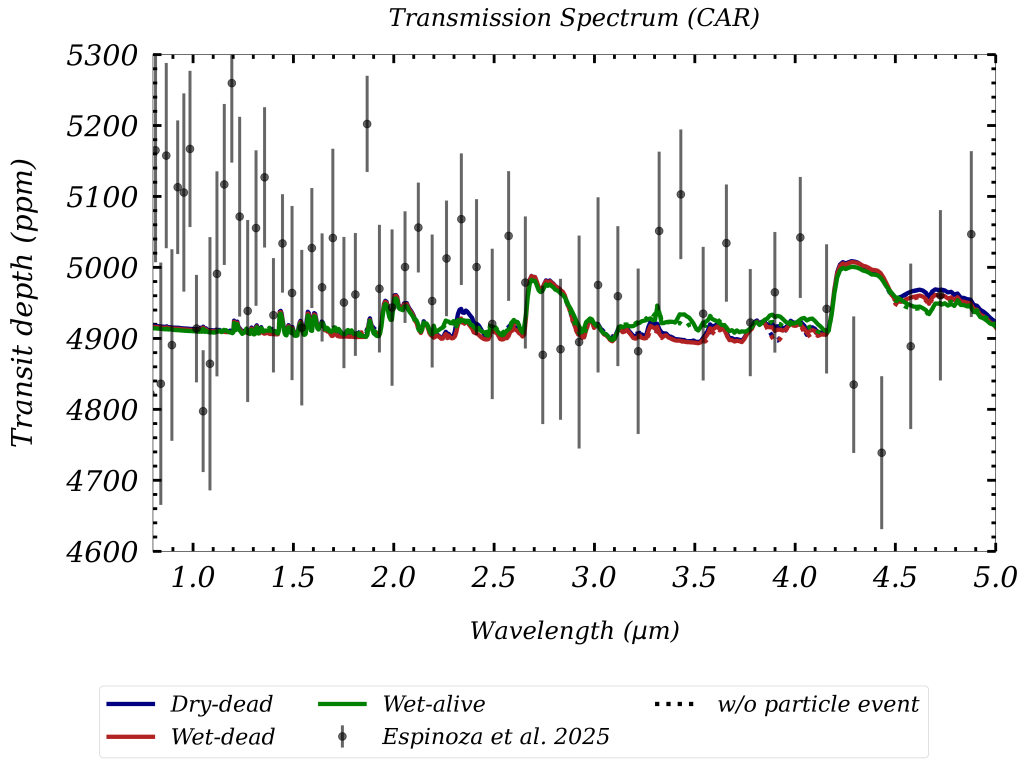


**Figure 5.14: Comparison of simulated and measured transmission spectra for TRAPPIST-1e.** The figure shows a comparison between the measured transmission spectrum (black data points) for one transit, which was published in Espinoza et al. (2025) and obtained on June 22, 2023 and the simulated transmission spectra for the different atmospheric scenarios with (solid lines) and without (dotted lines) particle event. The simulated spectrum was taken from figure 5.13 (upper panel) and plotted within the wavelength range of the measurements. Due to the large variation of the data points, the reference run is a little bit masked.

According to Leleu et al. (2021), the signal-to-noise ratio S/N is given by equation 5.1

$$\frac{S}{N} = \sqrt{n} \cdot \frac{TD}{\sigma}, \tag{5.1}$$

with transit depth TD, number of transits $n$ and measurement noise $\sigma$. In figure 5.14, the mean measurement noise of the data between 1 and 5 $\mu$m is ~100 ppm. In an optimistic case, one need at least 16 transit observations to reach a relevant S/N of $1\sigma$, in order to detect changes in $N_2O$ of ~25 ppm. Better would be $2\sigma$ ($3\sigma$) or more, which require 64 (144) or more transits. The detection of larger features like $CO_2$ is easier due to a higher signal. Hence, it needs more transits and more precise measurements in the future to improve the current data basis. Then, the abiotic formation of $N_2O$ could be misinterpreted as a biosignature of an exoplanet if the activity of the host star is not considered. Thus, it is recommended to include the impact of stellar energetic particles in the analysis methods.

## 5.2 LHS 1140 b – Planet orbiting an inactive M-dwarf Star

Dittmann et al. (2017) reported the detection of two planets orbiting a cool M-dwarf star, named LHS 1140, which were found using the transit method by the MEarth telescopes in Arizona (USA) and Chile. They are referred to as LHS 1140 b and c, with the focus on planet b in this section. The host star is classified in spectral class M4.5 and the system is localized at a distance of 14.993 pc from Earth (Gaia Collaboration et al., 2018). An overview of the main physical properties of LHS 1140 (b) is given in Table 5.3. Like TRAPPIST-1e, it is located in the habitable zone of its host star, but with a radius of approximately two Earth radii and a mass of almost six Earth masses, it is significantly larger and heavier. This opens up the possibility that its atmosphere could be more robust and possibly contain larger amounts of lighter trace gases such as $H_2$. The model setup is discussed in more detail in the following sections.

**Table 5.3: Overview of the physical parameters for the LHS 1140 system.** This table shows the physical parameters of the LHS 1140 (b) system. The planet LHS 1140 b is a super-Earth in the habitable zone of LHS 1140 (Wunderlich et al., 2021). The same values for day and year indicate the most likely tidally locked character.

| Parameter | Value[a] |
|---|---|
| Stellar Mass ($M_\odot$) | $0.184 \cdot M_\odot$ |
| Stellar Radius ($R_\odot$) | $0.2159 \cdot R_\odot$ |
| Stellar Temperature (K) | 3096 |
| Length of Day (Earth days) | 24.73 |
| Length of Year (Earth days) | 24.73 |
| Planet Mass ($M_\oplus$) | $5.6 \cdot M_\oplus$ |
| Planet Radius ($R_\oplus$) | $1.73 \cdot R_\oplus$ |
| Mean Surface Albedo | 0.255[b] |
| Orbital Distance (AU) | 0.096 |

[a] Cadieux et al. (2024b), [b] Wunderlich et al. (2021)

### 5.2.1 Simulation Setup

As with TRAPPIST-1e, it is also likely that LHS 1140 b is tidally locked due to the close-in orbit. Since there are no spectral data for LHS 1140 yet available, the spectral energy distribution (SED) is a synthetic combination of Proxima Centauri for the UV wavelength

range below 400 nm and the SED of GJ 1214 for the visible/NIR range. An orbital distance of 0.096 AU leads to a stellar Insolation of ~0.503 $S_\odot$ (Wunderlich et al., 2021). The stellar spectral flux of LHS 1140 is shown in figure 5.15. Compared to the cooler TRAPPIST-1, the Planck peak due to the hotter surface temperature is slightly shifted towards smaller wavelengths. ExoTIC uses this spectral flux with a constant stellar zenith angle of 60° to calculate the photolysis rates, which are then used by the photochemical module.

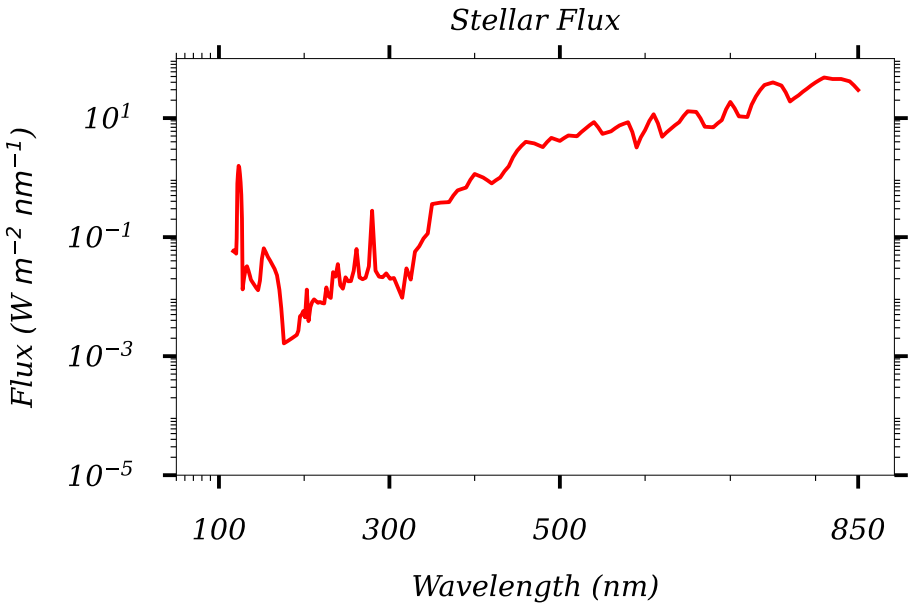


**Figure 5.15: Stellar spectral flux of LHS 1140.** Current measurements of the stellar flux of LHS 1140 are not yet available. The spectrum shown here is a synthetic combination of two different M dwarf stars - Proxima Centauri and GJ 1214, with the former spectrum used for wavelengths shorter than 400 nm and the latter for longer than 400 nm. The flux is scaled to the top of atmosphere of LHS 1140 b, which receives ~0.503 $S_\odot$ (Wunderlich et al., 2021).

### Initial Atmospheres

Observations of LHS 1140 b suggest that there is no thick $H_2$ dominated atmosphere (Damiano et al., 2024). Nevertheless, due to the large mass, it is possible that an $H_2$-dominated atmosphere may prevail, but has low surface pressure.

Compared to the atmospheres of TRAPPIST-1e, initial atmospheres with lower biogenic fluxes are used, which means lower $O_2$ content. Further, to test the influence of abiotic production of $N_2O$ within an $H_2$-dominated atmosphere, the initial amount of molecular nitrogen is enhanced. Furthermore, a recent study from Scherer et al. (2025) recommends

that LHS 1140 b receive a significant flow of atomic hydrogen originating from the outside interstellar medium (ISM) due to the small astrosphere. To investigate these different conditions regarding the impact of energetic particles, I performed ExoTIC model runs with four different starting atmospheres, which are grouped into more and less initial $N_2$ and with or without hydrogen flux in the upper atmosphere. The different model scenarios are based on initial states of atmospheric composition provided by colleagues at DLR and can be found in Table 5.4.

**Table 5.4: Overview of the used model scenarios for LHS 1140 b.** The table shows the different atmospheric scenarios for LHS 1140 b and the corresponding surface volume mixing ratios (%) of various constituents. In addition to the standard case (S), three further scenarios were calculated. One with additional hydrogen flux in the upper atmosphere (S-Heff), one with higher initial $N_2$ (S-$N_2$) and one with higher $N_2$ and hydrogen flux (S-$N_2$-Heff).

| Scenario | $CO_2$ (%) | $N_2$ (%) | $H_2$ (%) | NO (%) | $H_2O$ (%) |
|---|---|---|---|---|---|
| Standard (S) | $1.7 \times 10^{-7}$ | $5.0 \times 10^{-3}$ | 76.0 | $1.79 \times 10^{-13}$ | 4.0 |
| S-Heff | $1.7 \times 10^{-7}$ | $5.0 \times 10^{-3}$ | 76.0 | $1.78 \times 10^{-13}$ | 4.0 |
| S-$N_2$ | $1.7 \times 10^{-7}$ | 3.0 | 74.5 | $2.31 \times 10^{-9}$ | 2.4 |
| S-$N_2$-Heff | $1.7 \times 10^{-7}$ | 3.0 | 74.5 | $2.33 \times 10^{-9}$ | 2.4 |

As with TRAPPIST-1e, the atmospheric output of 1D-TERRA has 100 vertical layers, but ranging here from 0 to ~450 km. Figure 5.16 shows the full vertical profiles for different atmospheric trace gases. In both plots, $N_2$ is indicated by the solid green line. Plot (a) represents the case with less initial $N_2$, whereas plot (b) has approximately three orders of magnitude more $N_2$. It can be seen that with higher initial $N_2$ concentrations (Fig. 5.16 (b)), the $N_2O$ content is enhanced as well.

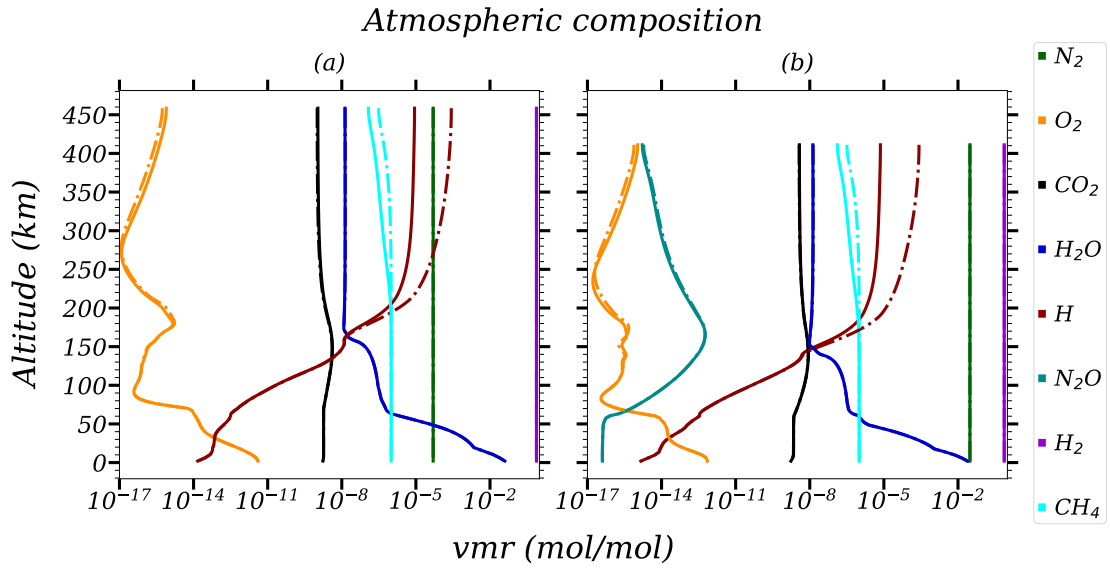


**Figure 5.16: Initial atmospheric composition of the LHS 114 b model runs.** The figure shows the vertical mixing ratio profile of various trace gases in mol/mol for atmospheric scenarios with small amount of initial $N_2$ (a) and higher amount of $N_2$ (b). The dashed-dotted lines indicate the scenarios with additional hydrogen flux in the upper atmosphere. Data were provided by DLR (same for Fig. 5.17).

The other trace gases don't show significant changes with increased $N_2$. Including hydrogen flux in the upper atmosphere (dash-dotted lines), the mixing ratio of atomic hydrogen increases for both scenarios of $N_2$. Methane (yellow) enhances as well, whereas $O_2$ (orange line) shows a small decrease.

The corresponding initial temperature profile is shown in figure 5.17, where the model runs with less initial $N_2$ are in the left plot (a) and the model runs with enhanced $N_2$ in the right plot (b). The additional hydrogen flux is indicated by different colors. Besides some fluctuations above 200 km, the are no significant changes in the temperature profile for the atmospheres with different initial $N_2$. Only the surface temperature is slightly higher in the model run with less $N_2$ (a) compared to the model run with more $N_2$. The additional hydrogen in the upper atmosphere doesn't change the temperature profile at all.

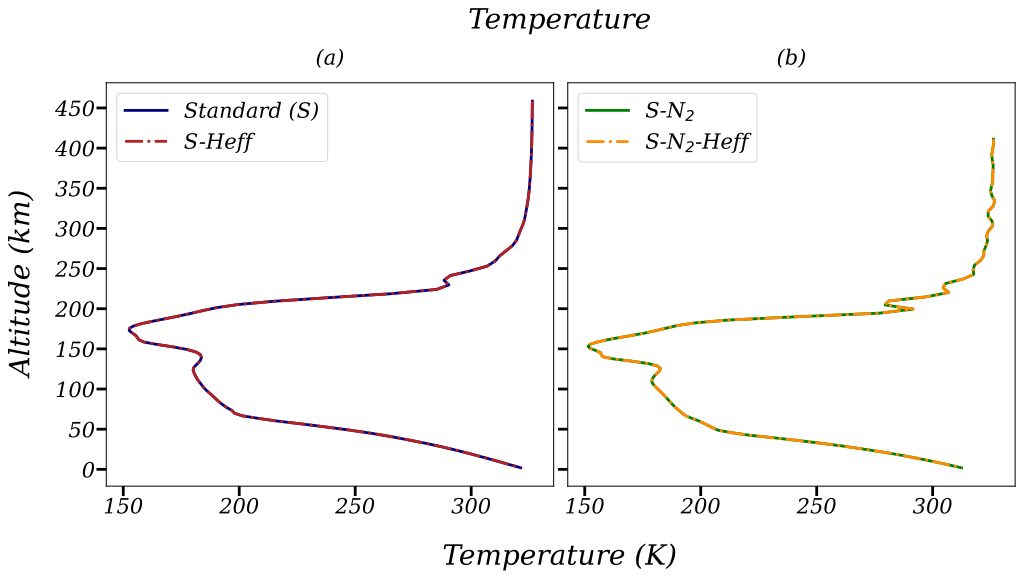


**Figure 5.17: Temperature profile for the four LHS 1140 b model simulations.** The figure shows the temperature profile for the different LHS 1140 b model runs, varying the initial $N_2$ content (a = less $N_2$, b = more $N_2$). The different colors indicate the model simulations with enhanced upper atmospheric hydrogen flux.

### Ionization Rates

As already mentioned for the previous simulations, ExoTIC uses ionization rates calculated by Konstantin Herbst (university of Kiel/Oslo) using AtRIS. The small astrosphere of LHS 1140 leads to a bigger influence of GCRs impacting the planetary atmosphere of LHS 1140 b (Herbst et al., 2020). Scherer et al. (2025) supports this bigger influence and mentions that a full 3D magneto-fluid dynamics simulation has to be made to get the whole picture of GCR flux. Figure 5.18 shows the ionization rates of the GCRs (red lines) calculated by AtRIS for the different input atmospheres (solid and dashed-dotted lines). It can be seen that the peak due to the more energetic particles arises in the lower atmosphere of LHS 1140 b. For comparison, the blue lines show Carrington-like events, which were scaled to the orbital distance of LHS 1140 b. Their peaks are higher up in the atmosphere and the effects on it are much greater. Overall, the different amount of $N_2$ in (a) and (b), as well as the possible hydrogen flux in the upper atmosphere (dashed-dotted lines), do not have a significant influence on the ionization rates.

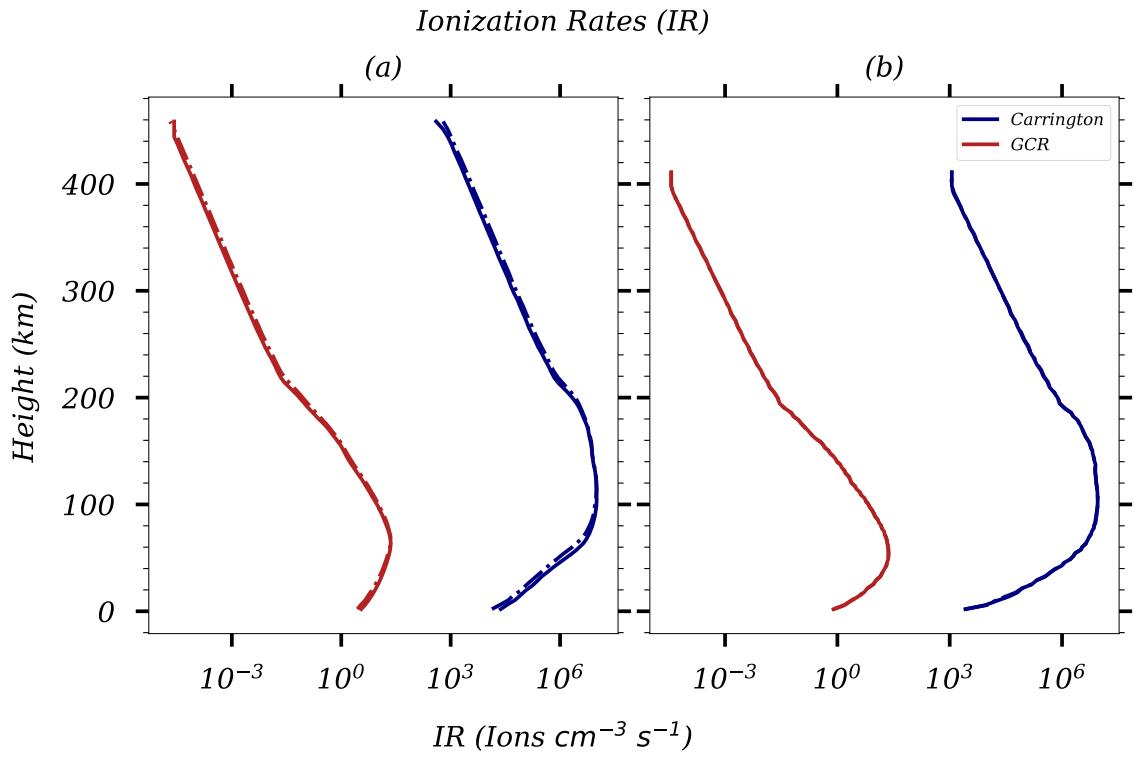


**Figure 5.18: Ion pair production rates for different input atmospheres of LHS 1140 b.** The figure shows the ion pair production rates for the two energetic particle events Carrington-like (blue) and GCR (red) with different atmospheres of LHS 1140 b. Within an $H_2$-dominated atmosphere, the initial $N_2$ content is lower in case (a) compared to the right plot (b). The dashed-dotted lines represent the atmospheres with additional hydrogen flux. Data were provided by Konstantin Herbst (Kiel/Oslo).

Even though no strong SEP events have been observed for LHS 1140 yet, they could serve in this work as a comparison for what effects one might expect in $H_2$-dominated atmospheres. In these simulations as well, the particle event starts in the $24^{\text{th}}$ model hour. The Carrington-like event lasts for six hours and the galactic cosmic ray impact lasts for 24 hours to simulate a permanent effect. For both types of particle event, ExoTIC performs 20 chemical timesteps within one model hour and calls the ion chemistry routine during the event period every $2^{\text{nd}}$ timestep. The whole output is generated after every 5th chemical timestep, which leads to a time resolution of 15 minutes. The results of the different model runs are presented in the next part.

### 5.2.2 Analysis of the Model Simulations

First, this sections starts with the results for the Carrington-like ionization event scaled to the orbital distance of LHS 1140 b in order to evaluate the impact on $H_2$-dominated atmospheres. Afterwards the same is done for the galactic cosmic ray background to account for the special small astrosphere of LHS 1140 (see previous part).

#### Hydrogen Species

Since hydrogen species become more important in $H_2$–dominated atmospheres, figure 5.19 shows the time series of the water vapor mixing ratio for a first brief overview. It includes the previous introduced model experiments (see Table 5.4) with a Carrington-like event, which is indicated by the yellow lines. All model simulations show water vapor depletion of several orders of magnitude, especially above 100 km, which is likely due to the photolysis of $H_2O$. With the beginning of the ionization event, the water vapor content slightly increases and is photolyzed again after the end of the event.

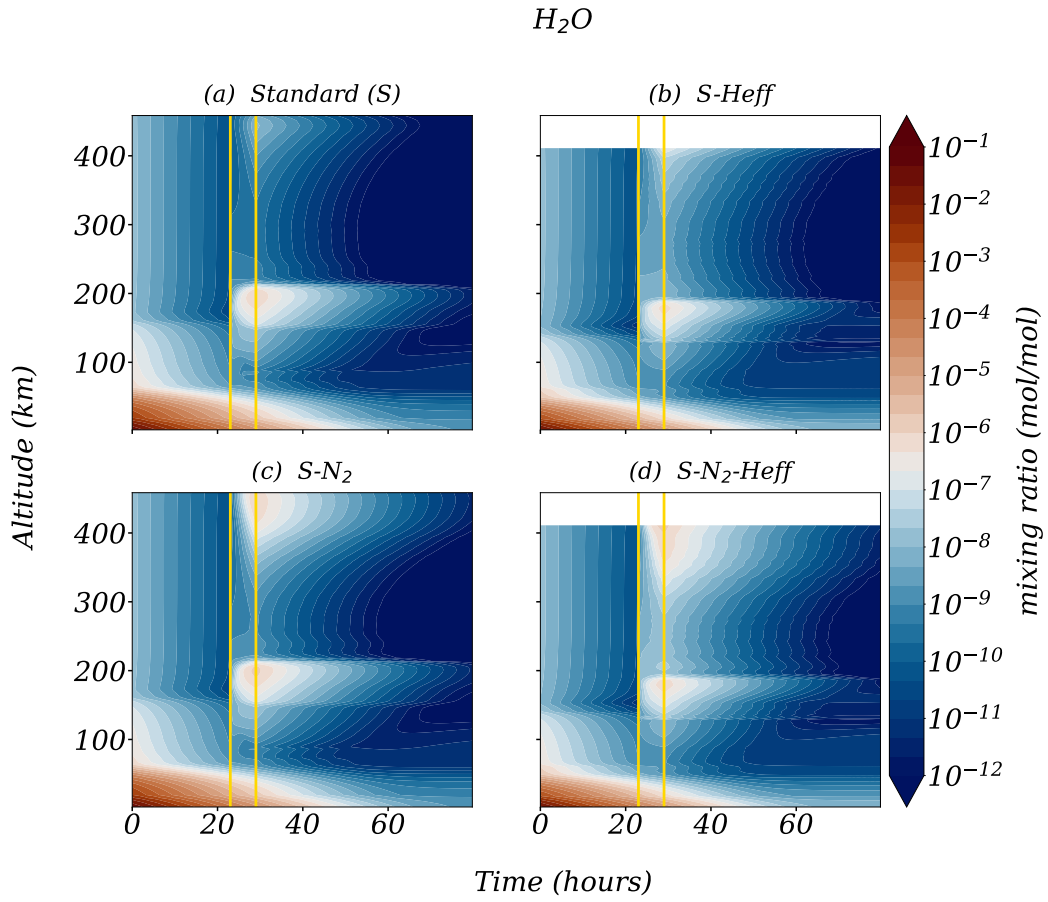


**Figure 5.19: Absolute mixing ratio of water vapor for LHS 1140 b model simulations.** The figure shows the absolute volume mixing ratio of $H_2O$ in mol/mol for the different model simulations of LHS 1140 b (Table 5.4).

This fact is also supported by the following Figure 5.20, which shows the absolute differences between various trace gases in a model run with and without ionization events averaged over the event (similar analysis as in Figs. 5.8–5.10). At an altitude of ~200 km, there is a peak in the water mixing ratio of 0.2—0.5 ppm for all four scenarios (a). This corresponds to the formation of OH (b) and the loss of $CH_4$ (g) in this altitude range during the particle events. Molecular hydrogen (c) is reduced over the entire altitude range of ~400 km compared to the reference run. It shows also a small peak at ~200 km of approximately 10 ppm.

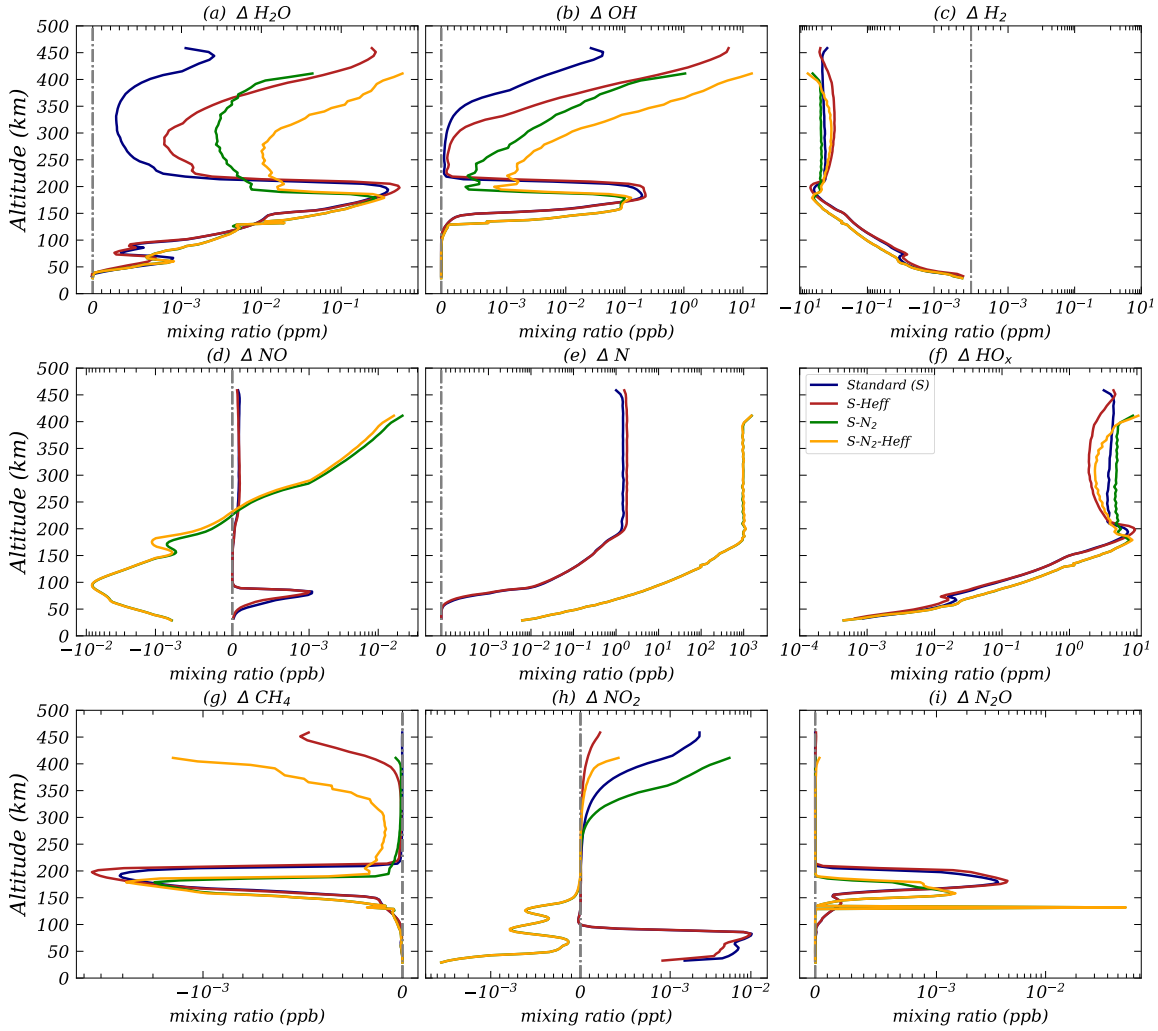


**Figure 5.20: Absolute differences in the mixing ratio of various trace gases for LHS 1140 b.** The analysis within this figure is similar to Figs. 5.8–5.10. Here, NO was replaced by $H_2$, and atomic oxygen was replaced by $CH_4$.

The Carrington-like ionization event starts peaking at around 200 km. This leads to stronger ionization, dissociative ionization and subsequent dissociation via recombination of the $H_2$-dominated atmosphere (see R51, R52 and Table 3.4). Therefore, atomic hydrogen is the dominant part within the $HO_x$ (H, OH, $HO_2$) species. In addition, oxygen and oxygen-ions are formed, which mainly originate from the ionization of $CO_2$, since the initial concentration is significantly higher compared to $O_2$. Within the denser atmosphere, which produces higher ionization rates, the ionized hydrogen molecules and oxygen ions can form $OH^+$ ions more quickly. They subsequently recombine to neutral OH and explain the OH peak at ~200 km. The produced OH is highly reactive and influences the water

vapor budget by oxidizing methane via R72, or reacting with the high amount of $H_2$ (R73). Both reactions can produce additional water vapor (Wunderlich et al., 2021).

$$CH_4 + OH \longrightarrow CH_3 + H_2O \tag{R72}$$

$$H_2 + OH \longrightarrow H_2O + H \tag{R73}$$

In the upper atmosphere above 200 km, the additional hydrogen flux increases the amount of OH and subsequently $H_2O$.

#### Nitrogen Species

In comparison to the hydrogen species, the nitrogen species show a different behavior for the simulations with less (blue and red lines) and more (green and orange lines) initial $N_2$. For NO and $NO_2$ (Fig. 5.20 d, h), there is depletion with some smaller variations from the surface up to ~200 km for the model runs with higher initial $N_2$. In contrast, the model runs with less initial $N_2$ show an increase of a few ppt for NO and $\sim 10^{-2}$ ppt for $NO_2$ below an altitude of 100 km. Regarding $N_2O$ (Fig. 5.20 (i)), the differences show a small additional production in the range of 1 to 10 ppt, whereas the difference is higher for the model runs with less initial $N_2$.

An effective loss mechanism of NO is owing to reaction R74 (Sinnhuber et al., 2012).

$$N + NO \longrightarrow N_2 + O \tag{R74}$$

In the model simulations with more initial $N_2$, the NO concentration is also higher throughout the atmosphere. With the beginning of the particle event, approximately three orders of magnitude more atomic nitrogen is formed in the scenarios with more $N_2$ (see Fig. 5.20 (e)). In the denser atmosphere below ~200 km, the combination of higher N and NO enhances the loss mechanism (R74) and lead to a fast exponential decay of NO due to the reaction kinetics. This is illustrated in Figures 5.21 and 5.22 for the scenarios with less $N_2$ ('Standard') and higher initial $N_2$ ('S-$N_2$'), which show the reaction rate for different NO depleting reactions. Here, the dominant reactions with the highest reaction rates are the photolysis reaction (e) and R74 (c), while the rest can be neglected, since the rates are order of magnitudes smaller.

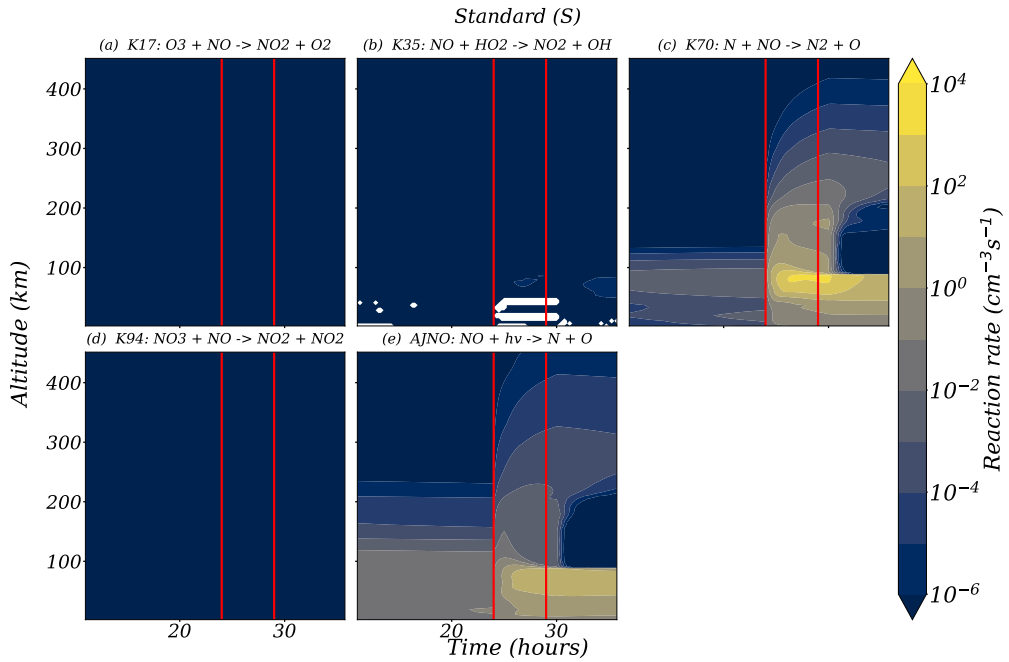


**Figure 5.21: Reaction rates of different NO reactions for the scenario with less initial $N_2$.** The figure shows the reaction rates of various NO-depleting reactions over time for the model scenario with less initial $N_2$. The particle event starts within the $24^{th}$ hour and lasts six hours (red vertical lines). The white artifacts are likely due to numerical issues at higher pressure.

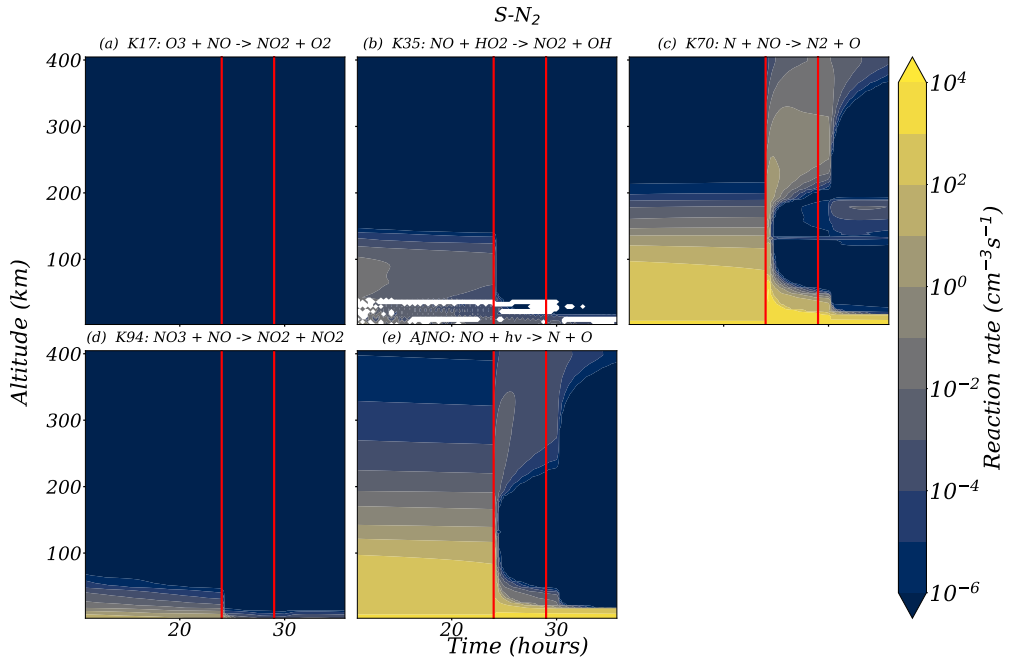


**Figure 5.22: Reaction rates of different NO reactions for the scenario with higher initial $N_2$.** Same as Fig. 5.21.

Right after the start of the particle event, the reaction rate of R74 is higher in Fig. 5.22 (c) compared to the scenario with lower initial $N_2$ (Fig. 5.21 (c)). Above ~200 km, the atmosphere becomes less dense, which weakens the depletion mechanism due to less probable particle collisions. Thus, the production of NO gains more importance and exceeds the production for the $N_2$-poor scenarios. In addition, less NO also means less $NO_2$. During the particle event, $N_2O$ is produced in an amount of up to several ppt in all scenarios (Fig. 5.20 (i)). Despite less $N_2$ and apart from a few layers, more $N_2O$ is produced (blue, red lines in Fig. 5.20 (i)). Wunderlich et al. (2021) suggests that the occurrence of OH can enhance molecular oxygen. In combination with the lower amount of $NO_2$, the $N_2O$ production due to the abiotic mechanism (R21–R24) is smaller within the scenarios with lower initial $N_2$. However, the $N_2O$ concentration of a few ppt is small compared to strongly $N_2$-dominated atmospheres in both cases.

As mentioned above, LHS 1140 b has a small astrosphere, and therefore GCRs, strongly contribute to the stellar energetic particles. The impact of GCR ionization is shown in Figure 5.23, showing a different picture compared to the stronger Carrington-like event. The changes are order of magnitudes smaller. Water vapor, for instance, shows alternating destruction and formation occurs up to an altitude of approximately 200 km (see Fig. 5.23 (a)). Above, there is mainly $H_2O$ production, which can be attributed to the enhanced OH. Since, the ionization rates for galactic cosmic rays are quite small, the amount of produced $H_2$/H-ions is not sufficient to compensate for the water loss due to ionization. The behavior of nitrogen compounds is similar to that observed in a Carrington-type event. Here, a decrease in NO and $NO_2$ can be observed in scenarios with a lower initial amount of $N_2$ as well. As explained above this could be assigned to the loss mechanism R74. All in all, the changes are very small, which implies that GCRs should be simulated over longer timescales. Thus, it is necessary to include the climate-chemistry model 1D-TERRA into the model chain.

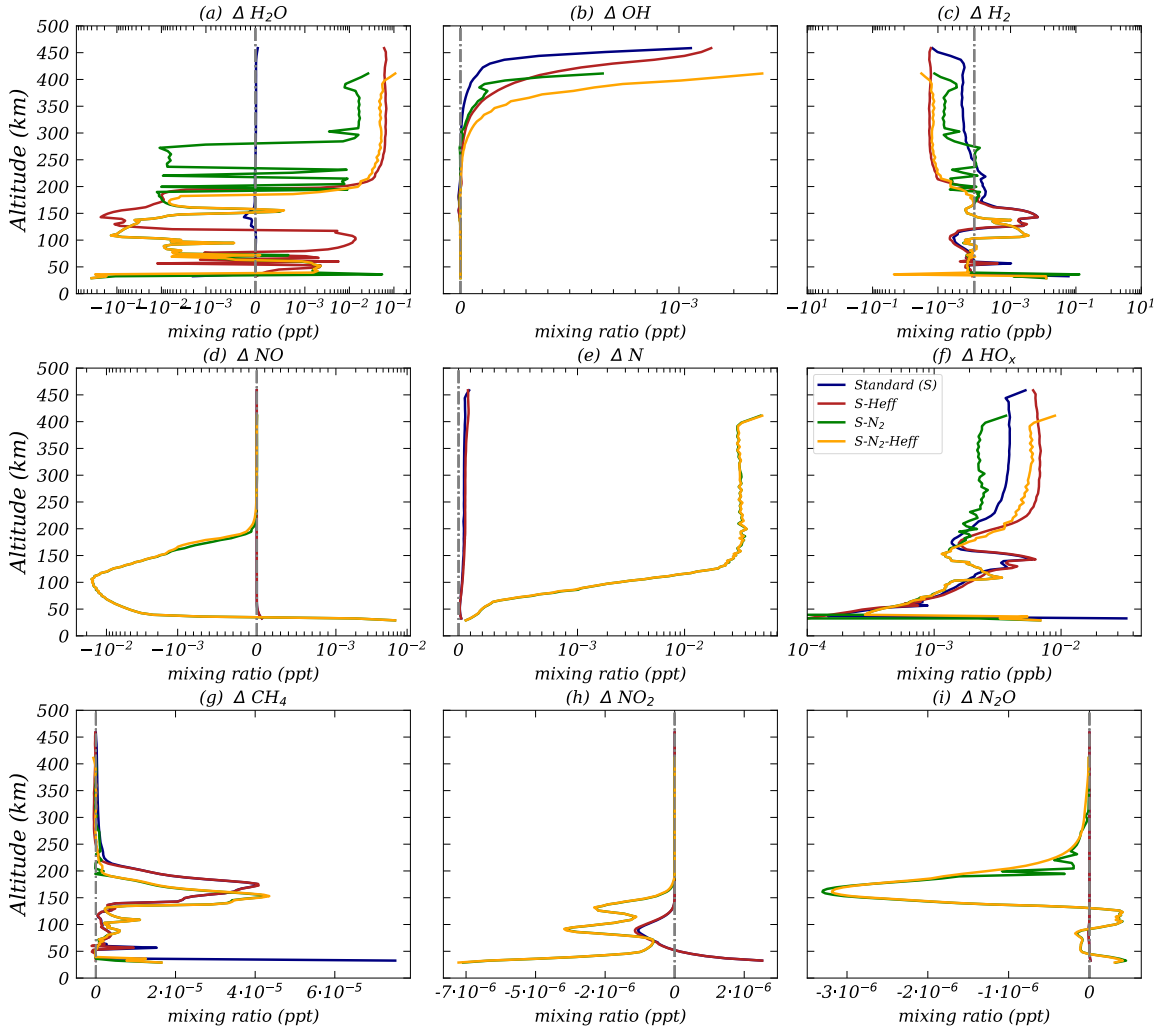


**Figure 5.23: Absolute differences in the mixing ratio of various trace gases for LHS 1140 b.** The figure is similar to Fig. 5.20, but for galactic cosmic ray impact.

### Consequences for the Transmission Spectra

Here, it is analyzed whether the changes within the atmospheric composition have an impact on the simulated transmission spectrum as well. The data for the plots in this section were provided by Ben Taysum using GARLIC. Figure 5.24 shows the impact of the Carrington-like event of six hours compared to a reference run without particle event between 0.7–10 $\mu$m. The resolution of the simulated spectrum is $R = 300$. It can be seen in the lower panel of Fig. 5.24 that the transit depth within the most prominent water bands (around 6 $\mu$m) is increased by 0.25–0.45% for all scenarios, but a little bit more for the model simulations with less initial $N_2$ (blue and red lines). The transit depth in the

water band around 2.6 $\mu$m is increased by up to 0.25%. This matches with the production of additional water vapor during the particle event of Fig. 5.20 (a). The extra input of atomic hydrogen above ~180 km (Fig. 5.16 (dashed-dotted)) leads to small changes in the transit depth (upper panel of Fig. 5.24 (red, orange)) compared to the model runs with no hydrogen flux (blue, green). This is in good agreement with Fig. 5.20, where $H_2O$ is greater above 200 km within the model runs with higher hydrogen flux. In contrast to the model simulations without particle events, the changes due to the additional hydrogen are about one order of magnitude smaller and difficult to distinguish. At this altitude, the density decreases and weakens the contribution to the transmission spectrum.

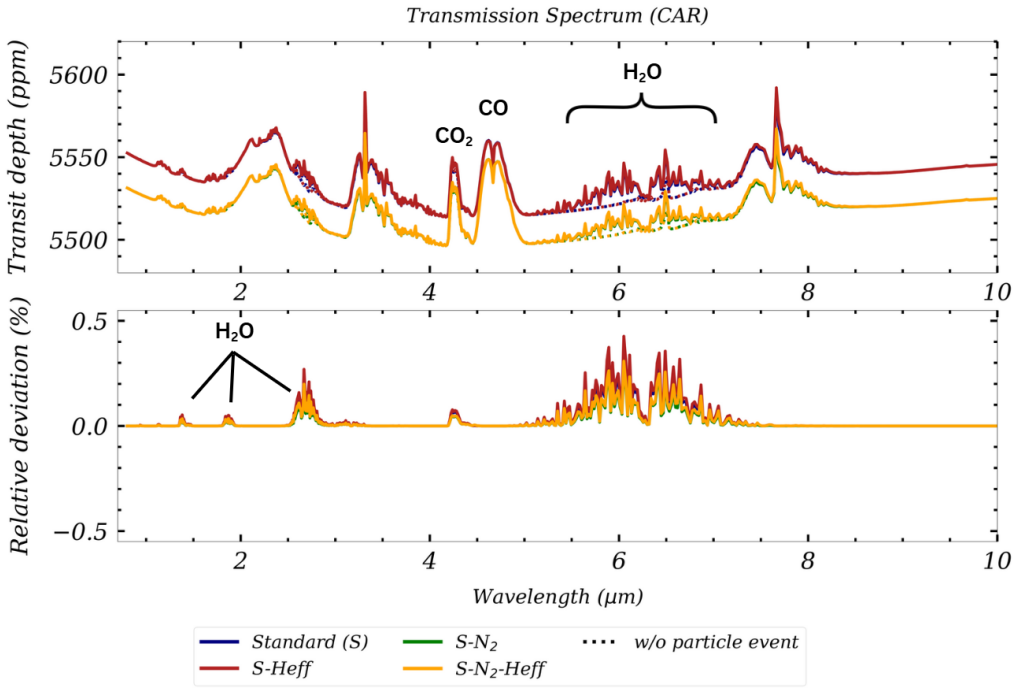


**Figure 5.24: Simulated transmission spectrum of LHS 1140 b during the Carrington-like particle impact.** The upper panel of this figure shows the simulated transmission spectrum (ppm) for the LHS 1140 b model runs, 'Standard' (blue), 'S-Heff' (red), 'S-$N_2$' (green), 'S-$N_2$-Heff' (orange), and the corresponding reference runs without particle event (dotted lines). The lower panel shows the relative deviation of the transit depth (%) for all the model scenarios. The band centers and bands of the different trace gases are indicated by the black lines. The data for the simulated transmission spectra were calculated with GARLIC at DLR using the output from the ExoTIC model runs at KIT. Subsequently, the results were visualised in the figure above and in figures 5.25–5.26.

Compared to the scenarios for TRAPPIST-1e, this spectrum of a $H_2$-dominated atmosphere shows more prominent peaks for methane (3.3 $\mu$m, 7.7 $\mu$m) due to the higher initial amount of $CH_4$ (upper panel in Fig. 5.24). This leads to lower concentrations of $CO_2$, because the methane weakens the $HO_x$ cycle for $CO_2$ reformation (Wunderlich et al., 2021, see R75).

$$CO + OH \longrightarrow CO_2 + H \tag{R75}$$

Thus, the peak for carbon monoxide (CO, 4.6 $\mu$m) is bigger compared to $CO_2$. The small visible peak at 4.3 $\mu$m, which can be attributed to $CO_2$, is likely related to the enhanced production of OH. This increases the $CO_2$ concentration in the atmosphere via reaction R75. The NIRISS instrument of the James Webb Space Telescope already measured two transits of LHS 1140 b. Figure 5.25 illustrates a comparison between the measured transmission spectrum (gray data points from Cadieux et al. (2024a), black from Damiano et al. (2024)) and the simulated spectrum for the different model simulations within the near infrared range from 0.7–5.0 $\mu$m.

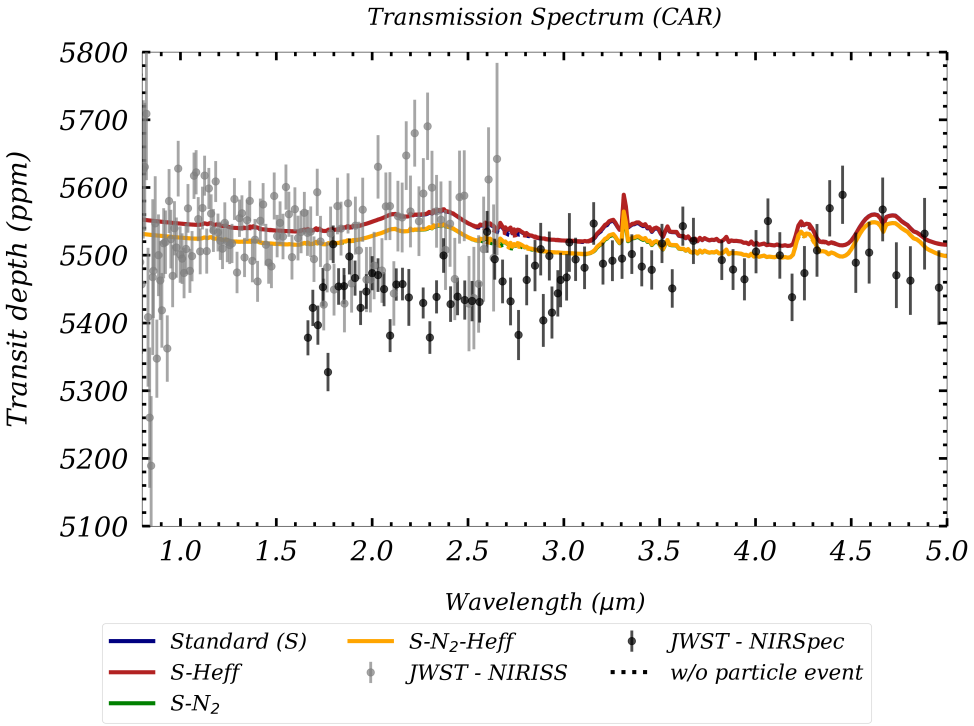


**Figure 5.25: Comparison of simulated and measured transmission spectra for LHS 1140 (b).** The figure shows a comparison between the transmission spectrum measured by the NIRISS/NIRSpec instrument (grey/black error bars) and the simulated transmission spectrum for the model simulations from table 5.4 with (solid lines) and without (dotted lines) particle event. The data is from Cadieux et al. (2024a) (grey) and Damiano et al. (2024) (black) with resolutions of $R \approx 100$ and $R \approx 65$.

The simulated spectra fit the measured data. However, the error bars are large and mask the influence of stellar energetic particles on the different atmospheres. The mean measurement noise for the measurements is with ~40 ppm lower compared to TRAPPIST-1e. Thus, less transits would be necessary to detect changes for example in the water

absorption band. With equation 5.1, a change in the signal of 25 ppm would require estimated ~24 transits for a signal-to-noise ratio of $S/N = 3$. The number of transits increase for the water band around 2.7 $\mu$m due to the smaller change in the transit depth. If further observations improve the measurement precision, the activity of the star and its impact on the spectral features should be taken into account when interpreting the atmospheric composition.

In comparison to the stronger Carrington-like event, the effect of GCRs is rather small, which is shown in Figure 5.26. There, the relative changes within the simulated transit depth are at least two orders of magnitude smaller (lower panel), matching the small absolute changes in the volume mixing ratio (see Fig. 5.23), especially in the most prominent water band around 5.7 $\mu$m. Here, the signal decreases, while it increases for the stronger Carrington-like event.

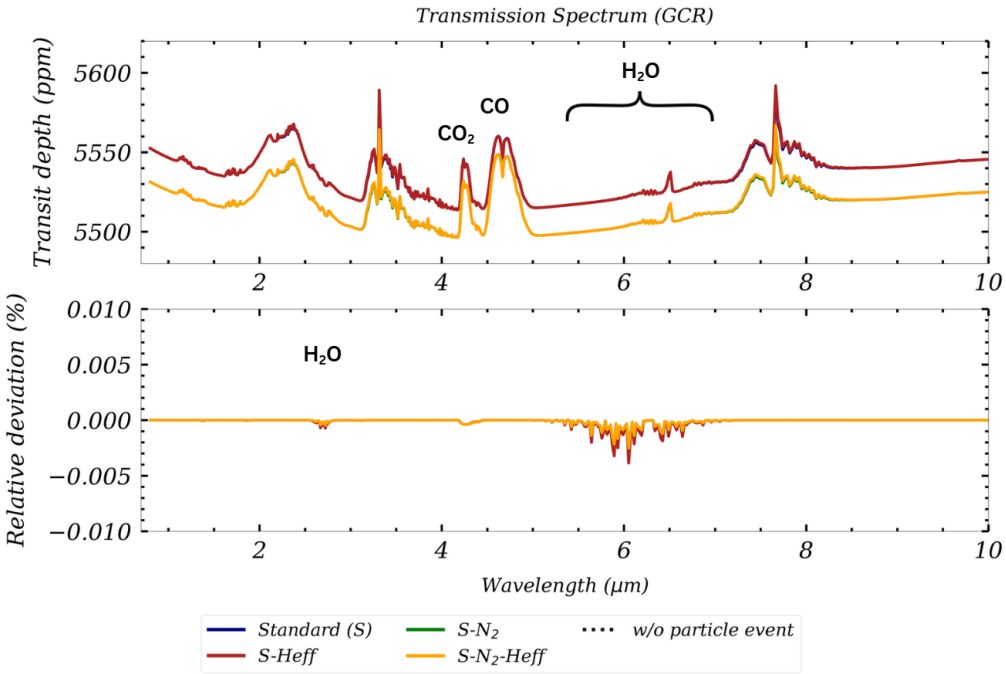


**Figure 5.26: Simulated transmission spectrum of LHS 1140 b during the GCR impact.** Same as Fig. 5.24, but for the impact of galactic cosmic rays. Note the different y-axis values for the relative deviation.

However, it should be pointed out that the particle flux of GCRs is small, but nearly constant, and is better described by a model experiment bringing the atmosphere into equilibrium, than by a short sporadic particle forcing as shown here. Due to the missing vertical transport and mixing in ExoTIC, such an experiment can not be carried out with

ExoTIC on long timescales. Hence, a model like 1D-Terra needs to be used in combination with particle forcing.

# 6 Summary

In this work, I studied the impact of energetic particle events on exoplanetary atmospheres. On Earth, such events are particularly known for depleting ozone through $NO_x$ and $HO_x$ species (Sinnhuber et al., 2012). The most common stars in the universe are red M-dwarf stars, most of which are also significantly more active than the Sun. This was the motivation to expand this research area to diverse planets orbiting M-dwarf stars. Since the James Webb Space Telescope is capable of characterizing atmospheres of Earth-sized planets, it is also helpful to constrain the impact of energetic particles on future observations.

To quantify the influence of energetic particles, I used the ion-chemistry model ExoTIC. Following the new technical developments, such as the use on HPC clusters and output in netCDF format, the ion chemical framework has been extended by the abiotic production of $N_2O$ and $H_2/H_2O$ ionization. In addition, sulfur chemistry was implemented into ExoTIC as part of a master's thesis by Chiara Schleif (Schleif, 2024). The principle workflow of the doctoral thesis to address the scientific questions formulated in section 1.2 is illustrated in figure 6.1. The new developments are highlighted in green and orange within figure 6.1. Input parameters like the stellar spectrum, ionization rates and atmospheric profiles (upper left box) were used to calculate the changes in the atmospheric composition during energetic particle events. Results of these model experiments formed the basis to calculate transmission spectra of the simulations using GARLIC. The following paragraphs summarize the results for the different experiments with the further developed ExoTIC model.

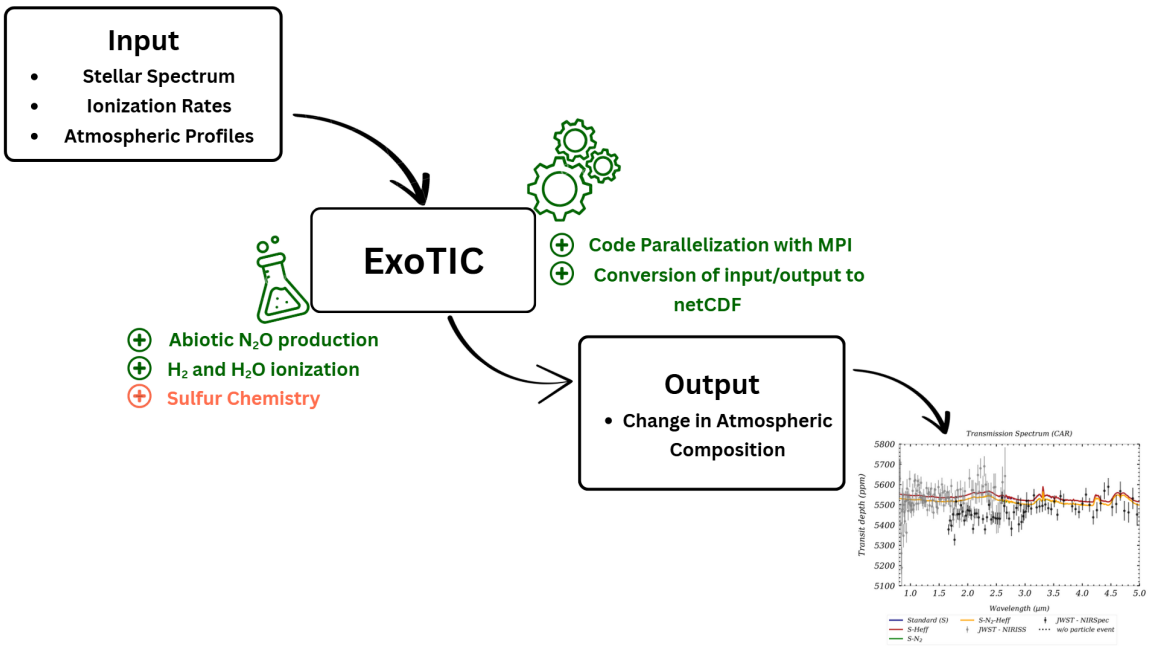


**Figure 6.1: Summary of the workflow for the doctoral thesis.** The figure illustrates the principle workflow during the thesis to address the scientific questions. Developments made within the ExoTIC model are highlighted in green. The sulfur chemistry (orange) was added by Schleif (2024).

Firstly, the new chemical framework was tested with modern Earth atmospheric conditions during the energetic particle event on $28^{th}/29^{th}$ October 2003. This so-called Halloween Event has been measured by the MIPAS instrument and provides good observations to validate the newly implemented reactions. The abiotic production of nitrous oxide is in good agreement to the measurements and model simulations obtained during the Halloween event. In addition, the four different sensitivity experiments, including the sulfur chemistry and $H_2/H_2O$-ionization showed no significant deviations that conflict with the observations. This new chemical framework was then applied to different atmospheres of the two M-dwarf orbiting planets TRAPPIST-1e and LHS 1140 b. While the atmospheres assumed for TRAPPIST-1e are Earth-like, the atmosphere of LHS 1140 b is dominated by $H_2$.

A first step away from Earth was to investigate various atmospheric scenarios still dominated by $N_2$. These ranged from a scenario involving only volcanic outgassing, to volcanic outgassing and ocean, to a scenario involving ocean, volcanism, and biogenic fluxes as on Earth. The impact of stellar energetic particles from the M-dwarf star TRAPPIST-1 was then investigated for these three atmospheres of the planet TRAPPIST-1e. The results showed that in atmospheres with high amount of $O_2$, ozone is reduced in the upper at-

mosphere similar to Earth, whereas in the scenarios with no biogenic fluxes mostly $O_3$ production by the smog mechanism dominated between ~40 and 70 km and below 40 km ('Dry-dead'). The production of $HO_x$ and $NO_x$ was stronger for the oxygen-rich scenario. Furthermore, it has been shown that nitrous oxide ($N_2O$) can also be produced abiotically during a particle event in atmospheres on planets orbiting M-stars. All these changes in the atmosphere are reflected in the transmission spectra.

A much more 'exotic' atmosphere was assumed for LHS 1140 b. It is bigger than TRAPPIST-1e and could prevail a lighter hydrogen-dominated atmosphere, which wasn't simulated with the ExoTIC model before. It has been shown that within $H_2$-dominated atmospheres, water vapor is produced by strong stellar energetic particles. This leads to an increase in the transit depth in the water bands of up to ~0.45% (around 6 $\mu$m). The effect is marginally stronger for scenarios with additional hydrogen flux. The changes of the nitrogen species in the range of (ppb) are too small to cause significant differences in the transmission spectrum. The same is true for the GCR impact, where the low ionization rates lead to differences that are orders of magnitude smaller compared to the stronger Carrington-like particle event.

The scientific questions formulated in the introduction were answered with the help of the further developed model and the workflow (see Fig. 6.1) – beginning with:

***Q1. How do stellar energetic particles and galactic cosmic rays influence the composition of different atmospheres of planets around M-dwarf stars?***

This work shows that the influence of stellar energetic particles on atmospheres around M-dwarf stars could be quite diverse depending on the initial atmospheric composition. Where significant ozone depletion still occurs on Earth, ozone production may also prevail in $N_2$ atmospheres and is negligible in $H_2$-dominated atmospheres with low amounts of molecular oxygen. Especially in $N_2$-dominated atmospheres, particle precipitation leads to more abiotic production of nitrous oxide. In $H_2$-dominated atmospheres, the main focus is on the production of additional $H_2O$ during energetic particle events, while the composition changes for other trace gases remain largely unchanged. Regarding the small effect of galactic cosmic rays, it is recommended to simulate longer time scales using the 1D-TERRA climate-chemistry model to better quantify the effect on atmospheric composition, since galactic cosmic rays represent a continuous source of energetic particles.

The two remaining research questions

***Q2. What impact do these changes in atmospheric composition have on the observed transmission spectra and their interpretation?***

and

***Q3. Does this affect the observability and interpretation of the so-called biosignatures in current and future observations?***

are closely related to each other and can be addressed together. The changes in atmospheric composition during stellar energetic particle events as shown in the simulated transmission spectra, influencing directly the transit depth of different absorption bands. The spectral signature of nitrous oxide would increase by 15-25 ppm and due to the lower UV-flux of M-Stars, the produced $N_2O$ is more stable against photolysis compared to G-Stars like the Sun. For the detection of such changes, more than 144 transits are required for a signal-to-noise ratio of $S/N = 3$, which is very much for JWST. However, changes of ~25 ppm should be seen as a lower limit, since the model runs were limited in time and cover just a selection of multiple events for a frequent flaring star. But with more and more precise measurements, this could result in a clear detection of $N_2O$ in the future. Since it is treated as a potential biosignature, this could pose the risk of incorrectly concluding a higher biogenic activity. In particular, the risk is bigger for $N_2$-dominated atmospheres with no biogenic fluxes. In the vicinity of very active stars, $N_2O$ is more of a marker for stellar activity than a good biosignature. Ozone, on the other hand, can be influenced in different ways even in more Earth-like atmospheres and is therefore even more difficult to interpret as a biosignature than $N_2O$. For $H_2$-dominated atmospheres, the simulated influence of stronger ionization events on the transmission spectrum is also not negligible, but only becomes relevant as the precision of the measurement data increases. Compared to TRAPPIST-1e, the measurement noise is smaller. Therefore, less transits (~24) are required according to equation 5.1. The smaller influence of galactic cosmic rays emphasizes the need to iterate between the models of the INCREASE workflow.

In general, the findings show that energetic particles have a significant impact on potential biosignatures. Thus, it is recommended to include stellar energetic particles into atmospheric models for the interpretation of measurements and observations, particularly in the vicinity of active stars. Otherwise, this could lead to false positives or false negatives. It is therefore essential to consider a combination of all factors.

### Room for further Model Improvements

Technological evolution is continuously improving the ability to characterize exoplanetary atmospheres more accurately. In the future, the resolution of available instruments will also enable the analysis of atmospheres around Sun-like stars. This section highlights a possible extension for the ExoTIC ion chemistry model and briefly mentions observation missions that are planned for the near or distant future.

A recent study of Wallner et al. (2022) suggests an abiotic pathway of molecular $O_2$ production out of sulfur dioxide ($SO_2$). In this process, $SO_2$ is doubly ionized and decomposes via the reaction R76 into ionized oxygen $O_2^+$ and ionized atomic sulfur.

$$SO_2{}^{2+} \longrightarrow O_2{}^{+} + S^{+} \tag{R76}$$

Due to recombination or charge exchange reactions, $O_2^+$ can be converted to molecular oxygen. The authors conclude that this reaction channel could be an important contribution to the $O_2$ budget besides the photolysis of $CO_2$. $SO_2$ can occur in quite large concentrations, especially on planets or moons with high volcanic activity and subsequent outgassing, such as Venus or the Jovian moon Io.

Since the sulfur chemistry was added into ExoTIC's chemistry module during the Master thesis of Chiara Schleif (Schleif, 2024), the next step would be to include this production of $O_2^+$ in the ion chemistry module of ExoTIC as well, in order to account for this path of abiotic oxygen production in $SO_2$-dominated atmospheres.

The scientific interest in observing and characterizing exoplanetary atmospheres will continue to grow. Besides JWST, further space- and ground-based missions are planned in the upcoming years that will pursue the scientific goals. The overarching objective is to improve the data basis for more accurate statements about the composition of exoplanetary atmospheres.

### PLATO – PLAnetary Transits and Oscillations of stars

The PLATO mission is initiated by the European Space Agency (ESA) and will be launched in 2026. Its aim is, in particular, to constrain atmospheric and planetary parameters for hot Jupiters around Sun-like G-stars using the transit method (Grenfell et al., 2020). Thus,

it will provide information about atmospheric types and targets, which could be observed by follow-up missions like ESA's Ariel[1].

### LIFE Mission and Habitable World Observatory (HWO)

In the distant future, two different approaches are currently being developed for missions to characterize the atmospheres of exoplanets that are similar to Earth and located in the habitable zone of Sun-like stars. These approaches are based on a direct observation method and are therefore independent of the fortunate geometry of a transit. One is NASA's **H**abitable **W**orld **O**bservatory (HWO) mission (National Academies of Sciences, Engineering, and Medicine, 2023) and the other is the European-led **L**arge **I**nterferometer **F**or **E**xoplanets (LIFE) mission (Quanz, S. P. et al., 2022b). HWO will collect the reflected light from the host stars, which contains the fingerprints of the atmospheric composition. It operates mainly in the UV/VIS/NIR part of the electromagnetic spectrum (National Academies of Sciences, Engineering, and Medicine, 2023).

In contrast, LIFE pursues the approach of thermal emission from exoplanets. This occurs mainly in the mid-infrared (MIR) range, where many potential biosignatures have their absorption bands (Kammerer, J. et al., 2022). In addition, the emission spectra provide information about the thermal structure of the atmosphere, constraining the planets' climate (Quanz, S. P. et al., 2022a). A recent study from Alei, E. et al. (2024) recommends a joint use of these two missions to obtain better retrievals for the atmospheric trace gases and the temperature profile.

In combination with ground-based star observation, the direct imaging approaches are well suited to provide observations on changes in exoplanetary atmospheres following a stellar particle event, because one is not dependent on a random transit. The atmosphere of the affected planet should then be examined immediately after the recorded flares.

Even if the launch of HWO and LIFE is not planned before the 2040s, there are exciting missions (PLATO, ARIEL) in the upcoming years that will significantly improve the data basis for characterizing exoplanetary atmospheres.

[1] https://www.esa.int/Science_Exploration/Space_Science/Ariel

# Bibliography


Adams, F. C., Bodenheimer, P., & Laughlin, G. (2005). M dwarfs: planet formation and long term evolution. *Astronomische Nachrichten*, *326*(10), 913–919. https://doi.org/https://doi.org/10.1002/asna.200510440

Agol, E., Dorn, C., Grimm, S. L., Turbet, M., Ducrot, E., Delrez, L., Gillon, M., Demory, B.-O., Burdanov, A., Barkaoui, K., Benkhaldoun, Z., Bolmont, E., Burgasser, A., Carey, S., de Wit, J., Fabrycky, D., Foreman-Mackey, D., Haldemann, J., Hernandez, D. M., … Grootel, V. V. (2021). Refining the transit-timing and photometric analysis of trappist-1: Masses, radii, densities, dynamics, and ephemerides. *The Planetary Science Journal*, *2*(1), 1. https://doi.org/10.3847/PSJ/abd022

Agostinelli, S., Allison, J., Amako, K., Apostolakis, J., Araujo, H., Arce, P., Asai, M., Axen, D., Banerjee, S., Barrand, G., Behner, F., Bellagamba, L., Boudreau, J., Broglia, L., Brunengo, A., Burkhardt, H., Chauvie, S., Chuma, J., Chytracek, R., … Zschiesche, D. (2003). Geant4—a simulation toolkit. *Nuclear Instruments and Methods in Physics Research Section A: Accelerators, Spectrometers, Detectors and Associated Equipment*, *506*(3), 250–303. https://doi.org/https://doi.org/10.1016/S0168-9002(03)01368-8

Alei, E., Quanz, S. P., Konrad, B. S., Garvin, E. O., Kofman, V., Mandell, A., Angerhausen, D., Mollière, P., Meyer, M. R., Robinson, T., Rugheimer, S., & the LIFE Collaboration. (2024). Large Interferometer For Exoplanets (LIFE) - XIII. The value of combining thermal emission and reflected light for the characterization of Earth twins. *A&A*, *689*, A245. https://doi.org/10.1051/0004-6361/202450320

Armitage, P. J., & Kley, W. (2019). *From Protoplanetary Disks to Planet Formation: Saas-Fee Advanced Course 45. Swiss Society for Astrophysics and Astronomy* (M. Audard, M. R. Meyer, & Y. Alibert, Eds.). Springer Berlin Heidelberg. https://doi.org/10.1007/978-3-662-58687-7

Baker, D. N., Mason, G. M., & Mazur, J. E. (2012). A small spacecraft mission with large accomplishments. *Eos, Transactions American Geophysical Union*, *93*(34), 325–326.

Banjac, S., Herbst, K., & Heber, B. (2019). The Atmospheric Radiation Interaction Simulator (AtRIS): Description and Validation. *Journal of Geophysical Research: Space Physics*, *124*(1), 50–67. https://doi.org/https://doi.org/10.1029/2018JA026042

Bates, D. R., & Nicolet, M. (1950). The photochemistry of atmospheric water vapor. *Journal of Geophysical Research (1896-1977)*, *55*(3), 301–327. https://doi.org/https://doi.org/10.1029/JZ055i003p00301

Bauer, S., & Lammer, H. (2010). *Planetary Aeronomy: Atmosphere Environments in Planetary Systems* (1st ed.). Springer Berlin, Heidelberg.

Baumgaertner, A. J., Jöckel, P., Riede, H., Stiller, G., & Funke, B. (2010). Energetic particle precipitation in echam5/messy–part 2: Solar proton events. *Atmospheric Chemistry and Physics*, *10*(15), 7285–7302. https://doi.org/10.5194/acp-10-7285-2010

Beech, M. (2019). *Introducing the Stars: Formation, Structure and Evolution*. Springer. https://doi.org/10.1007/978-3-030-11704-7

Borthakur, M. (2025). *Investigation of the impact of atmospheric ionisation on middle atmosphere chemistry and dynamics - model studies with ExoTIC and EMAC* [Doctoral dissertation, Karlsruher Institut für Technologie (KIT)]. Karlsruher Institut für Technologie (KIT). https://doi.org/10.5445/IR/1000177654

Cadieux, C., Doyon, R., MacDonald, R. J., Turbet, M., Artigau, É., Lim, O., Radica, M., Fauchez, T. J., Salhi, S., Dang, L., et al. (2024a). Transmission Spectroscopy of the Habitable Zone Exoplanet LHS 1140 b with JWST/NIRISS. *The Astrophysical Journal Letters*, *970*(1), L2. https://doi.org/10.3847/2041-8213/ad5afa

Cadieux, C., Plotnykov, M., Doyon, R., Valencia, D., Jahandar, F., Dang, L., Turbet, M., Fauchez, T. J., Cloutier, R., Cherubim, C., et al. (2024b). New mass and radius constraints on the LHS 1140 planets: LHS 1140 b is either a temperate mini-Neptune or a water world. *The Astrophysical Journal Letters*, *960*(1), L3. https://doi.org/10.3847/2041-8213/ad1691

Chapman, S. (1932). Discussion of memoirs. On a theory of upper-atmospheric ozone. *Quarterly Journal of the Royal Meteorological Society*, *58*(243), 11–13. https://doi.org/https://doi.org/10.1002/qj.49705824304

Chipperfield, M. (1999). Multiannual simulations with a three-dimensional chemical transport model. *Journal of Geophysical Research: Atmospheres*, *104*(D1), 1781–1805. https://doi.org/https://doi.org/10.1029/98JD02597

Cliver, E. W., Schrijver, C. J., Shibata, K., & Usoskin, I. G. (2022). Extreme solar events. *Living Reviews in Solar Physics*, *19*(1), 2. https://doi.org/10.1007/s41116-022-00033-8

Crutzen, P. J. (1970). The influence of nitrogen oxides on the atmospheric ozone content. *Quarterly Journal of the Royal Meteorological Society*, *96*(408), 320–325. https://doi.org/https://doi.org/10.1002/qj.49709640815

Crutzen, P. J., Isaksen, I. S. A., & Reid, G. C. (1975). Solar Proton Events: Stratospheric Sources of Nitric Oxide. *Science*, *189*(4201), 457–459. https://doi.org/10.1126/science.189.4201.457

Damiano, M., Bello-Arufe, A., Yang, J., & Hu, R. (2024). LHS 1140 b is a potentially habitable water world. *The Astrophysical Journal Letters*, *968*(2), L22. https://doi.org/10.3847/2041-8213/ad5204

Dittmann, J. A., Irwin, J. M., Charbonneau, D., Bonfils, X., Astudillo-Defru, N., Haywood, R. D., Berta-Thompson, Z. K., Newton, E. R., Rodriguez, J. E., Winters, J. G., Tan, T.-G., Almenara, J.-M., Bouchy, F., Delfosse, X., Forveille, T., Lovis, C., Murgas, F., Pepe, F., Santos, N. C., … Dressing, C. D. (2017). A temperate rocky super-earth transiting a nearby cool star. *Nature*, *544*(7650), 333–336. https://doi.org/10.1038/nature22055

Dole, S., & Asimov, I. (1964). *Planets for man* (tech. rep.). Defense Technical Information Center.

Doyon, R., Hutchings, J. B., Beaulieu, M., Albert, L., Lafrenière, D., Willott, C., Touahri, D., Rowlands, N., Maszkiewicz, M., Fullerton, A. W., et al. (2012). The jwst fine guidance sensor (fgs) and near-infrared imager and slitless spectrograph (niriss). *Space telescopes and instrumentation 2012: Optical, infrared, and millimeter wave*, *8442*, 1005–1017.

Encrenaz, T., & Haghighipour, N. (2020). Exoplanet, Detection, and Characterization. In M. Gargaud, W. M. Irvine, R. Amils, P. Claeys, H. J. Cleaves, M. Gerin, D. Rouan, T. Spohn, S. Tirard, & M. Viso (Eds.), *Encyclopedia of astrobiology* (pp. 1–14). Springer Berlin Heidelberg. https://doi.org/10.1007/978-3-642-27833-4_553-6

Encrenaz, T., & Coustenis, A. (2018). Composition and Chemistry of the Atmospheres of Terrestrial Planets: Venus, the Earth, Mars, and Titan. In H. J. Deeg & J. A. Belmonte (Eds.), *Handbook of exoplanets* (pp. 187–214). Springer International Publishing. https://doi.org/10.1007/978-3-319-55333-7_45

Espinoza, N., Allen, N. H., Glidden, A., Lewis, N. K., Seager, S., Cañas, C. I., Grant, D., Gressier, A., Courreges, S., Stevenson, K. B., Ranjan, S., Colón, K., Morris, B. M., MacDonald, R. J., Long, D., Wakeford, H. R., Valenti, J. A., Alderson, L., Batalha, N. E., … van der Marel, R. P. (2025). JWST-TST DREAMS: NIRSpec/PRISM Transmission Spectroscopy of the Habitable Zone Planet TRAPPIST-1 e. *The Astrophysical Journal Letters*, *990*(2), L52. https://doi.org/10.3847/2041-8213/adf42e

Evans, W. F. J., & Llewellyn, E. J. (1972). Measurements of mesospheric ozone from observations of the 1.27.$\mu$ band. *Radio Science*, *7*(1), 45–50. https://doi.org/10.1029/RS007i001p00045

Farman, J. C., Gardiner, B. G., & Shanklin, J. D. (1985). Large losses of total ozone in antarctica reveal seasonal clox/nox interaction. *Nature*, *315*(6016), 207–210. https://doi.org/10.1038/315207a0

Fressin, F., Torres, G., Rowe, J. F., Charbonneau, D., Rogers, L. A., Ballard, S., Batalha, N. M., Borucki, W. J., Bryson, S. T., Buchhave, L. A., et al. (2012). Two Earth-sized planets orbiting Kepler-20. *Nature*, *482*(7384), 195–198.

Funke, B., Baumgaertner, A., Calisto, M., Egorova, T., Jackman, C. H., Kieser, J., Krivolutsky, A., López-Puertas, M., Marsh, D. R., Reddmann, T., Rozanov, E., Salmi, S.-M., Sinnhuber, M., Stiller, G. P., Verronen, P. T., Versick, S., von Clarmann, T., Vyushkova, T. Y., Wieters, N., & Wissing, J. M. (2011). Composition changes after the "Halloween" solar proton event: the High Energy Particle Precipitation in the Atmosphere (HEPPA) model versus MIPAS data intercomparison study. *Atmospheric Chemistry and Physics*, *11*(17), 9089–9139. https://doi.org/10.5194/acp-11-9089-2011

Gaia Collaboration, Brown, A. G. A., Vallenari, A., Prusti, T., de Bruijne, J. H. J., Babusiaux, C., Bailer-Jones, C. A. L., Biermann, M., Evans, D. W., Eyer, L., Jansen, F., Jordi, C., Klioner, S. A., Lammers, U., Lindegren, L., Luri, X., Mignard, F., Panem, C., Pourbaix, D., … Zwitter, T. (2018). Gaia Data Release 2 - Summary of the contents and survey properties. *A&A*, *616*, A1. https://doi.org/10.1051/0004-6361/201833051

Gardner, J. P., Mather, J. C., Clampin, M., Doyon, R., Greenhouse, M. A., Hammel, H. B., Hutchings, J. B., Jakobsen, P., Lilly, S. J., Long, K. S., Lunine, J. I., Mccaughrean, M. J., Mountain, M., Nella, J., Rieke, G. H., Rieke, M. J., Rix, H.-W., Smith, E. P., Sonneborn, G., … Wright, G. S. (2006). The James Webb Space Telescope. *Space Science Reviews*, *123*(4), 485–606. https://doi.org/10.1007/s11214-006-8315-7

Gillon, M., Jehin, E., Lederer, S. M., Delrez, L., de Wit, J., Burdanov, A., Van Grootel, V., Burgasser, A. J., Triaud, A. H. M. J., Opitom, C., Demory, B.-O., Sahu, D. K., Bardalez Gagliuffi, D., Magain, P., & Queloz, D. (2016). Temperate earth-sized planets transiting a nearby ultracool dwarf star. *Nature*, *533*(7602), 221–224. https://doi.org/10.1038/nature17448

Gillon, M., Triaud, A. H. M. J., Demory, B.-O., Jehin, E., Agol, E., Deck, K. M., Lederer, S. M., de Wit, J., Burdanov, A., Ingalls, J. G., Bolmont, E., Leconte, J., Raymond, S. N., Selsis, F., Turbet, M., Barkaoui, K., Burgasser, A., Burleigh, M. R., Carey, S. J., … Queloz, D. (2017). Seven temperate terrestrial planets around the nearby ultracool dwarf star trappist-1. *Nature*, *542*(7642), 456–460. https://doi.org/10.1038/nature21360

Glasse, A., Rieke, G. H., Bauwens, E., García-Marín, M., Ressler, M. E., Rost, S., Tikkanen, T. V., Vandenbussche, B., & Wright, G. S. (2015). The mid-infrared instrument for the james webb space telescope, ix: Predicted sensitivity. *Publications of the Astronomical Society of the Pacific*, *127*(953), 686. https://doi.org/10.1086/682259

Goldblatt, C., Robinson, T. D., Zahnle, K. J., & Crisp, D. (2013). Low simulated radiation limit for runaway greenhouse climates. *Nature Geoscience*, *6*(8), 661–667. https://doi.org/10.1038/ngeo1892

Goody, R. M., & Yung, Y. L. (1995). *Atmospheric radiation: theoretical basis*. Oxford university press.

Gordon, I., Rothman, L., Hill, C., Kochanov, R., Tan, Y., Bernath, P., Birk, M., Boudon, V., Campargue, A., Chance, K., Drouin, B., Flaud, J.-M., Gamache, R., Hodges,

J., Jacquemart, D., Perevalov, V., Perrin, A., Shine, K., Smith, M.-A., … Zak, E. (2017). The hitran2016 molecular spectroscopic database [HITRAN2016 Special Issue]. *Journal of Quantitative Spectroscopy and Radiative Transfer*, *203*, 3–69. https://doi.org/https://doi.org/10.1016/j.jqsrt.2017.06.038

Grenfell, J. L. (2018). Atmospheric Biosignatures. In H. J. Deeg & J. A. Belmonte (Eds.), *Handbook of exoplanets* (pp. 3159–3172). Springer International Publishing. https://doi.org/10.1007/978-3-319-55333-7_68

Grenfell, J. L., Gebauer, S., Godolt, M., Palczynski, K., Rauer, H., Stock, J., von Paris, P., Lehmann, R., & Selsis, F. (2013). Potential Biosignatures in Super-Earth Atmospheres II. Photochemical Responses [PMID: 23683046]. *Astrobiology*, *13*(5), 415–438. https://doi.org/10.1089/ast.2012.0926

Grenfell, J. L., Godolt, M., Cabrera, J., Carone, L., Muñoz, A. G., Kitzmann, D., Smith, A. M. S., & Rauer, H. (2020). Atmospheric Characterization via Broadband Color Filters on the PLAnetary Transits and Oscillations of stars (PLATO) Mission. *Experimental Astronomy*, *50*(1), 1–49. https://doi.org/10.1007/s10686-020-09660-1

Grenfell, J. L., Grießmeier, J.-M., Patzer, B., Rauer, H., Segura, A., Stadelmann, A., Stracke, B., Titz, R., & Von Paris, P. (2007). Biomarker Response to Galactic Cosmic Ray-Induced NOx And The Methane Greenhouse Effect in The Atmosphere of An Earth-Like Planet Orbiting An M Dwarf Star [PMID: 17407408]. *Astrobiology*, *7*(1), 208–221. https://doi.org/10.1089/ast.2006.0129

Grenfell, J. L., Grießmeier, J.-M., von Paris, P., Patzer, A. B. C., Lammer, H., Stracke, B., Gebauer, S., Schreier, F., & Rauer, H. (2012). Response of atmospheric biomarkers to NO x-induced photochemistry generated by stellar cosmic rays for Earth-like planets in the habitable zone of M dwarf stars. *Astrobiology*, *12*(12), 1109–1122. https://doi.org/10.1089/ast.2011.0682

Grootel, V. V., Fernandes, C. S., Gillon, M., Jehin, E., Manfroid, J., Scuflaire, R., Burgasser, A. J., Barkaoui, K., Benkhaldoun, Z., Burdanov, A., Delrez, L., Demory, B.-O., Wit, J. d., Queloz, D., & Triaud, A. H. M. J. (2018). Stellar parameters for trappist-1. *The Astrophysical Journal*, *853*(1), 30. https://doi.org/10.3847/1538-4357/aaa023

Hansen, C. J., Kawaler, S. D., & Trimble, V. (2004). *Stellar interiors: Physical principles, structure, and evolution* (2nd ed.). Springer Science+Business Media. https://doi.org/10.1007/978-1-4419-9110-2

Hanslmeier, A. (2023). *Introduction to astronomy and astrophysics*. Springer Nature. https://doi.org/10.1007/978-3-662-64637-3

Henry, T. J., & Jao, W.-C. (2024). The character of m dwarfs. *Annual Review of Astronomy and Astrophysics*, *62*(Volume 62, 2024), 593–633. https://doi.org/https://doi.org/10.1146/annurev-astro-052722-102740

Herbst, K., Grenfell, J. L., Sinnhuber, M., & Wunderlich, F. (2022). INCREASE: An updated model suite to study the INfluence of Cosmic Rays on Exoplanetary AtmoSpherEs. *Astronomische Nachrichten*, *343*(4), e210072. https://doi.org/https://doi.org/10.1002/asna.20210072

Herbst, K., Bartenschlager, A., Grenfell, J. L., Iro, N., Sinnhuber, M., Taysum, B., Wunderlich, F., Engelbrecht, N. E., Light, J., Moloto, K. D., Harre, J.-V., Rauer, H., & Schreier, F. (2024). Impact of Cosmic Rays on Atmospheric Ion Chemistry and Spectral Transmission Features of TRAPPIST-1e. *The Astrophysical Journal*, *961*(2), 164. https://doi.org/10.3847/1538-4357/ad0895

Herbst, K., Grenfell, John Lee, Sinnhuber, Miriam, Rauer, Heike, Heber, Bernd, Banjac, Sasa, Scheucher, Markus, Schmidt, Vanessa, Gebauer, Stefanie, Lehmann, Ralph, & Schreier, Franz. (2019a). A new model suite to determine the influence of cosmic rays on (exo)planetary atmospheric biosignatures - Validation based on modern Earth. *A&A*, *631*, A101. https://doi.org/10.1051/0004-6361/201935888

Herbst, K., Papaioannou, Athanasios, Banjac, Saša, & Heber, Bernd. (2019b). From solar to stellar flare characteristics - On a new peak size distribution for G-, K-, and M-dwarf star flares. *A&A*, *621*, A67. https://doi.org/10.1051/0004-6361/201832789

Herbst, K., Scherer, K., Ferreira, S. E. S., Baalmann, L. R., Engelbrecht, N. E., Fichtner, H., Kleimann, J., Toit Strauss, R. D., Moeketsi, D. M., & Mohamed, S. (2020). On the Diversity of M-star Astrospheres and the Role of Galactic Cosmic Rays Within. *The Astrophysical Journal Letters*, *897*(2), L27. https://doi.org/10.3847/2041-8213/ab9df3

Herron, J. T. (1999). Evaluated Chemical Kinetics Data for Reactions of N($^2D$), N($^2P$), and $N_2$(A $^3\Sigma_u^+$) in the Gas Phase. *Journal of Physical and Chemical Reference Data*, *28*(5), 1453–1483. https://doi.org/10.1063/1.556043

Huntress Jr, W. T. (1977). Laboratory studies of bimolecular reactions of positive ions in interstellar clouds, in comets, and in planetary atmospheres of reducing composition. *Astrophysical Journal Supplement Series, vol. 33, Apr. 1977, p. 495-514.*, *33*, 495–514. https://doi.org/10.1086/190439

Innes, H., Tsai, S.-M., & Pierrehumbert, R. T. (2023). The runaway greenhouse effect on hycean worlds. *The Astrophysical Journal*, *953*(2), 168. https://doi.org/10.3847/1538-4357/ace346

Itikawa, Y. (2002). Cross Sections for Electron Collisions With Carbon Dioxide. *Journal of Physical and Chemical Reference Data*, *31*(3), 749–767. https://doi.org/10.1063/1.1481879

Itikawa, Y., & Mason, N. (2005). Cross Sections for Electron Collisions with Water Molecules. *Journal of Physical and Chemical Reference Data*, *34*(1), 1–22. https://doi.org/10.1063/1.1799251

Jackman, C. H., DeLand, M. T., Labow, G. J., Fleming, E. L., Weisenstein, D. K., Ko, M. K. W., Sinnhuber, M., & Russell, J. M. (2005). Neutral atmospheric influences of the solar proton events in October–November 2003. *Journal of Geophysical Research: Space Physics*, *110*(A9). https://doi.org/https://doi.org/10.1029/2004JA010888

Jakobsen, P., Ferruit, P., Alves de Oliveira, C., Arribas, S., Bagnasco, G., Barho, R., Beck, T. L., Birkmann, S., Böker, T., Bunker, A. J., Charlot, S., de Jong, P., de Marchi, G., Ehrenwinkler, R., Falcolini, M., Fels, R., Franx, M., Franz, D., Funke, M., … Zincke, C. (2022). The Near-Infrared Spectrograph (NIRSpec) on the James Webb Space Telescope - I. Overview of the instrument and its capabilities. *A&A*, *661*, A80. https://doi.org/10.1051/0004-6361/202142663

Johnson, R. E., Combi, M. R., Fox, J. L., Ip, W.-H., Leblanc, F., McGrath, M. A., Shematovich, V. I., Strobel, D. F., & Waite, J. H. (2008). Exospheres and atmospheric escape. *Space Science Reviews*, *139*(1), 355–397. https://doi.org/10.1007/s11214-008-9415-3

Johnstone, C. P., Güdel, M., Lüftinger, T., Toth, G., & Brott, I. (2015). Stellar winds on the main-sequence - I. Wind model. *A&A*, *577*, A27. https://doi.org/10.1051/0004-6361/201425300

Jones, J., Birkinshaw, K., & Twiddy, N. (1981). Rate coefficients and product ion distributions for the reactions of $OH^+$ and $H_2O^+$ with $N_2$ , $O_2$, NO. $N_2O$, Xe, CO, $CO_2$, $H_2S$ and $H_2$ at 300 K. *Chemical Physics Letters*, *77*(3), 484–488. https://doi.org/https://doi.org/10.1016/0009-2614(81)85191-3

Jones, R., & Rees, M. (1973). Time dependent studies of the aurora—i. ion density and composition. *Planetary and Space Science*, *21*(4), 537–557. https://doi.org/https://doi.org/10.1016/0032-0633(73)90069-X

Kammerer, J., Quanz, Sascha P., Dannert, Felix, & the LIFE Collaboration. (2022). Large Interferometer For Exoplanets (LIFE) - VI. Detecting rocky exoplanets in the habitable zones of Sun-like stars. *A&A*, *668*, A52. https://doi.org/10.1051/0004-6361/202243846

Karpas, Z., & Huntress, W. (1978). Reactions of $OH^+$ and $H_2O^+$ ions with some diatomic and simple polyatomic molecules. *Chemical Physics Letters*, *59*(1), 87–89. https://doi.org/https://doi.org/10.1016/0009-2614(78)85621-8

Kasting, J. F., Whitmire, D. P., & Reynolds, R. T. (1993). Habitable Zones around Main Sequence Stars. *Icarus*, *101*(1), 108–128. https://doi.org/https://doi.org/10.1006/icar.1993.1010

Kazil, J., Kopp, E., Chabrillat, S., & Bishop, J. (2003). The University of Bern Atmospheric Ion Model: Time-dependent modeling of the ions in the mesosphere and lower thermosphere. *Journal of Geophysical Research: Atmospheres*, *108*(D14). https://doi.org/https://doi.org/10.1029/2002JD003024

Kelly, C. W., Chipperfield, M. P., Plane, J. M. C., Feng, W., Sheese, P. E., Walker, K. A., & Boone, C. D. (2018). An Explanation for the Nitrous Oxide Layer Observed in the Mesopause Region. *Geophysical Research Letters*, *45*(15), 7818–7827. https://doi.org/https://doi.org/10.1029/2018GL078895

Kieffer, L. J., & Dunn, G. H. (1966). Electron impact ionization cross-section data for atoms, atomic ions, and diatomic molecules: I. Experimental data. *Reviews of Modern Physics*, *38*(1), 1.

Knudsen, H., Mikkelsen, U., Paludan, K., Kirsebom, K., Moller, S., Uggerhoj, E., Slevin, J., Charlton, M., & Morenzoni, E. (1995). Non-dissociative and dissociative ionization of N2, CO, CO2, and CH4 by impact of 50-6000 keV protons and antiprotons. *Journal of Physics B: Atomic, Molecular and Optical Physics*, *28*(16), 3569.

Kopparapu, R. K., Ramirez, R., Kasting, J. F., Eymet, V., Robinson, T. D., Mahadevan, S., Terrien, R. C., Domagal-Goldman, S., Meadows, V., & Deshpande, R. (2013). HABITABLE ZONES AROUND MAIN-SEQUENCE STARS: NEW ESTIMATES. *The Astrophysical Journal*, *765*(2), 131. https://doi.org/10.1088/0004-637X/765/2/131

Kozakis, T., Mendonça, J. M., & Buchhave, L. A. (2022). Is ozone a reliable proxy for molecular oxygen? - I. The O2–O3 relationship for Earth-like atmospheres. *A&A*, *665*, A156. https://doi.org/10.1051/0004-6361/202244164

Laidler, K. J. (1984). The development of the Arrhenius equation. *Journal of chemical Education*, *61*(6), 494.

Lammer, H. (2012). *Origin and Evolution of Planetary Atmospheres: Implications for Habitability*. Springer London, Limited. https://doi.org/10.1007/978-3-642-32087-3

Lary, D. J. (1997). Catalytic destruction of stratospheric ozone. *Journal of Geophysical Research: Atmospheres*, *102*(D17), 21515–21526. https://doi.org/https://doi.org/10.1029/97JD00912

Leleu, A., Chatel, G., Udry, S., Alibert, Y., Delisle, J.-B., & Mardling, R. (2021). Alleviating the transit timing variation bias in transit surveys - I. RIVERS: Method and detection of a pair of resonant super-Earths around Kepler-1705⋆. *A&A*, *655*, A66. https://doi.org/10.1051/0004-6361/202141471

Määttänen, A., Lefèvre, F., Verdier, L., Montmessin, F., Listowski, C., Guilbon, S., Fedorova, A., & Korablev, O. (2022). Ozone vertical distribution in Mars Years 27–30 from SPICAM/MEX UV occultations. *Icarus*, *387*, 115162. https://doi.org/https://doi.org/10.1016/j.icarus.2022.115162

Madhusudhan, N., Agúndez, M., Moses, J. I., & Hu, Y. (2016). Exoplanetary atmospheres—chemistry, formation conditions, and habitability. *Space science reviews*, *205*, 285–348. https://doi.org/10.1007/s11214-016-0254-3

Matsui, T., & Abe, Y. (1986). Evolution of an impact-induced atmosphere and magma ocean on the accreting Earth. *Nature*, *319*(6051), 303–305. https://doi.org/10.1038/319303a0

Mayor, M., & Queloz, D. (1995). A Jupiter-mass companion to a solar-type star. *nature*, *378*(6555), 355–359.

McKee, C. F., & Ostriker, E. C. (2007). Theory of Star Formation. *Annual Review of Astronomy and Astrophysics*, *45*(Volume 45, 2007), 565–687. https://doi.org/https://doi.org/10.1146/annurev.astro.45.051806.110602

Meador, W. E., & Weaver, W. R. (1980). Two-Stream Approximations to Radiative Transfer in Planetary Atmospheres: A Unified Description of Existing Methods and a New Improvement. *Journal of Atmospheric Sciences*, *37*(3), 630–643. https://doi.org/10.1175/1520-0469(1980)037<0630:TSATRT>2.0.CO;2

Mickey, C. D. (1980). Chemical Kinetics: Reaction Rates. *Journal of Chemical Education*, *57*(9), 659. https://doi.org/10.1021/ed057p659

Millar, T. J., Walsh, C., Van de Sande, M., & Markwick, A. J. (2024). The UMIST Database for Astrochemistry 2022. *A&A*, *682*, A109. https://doi.org/10.1051/0004-6361/202346908

Mironova, I. A., Aplin, K. L., Arnold, F., Bazilevskaya, G. A., Harrison, R. G., Krivolutsky, A. A., Nicoll, K. A., Rozanov, E. V., Turunen, E., & Usoskin, I. G. (2015). Energetic particle influence on the Earth's atmosphere. *Space science reviews*, *194*, 1–96. https://doi.org/10.1007/s11214-015-0185-4

Molina, M. J., & Rowland, F. S. (1974). Stratospheric sink for chlorofluoromethanes: Chlorine atom-catalysed destruction of ozone. *Nature*, *249*(5460), 810–812. https://doi.org/10.1038/249810a0

Müller, H.-R., Frisch, P. C., Florinski, V., & Zank, G. P. (2006). Heliospheric response to different possible interstellar environments. *The Astrophysical Journal*, *647*(2), 1491.

Nakajima, S., Hayashi, Y.-Y., & Abe, Y. (1992). A study on the "runaway greenhouse effect" with a one-dimensional radiative–convective equilibrium model. *Journal of Atmospheric Sciences*, *49*(23), 2256–2266. https://doi.org/10.1175/1520-0469(1992)049<2256:ASOTGE>2.0.CO;2

Nakamura, Y., Leblanc, F., Terada, N., Hiruba, S., Murata, I., Nakagawa, H., Sakai, S., Aoki, S., Piccialli, A., Willame, Y., Neary, L., Vandaele, A. C., Murase, K., & Kataoka, R. (2023). Numerical prediction of changes in atmospheric chemical compositions during a solar energetic particle event on mars [e2022JA031250 2022JA031250]. *Journal of Geophysical Research: Space Physics*, *128*(12), e2022JA031250. https://doi.org/https://doi.org/10.1029/2022JA031250

National Academies of Sciences, Engineering, and Medicine. (2023). *Pathways to Discovery in Astronomy and Astrophysics for the 2020s*. The National Academies Press. https://doi.org/10.17226/26141

Nicolet, M. (1975). On the production of nitric oxide by cosmic rays in the mesosphere and stratosphere. *Planetary and Space Science*, *23*(4), 637–649. https://doi.org/https://doi.org/10.1016/0032-0633(75)90104-X

Nieder, H., Winkler, H., Marsh, D. R., & Sinnhuber, M. (2014). NOx production due to energetic particle precipitation in the MLT region: Results from ion chemistry model studies. *Journal of Geophysical Research: Space Physics*, *119*(3), 2137–2148. https://doi.org/10.1002/2013JA019044

Nordheim, T., Dartnell, L., Desorgher, L., Coates, A., & Jones, G. (2015). Ionization of the venusian atmosphere from solar and galactic cosmic rays. *Icarus*, *245*, 80–86. https://doi.org/https://doi.org/10.1016/j.icarus.2014.09.032

Porter, H. S., Jackman, C. H., & Green, A. E. S. (1976). Efficiencies for production of atomic nitrogen and oxygen by relativistic proton impact in air. *The Journal of Chemical Physics*, *65*(1), 154–167. https://doi.org/10.1063/1.432812

Quanz, S. P., Absil, O., Benz, W., Bonfils, X., Berger, J.-P., Defrère, D., van Dishoeck, E., Ehrenreich, D., Fortney, J., Glauser, A., Grenfell, J. L., Janson, M., Kraus, S., Krause, O., Labadie, L., Lacour, S., Line, M., Linz, H., Loicq, J., … Wyatt, M. (2022a). Atmospheric characterization of terrestrial exoplanets in the mid-infrared: Biosignatures, habitability, and diversity. *Experimental Astronomy*, *54*(2), 1197–1221. https://doi.org/10.1007/s10686-021-09791-z

Quanz, S. P., Ottiger, M., Fontanet, E., Kammerer, J., Menti, F., Dannert, F., Gheorghe, A., Absil, O., Airapetian, V. S., Alei, E., Allart, R., Angerhausen, D., Blumenthal, S., Buchhave, L. A., Cabrera, J., Carrión-González, Ó., Chauvin, G., Danchi, W.

C., Dandumont, C., … the LIFE Collaboration. (2022b). Large Interferometer For Exoplanets (LIFE) - I. Improved exoplanet detection yield estimates for a large mid-infrared space-interferometer mission. *A&A*, *664*, A21. https://doi.org/10.1051/0004-6361/202140366

Ramaroson, R. R. A. (1989, July). *Modélisation locale, à une et trois dimensions des processus photochimiques de l'atmosphère moyenne* [Theses]. Université Pierre et Marie Curie - Paris VI. https://theses.hal.science/tel-00935265

Ramirez, R. M. (2018). A more comprehensive habitable zone for finding life on other planets. *Geosciences*, *8*(8), 280.

Ranjan, S., Schwieterman, E. W., Leung, M., Harman, C. E., & Hu, R. (2023). The Importance of the Upper Atmosphere to CO/O2 Runaway on Habitable Planets Orbiting Low-mass Stars. *The Astrophysical Journal Letters*, *958*(1), L15. https://doi.org/10.3847/2041-8213/ad037c

Reames, D. V. (1999). Particle acceleration at the sun and in the heliosphere. *Space Science Reviews*, *90*(3), 413–491. https://doi.org/10.1023/A:1005105831781

Rieke, M. J., Baum, S. A., Beichman, C. A., Crampton, D., Doyon, R., Eisenstein, D., Greene, T. P., Hodapp, K.-W., Horner, S. D., Johnstone, D., et al. (2003). Ngst nircam scientific program and design concept. *IR space telescopes and instruments*, *4850*, 478–485.

Rimmer, P., & Helling, C. (2013). Ionization in atmospheres of brown dwarfs and extrasolar planets. IV. The effect of cosmic rays. *The Astrophysical Journal*, *774*(2), 108.

Roberge, A., & Seager, S. (2018). The "Spectral Zoo" of Exoplanet Atmospheres. In H. J. Deeg & J. A. Belmonte (Eds.), *Handbook of exoplanets* (pp. 1–20). Springer International Publishing. https://doi.org/10.1007/978-3-319-30648-3_98-1

Rusch, D., Gérard, J.-C., Solomon, S., Crutzen, P., & Reid, G. (1981). The effect of particle precipitation events on the neutral and ion chemistry of the middle atmosphere—I. Odd nitrogen. *Planetary and Space Science*, *29*(7), 767–774. https://doi.org/https://doi.org/10.1016/0032-0633(81)90048-9

Rushby, A. J., Shields, A. L., & Joshi, M. (2019). The Effect of Land Fraction and Host Star Spectral Energy Distribution on the Planetary Albedo of Terrestrial Worlds. *The Astrophysical Journal*, *887*(1), 29. https://doi.org/10.3847/1538-4357/ab4da6

Rustamkulov, Z., Sing, D. K., Mukherjee, S., May, E. M., Kirk, J., Schlawin, E., Line, M. R., Piaulet, C., Carter, A. L., Batalha, N. E., Goyal, J. M., López-Morales, M., Lothringer, J. D., MacDonald, R. J., Moran, S. E., Stevenson, K. B., Wakeford, H. R., Espinoza, N., Bean, J. L., … Zieba, S. (2023). Early Release Science of the exoplanet WASP-39b with JWST NIRSpec PRISM. *Nature*, *614*(7949), 659–663. https://doi.org/10.1038/s41586-022-05677-y

Sagan, C. (1997). *Pale blue dot: A vision of the human future in space* [Originally published 1994]. Ballantine Books.

Sanchez-Lavega, A. (2010). *An Introduction to Planetary Atmospheres*. Taylor & Francis.

Scherer, K., Herbst, K., Engelbrecht, N., Ferreira, S., Kleimann, J., & Light, J. (2025). Modeling the astrosphere of LHS 1140-On the differences of 3D magnetohydrodynamic single- and multi-fluid simulations and the consequences for exoplanetary habitability. *Astronomy & Astrophysics*, *694*, A106.

Scheucher, M., Wunderlich, F., Grenfell, J. L., Godolt, M., Schreier, F., Kappel, D., Haus, R., Herbst, K., & Rauer, H. (2020). Consistently Simulating a Wide Range of Atmospheric Scenarios for K2-18b with a Flexible Radiative Transfer Module. *The Astrophysical Journal*, *898*(1), 44. https://doi.org/10.3847/1538-4357/ab9084

Schleif, C. (2024). *A Model-Based Study on the Influence of Solar Activity on the Atmospheric Chemistry of Venus and Mars* [Master's thesis, Karlsruher Institut für Technologie (KIT)]. Karlsruher Institut für Technologie (KIT). https://doi.org/10.5445/IR/1000178976

Schreier, F., Gimeno García, S., Hedelt, P., Hess, M., Mendrok, J., Vasquez, M., & Xu, J. (2014). GARLIC — A general purpose atmospheric radiative transfer line-by-line infrared-microwave code: Implementation and evaluation. *Journal of Quantitative Spectroscopy and Radiative Transfer*, *137*, 29–50. https://doi.org/https://doi.org/10.1016/j.jqsrt.2013.11.018

Seager, S., Welbanks, L., Ellerbroek, L., Bains, W., & Petkowski, J. J. (2025). Prospects for detecting signs of life on exoplanets in the jwst era. *Proceedings of the National Academy of Sciences*, *122*(39), e2416188122. https://doi.org/10.1073/pnas.2416188122

Selwyn, G., Podolske, J., & Johnston, H. S. (1977). Nitrous oxide ultraviolet absorption spectrum at stratospheric temperatures. *Geophysical Research Letters*, *4*(10), 427–430.

Semeniuk, K., McConnell, J. C., Jin, J. J., Jarosz, J. R., Boone, C. D., & Bernath, P. F. (2008). N2O production by high energy auroral electron precipitation. *Journal of Geophysical Research: Atmospheres*, *113*(D16). https://doi.org/https://doi.org/10.1029/2007JD009690

Sheese, P. E., Walker, K. A., Boone, C. D., Bernath, P. F., & Funke, B. (2016). Nitrous oxide in the atmosphere: First measurements of a lower thermospheric source. *Geophysical Research Letters*, *43*(6), 2866–2872. https://doi.org/https://doi.org/10.1002/2015GL067353

Sinnhuber, M., Nieder, H., & Wieters, N. (2012). Energetic Particle Precipitation and the Chemistry of the Mesosphere/Lower Thermosphere. *Surveys in Geophysics*, *33*(6), 1281–1334. https://doi.org/10.1007/s10712-012-9201-3

Solomon, S., Rusch, D., Gérard, J., Reid, G., & Crutzen, P. (1981). The effect of particle precipitation events on the neutral and ion chemistry of the middle atmosphere: II. Odd hydrogen. *Planetary and Space Science*, *29*(8), 885–893. https://doi.org/https://doi.org/10.1016/0032-0633(81)90078-7

Stiller, G. P., Kiefer, M., Eckert, E., von Clarmann, T., Kellmann, S., García-Comas, M., Funke, B., Leblanc, T., Fetzer, E., Froidevaux, L., Gomez, M., Hall, E., Hurst, D., Jordan, A., Kämpfer, N., Lambert, A., McDermid, I. S., McGee, T., Miloshevich, L., … Whiteman, D. N. (2012). Validation of MIPAS IMK/IAA temperature, water vapor, and ozone profiles with MOHAVE-2009 campaign measurements. *Atmospheric Measurement Techniques*, *5*(2), 289–320. https://doi.org/10.5194/amt-5-289-2012

Straub, H. C., Renault, P., Lindsay, B. G., Smith, K. A., & Stebbings, R. F. (1996). Absolute partial cross sections for electron-impact ionization of $H_2$, $N_2$, and $O_2$ from threshold to 1000 eV. *Phys. Rev. A*, *54*, 2146–2153. https://doi.org/10.1103/PhysRevA.54.2146

Tsurutani, B. T., Judge, D. L., Guarnieri, F. L., Gangopadhyay, P., Jones, A. R., Nuttall, J., Zambon, G. A., Didkovsky, L., Mannucci, A. J., Iijima, B., Meier, R. R., Immel, T. J., Woods, T. N., Prasad, S., Floyd, L., Huba, J., Solomon, S. C., Straus, P., & Viereck, R. (2005). The October 28, 2003 extreme EUV solar flare and resultant extreme

ionospheric effects: Comparison to other Halloween events and the Bastille Day event. *Geophysical Research Letters*, *32*(3). https://doi.org/https://doi.org/10.1029/2004GL021475

Vida, K., Kővári, Z., Pál, A., Oláh, K., & Kriskovics, L. (2017). Frequent Flaring in the TRAPPIST-1 System—Unsuited for Life? *The Astrophysical Journal*, *841*(2), 124. https://doi.org/10.3847/1538-4357/aa6f05

Vidotto, A. A. (2021). The evolution of the solar wind. *Living Reviews in Solar Physics*, *18*(1), 3. https://doi.org/10.1007/s41116-021-00029-w

Volkov, A. N. (2017). Exobase properties of hydrodynamic and kinetic models of thermal escape from planetary atmospheres and notion of slow hydrodynamic escape. *Monthly Notices of the Royal Astronomical Society*, *472*(2), 1825–1841. https://doi.org/10.1093/mnras/stx1917

Wallner, M., Jarraya, M., Olsson, E., Ideböhn, V., Squibb, R. J., Yaghlane, S. B., Nyman, G., Eland, J. H., Feifel, R., & Hochlaf, M. (2022). Abiotic molecular oxygen production—Ionic pathway from sulfur dioxide. *Science Advances*, *8*(33), eabq5411. https://doi.org/10.1126/sciadv.abq5411

Wennberg, P. O., Anderson, J. G., & Weisenstein, D. K. (1994). Kinetics of reactions of ground state nitrogen atoms ($^4S_{3/2}$) with NO and $NO_2$. *Journal of Geophysical Research: Atmospheres*, *99*(D9), 18839–18846. https://doi.org/10.1029/94JD01823

Wilson, D. J., Froning, C. S., Duvvuri, G. M., France, K., Youngblood, A., Schneider, P. C., Berta-Thompson, Z., Brown, A., Buccino, A. P., Hawley, S., Irwin, J., Kaltenegger, L., Kowalski, A., Linsky, J., Parke Loyd, R. O., Miguel, Y., Pineda, J. S., Redfield, S., Roberge, A., … Vieytes, M. (2021). The mega-muscles spectral energy distribution of trappist-1. *The Astrophysical Journal*, *911*(1), 18. https://doi.org/10.3847/1538-4357/abe771

Windmark, F., Birnstiel, T., Güttler, C., Blum, J., Dullemond, C. P., & Henning, Th. (2012). Planetesimal formation by sweep-up: how the bouncing barrier can be beneficial to growth. *A&A*, *540*, A73. https://doi.org/10.1051/0004-6361/201118475

Winkler, H., Kazeminejad, S., Sinnhuber, M., Kallenrode, M.-B., & Notholt, J. (2009). Conversion of mesospheric HCl into active chlorine during the solar proton event in July

2000 in the northern polar region. *Journal of Geophysical Research: Atmospheres*, *114*(D1). https://doi.org/https://doi.org/10.1029/2008JD011587

Winkler, H. (2008). *The response of middle atmospheric ozone to solar proton events in a changing geomagnetic field.* [Doctoral dissertation].

Wissing, J. M., Kallenrode, M.-B., Wieters, N., Winkler, H., & Sinnhuber, M. (2010). Atmospheric Ionization Module Osnabrück (AIMOS): 2. Total particle inventory in the October–November 2003 event and ozone. *Journal of Geophysical Research: Space Physics*, *115*(A2). https://doi.org/https://doi.org/10.1029/2009JA014419

Wunderlich, F., Scheucher, M., Godolt, M., Grenfell, J. L., Schreier, F., Schneider, P. C., Wilson, D. J., Sánchez-López, A., López-Puertas, M., & Rauer, H. (2020). Distinguishing between Wet and Dry Atmospheres of TRAPPIST-1 e and f. *The Astrophysical Journal*, *901*(2), 126. https://doi.org/10.3847/1538-4357/aba59c

Wunderlich, F., Scheucher, M., Grenfell, J. L., Schreier, F., Sousa-Silva, C., Godolt, M., & Rauer, H. (2021). Detectability of biosignatures on LHS 1140 b. *A&A*, *647*, A48. https://doi.org/10.1051/0004-6361/202039663

Yoon, J.-S., Song, M.-Y., Han, J.-M., Hwang, S. H., Chang, W.-S., Lee, B., & Itikawa, Y. (2008). Cross Sections for Electron Collisions with Hydrogen Molecules. *Journal of Physical and Chemical Reference Data*, *37*(2), 913–931. https://doi.org/10.1063/1.2838023

Youdin, A. N., & Goodman, J. (2005). Streaming Instabilities in Protoplanetary Disks. *The Astrophysical Journal*, *620*(1), 459. https://doi.org/10.1086/426895

Zipf, E., & Prasad, S. (1980). Production of nitrous oxide in the auroral D and E regions. *Nature*, *287*(5782), 525–526. https://doi.org/10.1038/287525a0

# Appendix

# A. List of Figures

# B. List of Tables

# C. List of Code

# Acknowledgments

Zuallerst bedanke ich mich für die Möglichkeit, dass ich in einem äußerst spannenden Projekt (INCREASE) promovieren durfte, welches vom Schwerpunktprogramm 1992 "Exploring the Diversity of Extrasolar Planets (HE8392/1-1, GR 2004/4-1, SI1088/9-1, SM 486/2-1)" der Deutschen Forschungsgemeinschaft (DFG) gefördert wurde. Die Simulationen für diese Doktorarbeit wurden auf dem Supercomputer BwUniCluster2.0/3.0 durchgeführt. Es ist eingebettet in die HPC-Cluster Infrastruktur (bwHPC) und wird gefördert durch das Ministerium für Wissenschaft, Forschung und Kunst des Landes Baden-Württemberg, der DFG sowie von 10 Universitäten in Baden-Württemberg.

Ein besonderer Dank gilt Dr. Miriam Sinnhuber für ihre großartige Betreuung und dass ich als Doktorrand in ihrer Gruppe arbeiten durfte. Vielen Dank für die guten Gespräche, Ratschläge und Diskussionen, die mich stets weiter gebracht haben. Des Weiteren gilt mein Dank Prof. Dr. Peter Braesicke und Prof. Dr. Thomas Leisner, die die Rolle der Referrenten übernommen haben.

Ich bedanke mich besonders bei unseren Partnern am DLR Berlin, Dr. John Lee Grenfell, Dr. Nicolas Iro, Dr. Ben Taysum und Dr. Fabian Wunderlich, die die Simulationen mit dem Klimamodell 1D-TERRA zur Verfügung gestellt haben. Ein weiterer Dank geht an Dr. Konstantin Herbst (Universität Kiel, jetzt Universität Oslo), der innerhalb des INCREASE Projekts die Ionisationsraten bereitgestellt hat.

At this point, special thanks go to Dr. Ben Taysum, who ran the GARLIC model to provide the transmission spectra. Even after the personnel change at DLR, he agreed to take on this role in addition to his regular work.

Vielen Dank an Prof. Thomas Bohlen für die Bereitschaft zur Übernahme der Mentorenrolle während der Promotion. Auch wenn es wohl nur sehr selten zu Problemen kommt, ist es gut für den Notfall einen Ansprechpartner zu haben.

Für die Unterstützung in der MSK Gruppe und der MOD Gruppe. Es war eine wunderbare Zeit und ein solches Arbeitsumfeld mit diesen netten Kolleg:innen kann man nur jedem wünschen. Insbesondere die gemeinsamen Mittagessen und die Pläuschchen auch über

nichtwissenschaftliche Themen waren immer ein Highlight des Tages. Außerdem danke ich Dr. Lena Feld, Valentin Hanft und Dr. Florian Haenel für die hilfreichen Kommentare zu dieser Doktorarbeit.

Ich danke allen IMKASF Mitarbeiter:innen, insbesondere Esther-Salome Prietzel für die Unterstützung bei den administrativen Angelegenheiten und Claudia Roesner für den Support bei bei technischen Problemen am Computer.

Ich danke meiner Familie, besonders meinen Eltern Anja und Hans, sowie meinem Bruder Johannes. Vielen Dank, dass ihr mich bei allem immer unterstützt und den Rücken freigehalten habt! An die KG-Salgen, es ist schön, wenn man Freunde hat, die einen immer unterstützen und mit denen man seine Zeit verbringen darf.